Automated Ultrasound Studies Of Magnetoelastic Effects In Rare Earth Metals and Alloys

Chee Ming Lim

Submitted for the degree of Doctor of Philosophy
at the University of Warwick.

Department of Physics,
University of Warwick

April 1998

Table Of Contents

List Of Figures

Chapter 1

Chapter 3

Chapter 4

Chapter 5

Figure 5.8. Signal processed C_{33} (zero field) data and a 3 point nearest neighbour averaging applied.

Figure 5.9. Longitudinal wave attenuation as a function of temperature for Tm. Wave propagating down the c-axis at zero applied field.

Figure 5.10. C_{44} as a function of temperature at zero applied field.

Figure 5.11. Signal processed zero field C_{44} data as a function of temperature with 3 points averaging applied.

Figure 5.12. Zero field shear wave attenuation (α_{44}) versus temperature. Wave propagating direction down the c-axis.

Figure 5.13. C_{44} as a function of temperature for Tm with c-axis applied field at 0.5, 2.0 and 3.0 T.

Figure 5.14. Shear wave attenuation as a function of temperature for Tm with c-axis applied field at 3 T. Shear wave propagated down c-axis.

Figure 5.15. C_{66} as a function of temperature for Tm.

Figure 5.16. C_{11} as a function of temperature for Tm.

Figure 5.17. Waveforms of EMAT generated in-plane radially polarised shear wave propagating down the c-axis of Tm with sample temperature at 60, 70 and 96 K. C-axis applied magnetic field at 2 T.

Figure 5.18. EMAT measured C_{44} as a function of temperature for Tm with c-axis applied field at 0.6 and 1.5 T.

Figure 5.19. Shear wave EMAT signal amplitude as a function of temperature. Wave propogated down c-axis of Tm with c-axis applied field at 1 T.

Figure 5.20. H_o - T plot of EMAT signal amplitude for Tm. H_o and shear wave propagation along the c-axis of the single crystal Tm.

Chapter 6

Figure 6.1. C_{44} versus temperature for $Er_{91.6\%}Tm_{8.4\%}$ at zero field.

Figure 6.2. Shear wave attenuation versus temperature at zero field for $Er_{91.6\%}Tm_{8.4\%}$.

Figure 6.3. C_{44} versus temperature for $Er_{91.6\%}Tm_{8.4\%}$ with c-axis applied field at 0.5, 0.75, 1.0 T.

Figure 6.4. C_{44} versus temperature for $Er_{91.6\%}Tm_{8.4\%}$ with c-axis applied field at 0, 3 and 4 T.

Figure 6.5. Shear wave attenuation as a function of temperature for $Er_{91.6\%}Tm_{8.4\%}$ with c-axis applied field at 3 T.

Figure 6.6a. C_{33} as a function of temperature for $Er_{91.6\%}Tm_{8.4\%}$ at zero field.

Figure 6.6b-d. Expanded graph of figure 6.6a.

Figure 6.7. C_{33} as a function of temperature for $Er_{91.6\%}Tm_{8.4\%}$ with c-axis applied field at 0.5 T.

Figure 6.8. C_{33} as a function of temperature for $Er_{93.3\%}Tm_{6.7\%}$ with c-axis applied field at 0, 1, 2, 3 and 4 T.

Figure 6.9. Longitudinal wave attenuation as a function of temperature for $Er_{93.3\%}Tm_{6.7\%}$ at zero field. Wave propagation down the c-axis.

Figure 6.10. C_{11} as a function of temperature for $Er_{91.6\%}Tm_{8.4\%}$ with a-axis applied magnetic field at 0, 0.5 and 1 T.

Figure 6.11. Longitudinal wave attenuation as function of temperature at zero field. Wave propagation down the a-axis.

Figure 6.12. C_{66} as a function of temperature for $Er_{91.6\%}Tm_{8.4\%}$ with a-axis applied field at 0, 0.5, 1 and 2 T.

Figure 6.13. B-axis polarised shear wave attenuation as a function of temperature for $Er_{91.6\%}Tm_{8.4\%}$ at zero field. Wave propagated down the a-axis.

Figure 6.14. EMAT measured C_{44} as a function of temperature for $Er_{91.6\%}Tm_{8.4\%}$ with c-axis applied field at 0.5, 0.75 and 1 T.

Figure 6.15. EMAT measured C_{33} as a function of temperature for $Er_{91.6\%}Tm_{8.4\%}$ with c-axis applied field at 0.5, 0.75 and 1 T.

Figure 6.16. EMAT signal amplitude versus temperature for $Er_{91.6\%}Tm_{8.4\%}$ with c-axis applied field at 0.5, 0.75 and 1 T.

Figure 6.17. Waveforms of EMAT generated in-plane radially polarised shear waves propagating down the c-axis of $Er_{91.6\%}Tm_{8.4\%}$ at 77 K.

Figure 6.18. Longitudinal EMAT signal amplitude as a function of temperature for $Er_{91.6\%}Tm_{8.4\%}$ with c-axis applied field at 0.5, 0.75 and 1 T.

Figure 6.19. H_o - T plot of EMAT signal amplitude for $Er_{91.6\%}Tm_{8.4\%}$. H_o and shear wave propagation along the c-axis.

Declaration

The work contained in this thesis is my own except where specifically stated otherwise, and was based in the Department of Physics, University of Warwick from January 1995 to April 1998. No part of this work has been previously submitted to this or any other academic institution for admission to a higher degree. Some of the work has appeared in the form of publications which are listed in the bibliography.

Abstract

Ultrasound studies of single crystals of Er, Tm and alloys of Er-Tm were carried out as a function of temperature (4.2 - 300 K) and applied magnetic field (0 - 5 T). The elastic constants of these materials were measured and anomalies in the elastic constants were observed. The ultrasound data were compared with reported results from other material characterisation techniques and the magnetic phases and transition temperatures of the materials were then identified. The effects of the application of magnetic field on the magnetic ordering of the materials were studied using the ultrasound method. In Er-Tm there was evidence of applied field (a-axis field and c-axis field) induced ordering in the cycloid phase and c-axis applied magnetic field of > 3 T resulted in the ferrimagnetic to ferromagnetic transition in Tm.

A commercial ultrasound measurement system was modified and adapted for use in this work. The modified system enables the ultrasonic velocity and attenuation to be measured as a function of: (a) temperature, (b) applied magnetic field and (c) frequency. The present system was enhanced to work with less efficient ultrasonic transducers such as quartz and electromagnetic acoustic (EMAT) transducers.

This work looked at the design and feasibility of using EMATs to generate ultrasound in single crystals of the rare earth metals and alloys. EMATs generating (a) in-plane radially polarised shear waves and (b) longitudinal waves were made and shown to work on these materials. The use of EMATs meant that ultrasound measurements could be conducted in the non-contact regime, i.e. no acoustic couplant is required between the sample and transducer. EMATs are particularly useful in this work where the sample and transducer are subjected to repeated temperature cycles over a wide temperature range (4.2 to 300 K) and acoustic couplant can fracture.

The EMAT acoustic coupling efficiency in these samples were studied as a function of temperature and applied magnetic field. Large increases in the EMAT acoustic coupling efficiency (combination of generation and detection efficiencies) often occur close to the magnetic phase transition temperatures of the samples.

Chapter 1

Preview

A wave is characterised by its amplitude, direction of propagation, polarisation, frequency and wavelength. The characteristics of an ultrasonic wave can change as it interacts with the medium through which it propagates. The ultrasonic wave interactions can be observed via the changes in the wave polarisation, velocity and attenuation. Several of the recognised wave interaction mechanisms are listed and discussed in Truell *et al.* (1969). Measurement and monitoring of the ultrasonic wave velocity (group velocity) and attenuation is the basis of ultrasound measurement.

The aims of this work are:

(a) to adapt a commercial ultrasound measurement system (Matec DSP-8000) for use in the ultrasound study of single crystal rare earth metals and alloys.

(b) to perform ultrasound measurements on single crystals of erbium (Er) thulium (Tm) and the binary alloy Er-Tm as a function of temperature and applied magnetic field.

(c) to study the feasibility of using electromagnetic acoustic transducers (EMAT) in the ultrasound study of single crystal rare earth metals and alloys.

In this work the elastic properties of single crystal rare earth metal; Er, Tm and their binary alloy (Er-Tm) are studied using ultrasound measurement techniques. The ultrasonic wave velocities are measured as a function of temperature and applied magnetic field. The relationship between the ultrasonic velocities and the elastic constants (moduli) for these samples (hexagonal close-packed structure) are described in chapter 2. While the theoretical aspects of ultrasonic wave propagation in hexagonal close-packed crystal are being described, the experimental considerations are also discussed. This is then followed by a brief description of the different ultrasound measurement techniques used in the study of single crystal rare earth metals.

Section 2.3 serves as a generic section introducing the general properties, with emphasis on the magnetic structures, of Er and Tm. The magnetic structures of these metals have been extensively studied, namely by x-ray and neutron diffraction techniques [Cable *et al.,* 1965], [Habenschuss *et al.*, 1974], [Cowley and Jensen, 1992], [Åström *et al.*, 1991], [Koehler *et al.* , 1962] [McEwen *et al.* , 1995]. Several magnetic phases have been identified in these metals.

Although the magnetic properties of these samples have been studied using other material characterisation techniques, the results from the ultrasound measurement shown in this thesis are believed to be the first reported for the single crystal of Tm and Er-Tm. Furthermore, this work is believed to be the first reported ultrasound studies of single crystal Er, Tm and Er-Tm using a miniature EMAT. The use of an EMAT enables the ultrasound measurements to be performed in the non-contact regime, therefore avoiding acoustic couplant problems. In the ultrasound studies of the rare earth metals

the sample and transducers are often subjected to the extreme of temperatures (4.2 K to 300 K). If a contact ultrasound measurement method is used, the choice of acoustic couplant becomes critical. The wide temperature range and repeated temperature cycling causes severe thermal stress on the acoustic couplant which often results in the breaking of the acoustic couplant, i.e. the sample becomes acoustically detached from the transducer. This can be particular problem for some of the rare earth materials which can expand along the c-axis while contracting along the basal plane. The EMAT acoustic coupling efficiency, however, is dependent on the magnetic and electrical properties of the sample. One would expect a great variation in the EMAT acoustic coupling efficiency from sample to sample. Furthermore, these properties which the EMAT acoustic generation efficiency is dependent on are not single valued but are dependent on the temperature, pressure and applied magnetic field. For magnetically anisotropic materials, the direction of the applied magnetic field also affects the EMAT acoustic generation efficiency.

Chapter 3 describes the ultrasound measurement system. The ultrasound measurement system used in this work is a modified version of a Matec DSP-8000. The aim is to produce an automated ultrasound measurement system which can perform velocity and attenuation measurements as a function of temperature, frequency and applied magnetic field. In chapter 3 the process of integrating the DSP-8000 with an Oxford Instruments cryogenic system and super-conducting magnet is described. At the initial stage of this work a large proportion of time was spent in modifying the original DSP-8000 software. Modifications to the software were necessary to bring the system to the desired level of automation. The modifications made to the different sections of the

software are described in section 3.5. Chapter 3 also describes the hardware modifications to enable the use of EMAT and quartz transducers. Most commercial ultrasound measurement systems are designed to drive lead zirconate titanate (PZT) or similar transducers. The acoustic generation efficiency of PZT transducers are orders of magnitude better than those of quartz transducers and EMAT and therefore additional amplifiers and filter circuit are required to improve the signal to noise ratio. The EMAT design considerations are discussed in section 3.6. Chapter 3 ends with the description of sample preparation.

The experimental results for the Er, Tm and Er-Tm samples are shown and discussed in chapters 4, 5 and 6 respectively. The ultrasound measurements using spiral coil EMAT, generating in-plane radially polarised shear wave, was tested on the single crystal Er sample. The aims of this preliminary test is to:

(a) monitor the performance of the in-house design and manufactured EMAT coils.

(b) evaluate the performance of the automated ultrasound measurement system.

(c) study EMAT acoustic coupling efficiency as a function of temperature and applied magnetic field on single crystal of Er.

The EMAT ultrasound measurement results were then compared with the ultrasound measurement results reported by Palmer *et al.* (1974) and Eccleston and Palmer (1992). The shortfalls of the automated ultrasound measurement system were noted. The results from the preliminary EMAT ultrasound measurement show spectacular changes in EMAT acoustic coupling efficiency for the different magnetic phases of Er. An increase in EMAT acoustic coupling efficiency of several orders of

magnitude was observed close to the magnetic phase transition temperatures. Hence demonstrating the possibility of using the EMAT acoustic coupling efficiency to detect magnetic phase transitions in the rare earth metals.

In chapter 5 the results from the ultrasound measurements of the single crystal Tm sample are presented. The elastic moduli (C_{11}, C_{33}, C_{44} and C_{66}) as a function of temperature and applied magnetic field were measured. Several anomalies in the elastic moduli measurements were observed. EMATs were also used in the ultrasound measurements of the Tm sample. The EMAT signal amplitude was used to construct a tentative magnetic phase diagram for the Tm sample.

Two binary alloys of Er and Tm were studied. Both samples were in the form of single crystals. The compositions, as atomic weight percentage, for the alloys are; $Er_{93.3\%}Tm_{6.7\%}$ and $Er_{91.6\%}Tm_{8.4\%}$. The elastic moduli of the samples were measured as a function of temperature and applied magnetic field. The results from these ultrasound measurements are presented in chapter 6. Longitudinal EMAT was tested on the $Er_{91.6\%}Tm_{8.4\%}$ sample. The results show distinct differences in the EMAT acoustic coupling efficiency between shear wave and longitudinal wave generation. A tentative magnetic phase diagram of $Er_{91.6\%}Tm_{8.4\%}$ has been constructed using the shear wave EMAT signal amplitude.

The overall performance of the automatic ultrasound measurement system proved to be satisfactory but there were some shortfalls. In chapter 7, the performance of the automated ultrasound measurement system is evaluated. Methods of improving the

system are discussed and suggested as further work. The use of EMAT in ultrasound studies of rare earth metals is discussed in chapter 7.

References

Atoji M. 1974, Solid State Commun., **14**, pp1047.

Åström H.U., Nogues J., Nicolaides G.K., Rao K.V. and Benediktsson G. 1991 J. Phys.: Condens. Matter **3**, pp7395-7402.

Cowley R.A. and Jensen J. 1992, J. Phys. Condens. Matter **4** pp9673-9696.

Eccleston R.S. and S.B. Palmer 1992, J. Magnetism and Magnetic Materials, **104-107**, pp1529-1530.

Koehler W.C., Cable J.W., Wollan E.O. and Wilkinson, M.K. 1962, Phys. Rev. B **126**, pp1672.

McEwen K.A., Steigenberger U. Weiss L. Zeiske T. and Jensen J. 1995, J. Magnetism and Magnetic Materials, pp767-768.

Palmer S.B., E.W. Lee and M.N. Islam 1974, Proc. Roy. Soc. Ser. **A338**, pp341.

Truell R., Elbaum C. and Chick B.B. 1969, *Ultrasonic Methods in Solid State Physics*, Academic Press, chpt 1.

Chapter 2

Ultrasonic Techniques And The Magnetic Properties Of Er And Tm.

2.0 Introduction

The aim of this chapter is firstly in section 2.1 to provide the necessary background to the ultrasound measurements associated with this work. This is followed by an introduction to ultrasound measurement techniques, with emphasis on the pulse-echo method. In the ultrasonic theory section practical considerations are also discussed and in section 2.3, the magnetic properties of Er and Tm are introduced.

2.1 Ultrasound Characterisation Of Solids

The fundamental aim of ultrasound measurements is to generate, propagate and detect ultrasonic waves. Changes in the wave characteristics, i.e. velocity and attenuation, then imply physical changes in the sample.

In general, three distinct waves can be propagated along any one direction in a crystal, their displacements being mutually orthogonal to each other. For a wave

propagating along a non-symmetry direction in an anisotropic medium, the wave energy does not coincide with the wave front normal, see figure 2.1, and as a consequence the ultrasound beam is steered. In ultrasound measurements it is the wave front velocity (group velocity) that is measured [Musgrave, 1970]. In general, the group velocity and phase velocity are not equal. In this work the interest is in propagating ultrasonic waves along the principal axes of the hexagonal close-packed (hcp) structure. The basal plane is isotropic and all the wave surfaces are circular. This means that the velocity and wave surfaces coincide. Any section containing the c-axis (orthogonal to the basal plane) has non-circular slowness surfaces (sm^{-1}) as illustrated in Figure 2.2 for Er. The longitudinal slowness surface is indicated by L and the shear slowness surface, S1 (polarisation along the b-axis), is shown dotted whereas the other shear slowness surface, S2 (basal plane polarised), is shown in solid line. If the waves propagate along the c-axis direction the two shear slowness surfaces coincide, hence there is no ambiguity in the shear velocity measurement. However, if the wave is propagated off the c-axis, say at 45° to the c-axis, the S1 and S2 surfaces are separated implying that one would obtain two different shear velocities, as expected.

Simple propagation theory assumes plane waves. However it is difficult if not impossible to achieve the plane wave condition. The form of the propagation is determined by the transducer size and resonant frequency. Considering a continuous wave transducer modelled as a piston radiator the near field extent is given by; $N = D^2/4\lambda$ and the ultrasound beam divergent half angle is given by $\theta = \sin^{-1}(1.22\lambda/D)$. D is the diameter of the transducer and λ the ultrasound wavelength. Typically the quartz

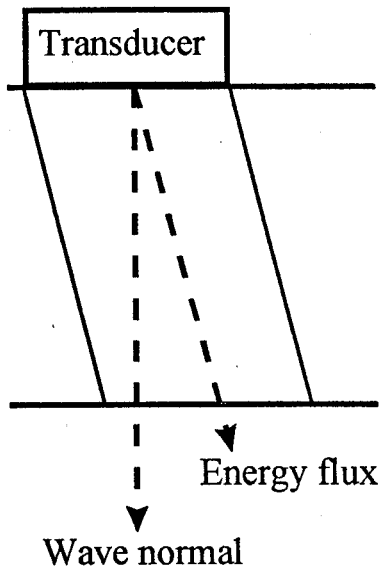

Figure 2.1. Wave propagation along the non-symmetry direction in an anisotropic media. Wave propagation direction and the energy flux direction do not coincide.

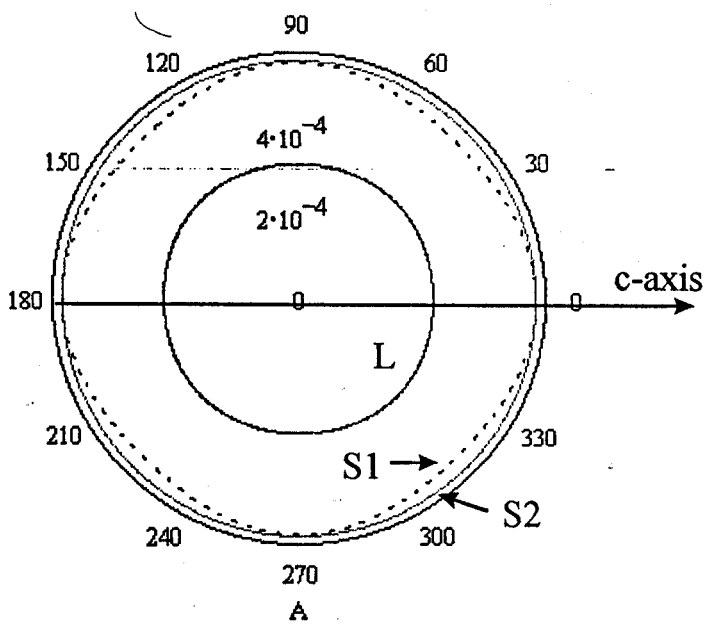

Figure 2.2. Sloweness surfaces of longitudinal wave, L, and shear waves, S1 and S2, for Er. C_{11} = 83.7 GPa, C_{12} = 29.3 GPa, C_{13} = 22.3 GPa, C_{33} = 84.5 and C_{66} = 27.1 GPa. Elastic modulus data at 300 K from Palmer *et. al.* (1974).

transducers used are 2.0 mm in diameter and resonant at 10 MHz, giving for a typical longitudinal velocity of 3200 ms^{-1} , $\lambda = 0.32$ mm and $\theta = 11^{\circ}$ and $N = 9.8$ mm. And for a typical shear velocity of 1800 ms^{-1}, $\lambda = 0.18$ mm and $\theta = 6^{\circ}$ and $N = 30.8$ mm.

In the near field the on-axis maxima and minima become less pronounced for a transducer driven by a tone burst; tone-bursts of less than 5 cycles are used for the present work so it is expected that (with sample thickness of around 4mm) near field effects should not cause any problems.

We will now develop the relationship between the elastic moduli and ultrasonic velocity for a hexagonal crystal. It must be emphasised that plane waves are considered and the medium is assumed to be non-dispersive. The displacement, s, of a particle, in the medium in which a stress wave propagates, is related to the elastic modulus, C, as [Truell *et al.*, 1969];

$$C_{ijkl}s_{ol}n_k n_j = \rho v^2 s_{oi} \qquad (2.1)$$

where ρ is the density of the medium and the displacement; $s_x = s_{ox}e^{i(\omega t - \mathbf{k}.\mathbf{r})}$ with s_{ox} being the amplitude of the displacement at time $t = 0$. The subsript x can be replaced by i,j,k or l. ω the wave angular frequency, wavevector $\mathbf{k} = (2\pi/\lambda)\mathbf{n}$, $\mathbf{n}$ the unit vector normal to the wave front and the subscripts i, j, k and l can take the values 1, 2 or 3. For the hcp system the elastic moduli tensor C_{ijkl} is reduced to the 5 elements shown in

equation 2.2. in the matrix notation, i.e. $C_{1111} \equiv C_{11}$, $C_{1122} \equiv C_{12}$, $C_{1133} \equiv C_{13}$, $C_{3333} \equiv C_{33}$, $C_{2323} \equiv C_{3232} \equiv C_{44}$ and $C_{1212} \equiv C_{2121} \equiv C_{66}$.

$$\begin{array}{cccccc} C_{11} & C_{12} & C_{13} & - & - & - \\ C_{12} & C_{11} & C_{13} & - & - & - \\ C_{12} & C_{13} & C_{33} & - & - & - \\ - & - & - & C_{44} & - & - \\ - & - & - & - & C_{44} & - \\ - & - & - & - & - & C_{66} = (C_{11} - C_{12})/2 \end{array} \qquad (2.2)$$

Using equation 2.1 and equation 2.2 a set of equations are obtained;

$$\begin{aligned} &\left[C_{11}n_1^2 + \frac{1}{2}(C_{11} - C_{12})n_2^2 + C_{44}n_3^2 - \rho v^2\right]s_{o1} + \left[\frac{1}{2}(C_{11} + C_{12})n_1n_2\right]s_{o2} + \\ &\qquad \left[(C_{13} + C_{44})n_1n_3\right]s_{o3} = 0 \\ &\left[\frac{1}{2}(C_{11} + C_{12})n_1n_2\right]s_{o1} + \left[\frac{1}{2}(C_{11} - C_{12})n_1^2 + C_{11}n_2^2 + C_{44}n_3^2 - \rho v^2\right]s_{o2} \\ &\qquad + \left[(C_{13} + C_{44})n_2n_3\right]s_{o3} = 0 \\ &\left[(C_{13} + C_{44})n_1n_3\right]s_{o1} + \left[(C_{13} + C_{44})n_2n_3\right]s_{o2} + \\ &\qquad \left[C_{44}\left(n_1^2 + n_2^2\right) + C_{33}n_3^2 - \rho v^2\right]s_{o3} = 0 \end{aligned} \qquad (2.3)$$

If the wave is propagated down the c-axis of a hcp structure, then $n_1 = n_2 = 0$, $n_3 = 1$ and the above equation reduces to;

$$(C_{44} - \rho v^2)s_{o1} = 0$$
$$(C_{44} - \rho v^2)s_{o2} = 0 \qquad (2.4)$$
$$(C_{33} - \rho v^2)s_{o3} = 0$$

The solutions to equation 2.4 implies that C_{44} can be obtained by measuring the shear wave velocity propagated down the c-axis with polarisation parallel either to the a-axis or b-axis. The C_{33} modulus can be obtained from the velocity measurement of the longitudinal wave propagated down the c-axis. Directing waves down the a-axis, $n_1 = 1$, $n_2 = n_3 = 0$ reduces equation 2.3 to,

$$(C_{11} - \rho v^2)s_{o1} = 0$$
$$[(C_{11} - C_{12})/2 - \rho v^2]s_{o2} = 0 \qquad (2.5)$$
$$(C_{44} - \rho v^2)s_{o3} = 0$$

The solution to equation 2.5 shows the longitudinal velocity measurement would provide the value for C_{11} and shear wave velocities measurements with polarisation along the c-axis would give C_{44} and if the shear wave polarisation is along the b-axis $C_{66} = \frac{1}{2}(C_{11} - C_{12})$ is obtained. Velocity measurements of the transverse and longitudinal waves along the c-axis and a-axis therefore give only C_{33}, C_{44}, C_{11}, C_{12} and C_{66}. To determine C_{13}, velocity measurement with wave propagation in another direction is required. A typical direction in which the wave is propagated and its velocity measured is 45° to the c-axis and a-axis, where $n_1 = n_3 = 2^{-1/2}$ and $n_2 = 0$. Substituting these n

values into equation 2.3 gives the solution for the transverse wave with polarisation along the b-axis;

$$\rho v^2 = (C_{11} - C_{12} + 2C_{44})/4 \qquad (2.6)$$

And the combination of the transverse and longitudinal wave solution is;

$$\rho v^2 = (C_{11} + C_{33} + 2C_{44})/4 \pm [((C_{11} - C_{33})/2)^2 + (C_{13} + C_{44})^2]^{1/2} \qquad (2.7)$$

and hence the determination of C_{13}.

From the above discussion we see that the elastic moduli for the hcp crystal, i.e. C_{11}, C_{33}, C_{44}, C_{12} and $C_{66} = \frac{1}{2}(C_{11} - C_{12})$ can be obtained from the longitudinal and shear velocities measurements with wave propagated down the principal axes of the crystal. Due to the size of the samples it was not possible to do a 45° cut between the c and a axes, thus C_{13} was not measured.

Apart from the losses at the transducer-sample boundary, changes in the acoustic wave characteristics can be caused by several interaction mechanisms as discussed by Truell *et al.* (1969). The interactions which are significant and relevant to this work are; the direct scattering at the boundaries and the magnetoelastic losses due to domain wall motion, domain rotation and spin-phonon effects. In the review by Bar'yakhtar and Turov (1988) they have indicated that although generally the magnetoelastic interaction

is small it can have significant effects at magnetoacoustic resonance in magnetic systems having magnetic anisotropy and at magnetic phase transitions. Magnetoacoustic resonance occurs when the frequencies and wave vectors of magnons and phonons having the same symmetry coincide. Magnetoacoustic frequencies are typically ~ 10^9 Hz, well above the frequencies involved in this work ~ 10^7 Hz. The theory on the magnetoelastic interaction in ferromagnets are discussed by Povey *et al.* (1980) and Buchel'nikov and Vasil'ev (1992). The acoustic generation in ferromagnets was shown to be contributed by two main types of process; at low applied magnetic field the acoustic generation is dominated by the spin-lattice coupling as a result of domain wall motion and domain rotation whereas a modified Lorentz mechanism dominates in the high field regime.

2.2 Ultrasound Measurement Techniques

In this section different ultrasound measurement methods are introduced and discussed. Ultrasound measurement systems can either function in the pulse-echo mode or continuous wave (cw) mode. The discussion in this section concentrates only on ultrasound measurement techniques working in the pulse-echo mode.

In the pulse echo mode, ultrasound is generally produced as burst of pulses, generally in the form of a tone-burst (packet of acoustic energy). A tone-burst pulse consist of one or more wave cycles. The width of the tone-burst is determined by the number of cycles in the pulse. The tone-burst frequency is the resonant frequency (or

close to the resonant frequency) of the acoustic transducer. The preferred tone-burst profile, i.e. the shape enveloping the wave cycles, is a Gaussian wave envelope which provides a continuous frequency domain.

The detection of the acoustic wave can either be by the same generating transducer or by a different receiver transducer. In this work the so-called send-receive mode is used with one transducer both sending and receiving. The through transmission method is preferred for highly attenuating samples. In most cases amplification of the received signal is necessary. Several amplifications stages and filters may be used to improve the signal to noise ratio.

Ultrasound measurement techniques can be designed to; (a) be highly sensitive to velocity and attenuation changes or (b) measure accurately absolute velocities. In this work the interest is in the detection of velocity change, $\Delta v/v = 0.001$. Several methods are described below starting with the pulse echo overlap technique.

2.2.1 Pulse Echo Overlap Technique

The pulse echo overlap technique is a very sensitive and high precision technique. In aim is to measure the time of flight of the ultrasonic pulse echoes. The time of flight is defined as the time taken by the ultrasonic pulse to travel from the acoustic transmitter, through the sample, to the receiver. The sample is prepared with two parallel surfaces and in pulse echo mode. The transducer is placed on one of these

surfaces and attached to the sample with an acoustic couplant, e.g. ultrasonic gel. The ultrasonic pulse is transmitted from the transducer through the acoustic couplant and into the sample. The acoustic couplant allows most of the ultrasound energy to be transmitted into the sample. The ultrasonic pulse then propagates through the sample until it reaches a boundary, an acoustically mismatched surface where most of the ultrasound energy is reflected back into the sample. The ultrasonic wave then propagates through the sample again before reaching the tranducer via the acoustic couplant. The total time taken, including electronic delays, is the time of flight of the pulse echoes.

The basic setup of a pulse echo overlap system is shown in figure 2.3 as described in Hellier *et al.* (1974). A frequency synthesizer triggers the x-axis of the oscilloscope and this is frequency divided at a decade fraction. This is then use to trigger the RF generator which in turn pulse the acoustic transducer. In the transmission mode two transducers are used; one as a transmitter and the other as a receiver transducer. The transducers are placed on opposite sides of the samples surface. The received acoustic signal is then amplified and fed into the y terminal of the oscilloscope. When the repetition rate of the frequency synthesizer, after adjustment, matches the propagation time of the ultrasound signal through the sample plus electronic delay the ultrasound pulse echoes appear to be overlapped on the display screen of the oscilloscope. The oscilloscope display is enhanced by feeding part of the output for the frequency divider into the z mod of the oscilloscope. This increases the brightness over the two overlapping pulse echoes. The time of flight of the pulse echoes is obtained from the inverse of the reading on the frequency meter.

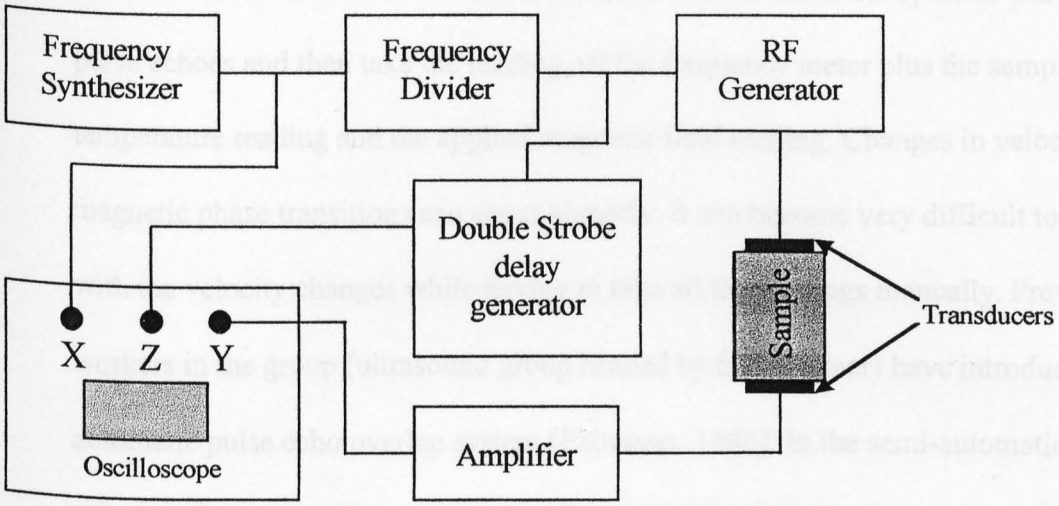

Figure 2.3. Pulse echo overlap system described in Hellier *et. al.* (1975).

The use of a manual pulse echo overlap ultrasound measurement system in this work is tedious and labour intensive. For each measurement the operator has to align the pulse echoes and then take the reading off the frequency meter plus the sample temperature reading and the applied magnetic field reading. Changes in velocity close to magnetic phase transitions can occur abruptly. It can become very difficult to keep track with the velocity changes while having to take all the readings manually. Previous workers in the group (ultrasound group headed by S.B. Palmer) have introduced a semi-automatic pulse echo overlap system [Patterson, 1986]. In the semi-automatic pulse echo overlap system the operator is only required to align the pulse echoes and manually activating a PC to capture and store the frequency readings and the sample temperature readings.

2.2.2 Sing Around Technique

In the sing around technique a feedback mechansim is used to measure the time of flight of the ultrasound pulse echoes. A transducer is used to generate the ultrasound while another is used as a receiver. An initial rf pulse is used to trigger a pulse generator to generate the ultrasound. The received signal is then amplified and fed back to the pulse generator to produce another pulse. Ultrasonic pulses are thus generated and transimitted through the sample continuously. The reciprocal of the repetition rate is the time taken for the pulse to travel through the sample plus the electronic delays. Absolute velocity measurement is seldom possible because of the difficulty in eliminating the

electronic delays. The sensitivity of the system is typically $\Delta v/v \approx 10^{-5}$ [Jiles, 1979]. The system used by Jiles (1979) was not automated.

2.2.3 Automated Ultrasound Measurement System

One automated ultrasound measurement system designed and constructed by former workers of this group not only uses a PC to control the experimental parameters and to acquire and store data, it also can determine the time of flight of the pulse echoes [Eccleston, 1991]. Communications between PC and the instruments is via the IEEE 488 interface bus. This system was a leap forward from previous ones.

A transducer is repeatedly pulsed by a Matec tone-burst generator at fixed frequency, pulse width and output voltage. The ultrasonic waveform was then captured using a Hewlett-Packard (HP54201A) digital storage oscilloscope. Two successive pulse echoes are selected, i.e. time base of the digital oscilloscope adjusted to display only two pulse echoes on the display screen. The data capacity per trigger is 1000 data points. The data are then transferred to the PC. Once in the PC the data are processed to extract the time of fight of the pulse echoes. To do this the algorithm looks for the zero crossing (V=0) points of the cycles in each pulse. A quadratic function is then fitted over the data points. The root (real part) of the quadratic function gives the zero crossing point in the time domain. The time of flight of the pulse echoes are determined by matching the zero crossing points of each cycle with the corresponding cycles in the

successive pulse echo. The difference in the roots for each pair of cycles, Δt, are then determined and the average value calculated. The system used by Eccleston (1991) can also work out the ultrasonic attenuation by measuring the relative change in amplitude of the two selected pulse echoes.

The inherent problem with the system, or any automated system, is the reliance on well defined and non-distorted pulse echoes. Error can be easily introduced in the velocity and attenuation measurements. For example the method of attenuation measurement described above assumes that an exponentially decaying function can be fitted over a series of ultrasonic pulse echoes in the ultrasound waveform. Any mode converted waves running through the waveform can interfere with the main pulse echoes and the envelope of the pulse echoes is no longer an exponentially decaying function. A commonly used method of ultrasonic attenuation measurement is to fit an exponential function over several pulse echoes in the pulse echo train as they are being displayed on the oscilloscope. Fitting is carried out by varying the time constant on the function generator producing the exponential function. The quality of fit is rarely perfect and is subject to the discretion of the operator.

Similarly the error in the velocity determination can result from the distortion of the pulse echoes. In such circumstances the zero points for each cycles can not be paired up correctly. It must be pointed out that even a manually operated system, such as the pulse echo overlap system, requires reasonably well defined pulse echoes for the cycles to be matched (overlapped) accurately. In a manually operated system the accuracy of the alignment and measurements are again in the discretion of the operator.

2.3 Physical Properties Of Rare Earth Elements

This is a generic section introducing the rare earth elements of erbium and thulium. For a detailed description of the physical and chemical properties of the rare earth the reader can refer to the Handbook on the Physics and Chemistry of Rare Earth (Gschneidner and Eyring, 1978). A comprehensive description of the electronic structure of these elements and their alloys are reported by Coqblin (1977). Details of the magnetic properties of rare earth metals can be found in Elliot (1972).

The rare earth elements, also referred to as the Lanthanide series, starts with Lanthanum with atomic number 57 and ends with Lutetium having atomic number 71. The atomic radii, defined as half the distance between nearest neighbours, range from 1.83 Å to 1.73 Å going across the series and this change in atomic radii is approximately linear [Hall *et al.*, 1963]. A majority of the rare earth elements have the hexagonal close-packed (hcp) structure, including Er and Tm. The lighter elements, atomic number < 64, have the double hexagonal close-packed (dhcp) structure. The non hcp or dhcp structure elements in the series are Ce, Sm, Eu and Yb. Sm and Eu have rhombohedral and body-centred cubic respectively. Ce has the γ face-centred cubic (fcc) at normal temperature and pressure but can change into the α fcc at low temperature or at high pressure. Yb has a fcc structure at room temperature and normal pressure. The consistency of the crystallographic structures and the atomic radii suggest the similarity

in their chemical properties which contributed to much of the difficulties in the purification process. Some of these elements are not rare at all but due to the difficulties encountered in the purification process they are labelled rare earth elements. In most circumstances, the electronic configuration of these elements is; $4f^n$, $5d^1$, $6s^2$, where n can take the number 0 to 14. In general, the 4f wave functions from the nearest neighbours do not overlap and the 4f orbital is at least 10 times smaller than the atomic radius. The relatively small 4f shell makes it possible to treat the atoms as isolated trivalent ions. The distribution of the conduction electrons is as follows; one electron in the 5d shell and two electrons in the 6s shell. The distribution of the 4f electrons follows Hund's rule. The magnetic moment is given by; $\mu = \mu_B g_J [J(J+1)]^{1/2}$, where μ_B is the Bohr magneton, g_J the Landé factor defined as;

$$g_J = 1 + \frac{J(J+1) + S(S+1) - L(L+1)}{2J(J+1)}$$

and J the total angular momentum with J = L - S for light elements (atomic number < 64) and J = L + S for heavy elements. L and S are the orbital and spin angular momentum respectively. Er and Tm, being heavy rare earth metals have their total angular momentum described by J = L + S. This gives: (a) Er; S = 3/2 and L = 6 hence J = 15/2 and (b) Tm; S = 1, L = 5, J = 6. The theoretical magnetic moment are: $9.6\mu_B$ and $7.6\mu_B$ for Er and Tm respectively, while the measured values are $9.5\mu_B$ and $7.62\mu_B$ [Coqblin, 1977]. The very good agreement between the theoretical and the experimental values of the magnetic moments suggest that the assumption of the rare earth metals to

behave like independent trivalent ions is valid (only to the first approximation). The 4f electrons thus dictate the magnetic properties of the metals.

Er has a metallic grey appearance with density $\rho = 9.145$ gcm^{-3}. The lattice parameters are; a = 3.539 Å and c = 5.6 Å [Klemm ,1937]. The magnetic structure of the rare elements have been extensively studied using x-rays and neutron diffraction methods. The phase diagram of Er has been constructed by several workers with the early work performed by Cable *et al.* (1961) on poly-crystalline samples of Er. Improvements in the metal purification process provided sufficient quantity of starting material at reasonable cost for the production of single crystals. In the pioneering work on Er reported by Cable *et al.* (1965) three distinct magnetic phases were observed apart from the room temperature paramagnetic phase. The Néel temperature of Er is at 87 K with the magnetic moments aligned along the c-axis and sinusoidally modulated. Detailed studies conducted by Habenschuss *et al.* (1974) and Atoji *et al.* (1974) showed the change in the modulation of the moments as a function of temperature. Initially the anti-ferromagnetic phase exhibits a modulation period of just under 8 atomic layers at 84 K, q=1/4 to just under seven atomic layers at 52 K, q =2/7. The next distinct phase identified by Cable *et al.* (1965) is between 54 K and $T_c = 18$ K. A basal plane component is observed which has the same period of modulation as the c-axis components. High resolution synchrotron x-ray scattering studies reported by Gibbs *et al.* (1986) provided evidence of lock-in transitions with q = 1/4, 6/23, 5/19, 4/15 and 2/7. Below the Curie point the magnetic moments are aligned with a cone ferromagnetic structure. Recent work by Cowley and Jensen (1992) provide detailed discussion on the structure of the intermediate magnetic phases observed between 18 K and 52 K. The c-

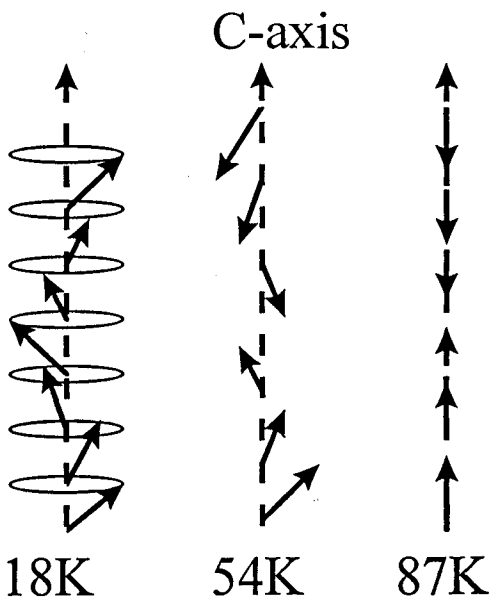

Figure 2.4. Magnetic ordering of Er. Néel temperature occurs at 87 K with magnetic moment aligned and modulated along the c-axis. Basal plane magnetic moment develops at 54 K. T_c = 18 K with magnetic moment having the cone structure.

axis magnetic phase diagram of Er has been constructed by McMorrow *et al.* (1992), showing the complexity of the magnetic structure between 18 K and 52 K. The three distinct magnetic ordering structures of Er are shown schematically in Figure 2.3.

Other experiments besides the neutron and synchrotron x-ray diffraction studies have been performed on Er, i.e. ultrasound [Eccleston *et al.*, 1992], thermal expansion and magnetostriction [Zochowski *et al.*, 1995], ac susceptibility and resistivity [Watson *et al*, 1995] and magnetisation [Snigirev *et al.*, 1992]. Note that the ultrasound studies conducted by Eccleston *et al.* (1992) used quartz transducers for the acoustic generation whereas in this work the focus is on EMATs and can be considered as a further extension to the studies reported by Eccleston *et al.* (1992).

Tm has similar physical properties to Er. Its density is 9.325 gcm^{-3} and the crystal parameters are a = 3.530 Å and c = 5.575 Å [Klemm ,1937]. The early studies of the magnetic structure of Tm were conducted by Koehler *et al.* (1962) using neutron scattering techniques. These studies reported the paramagnetic to antiferromagnetic transition occurring at 56 K, at zero field. Similar to Er, the magnetic moments are sinosoidally modulated along the c-axis. The magnetic moment squares up along the c-axis below 40 K and at temperatures below 32 K Tm becomes ferrimagnetic, see figure 2.4. In the ferrimagnetic phase the moments are aligned along the c-axis such that the sequence of the magnetic moments are 4 layers up and 3 layers down. If an external field greater than 2.8 T is applied parallel to the c-axis the ferrimagnetic phase is transformed to a ferromagnetic phase. The total momentum is described by J = 6, implying S = 1 and L = 5. The theoretical magnetic moment per atom at 0 K is $7.6\mu_B$

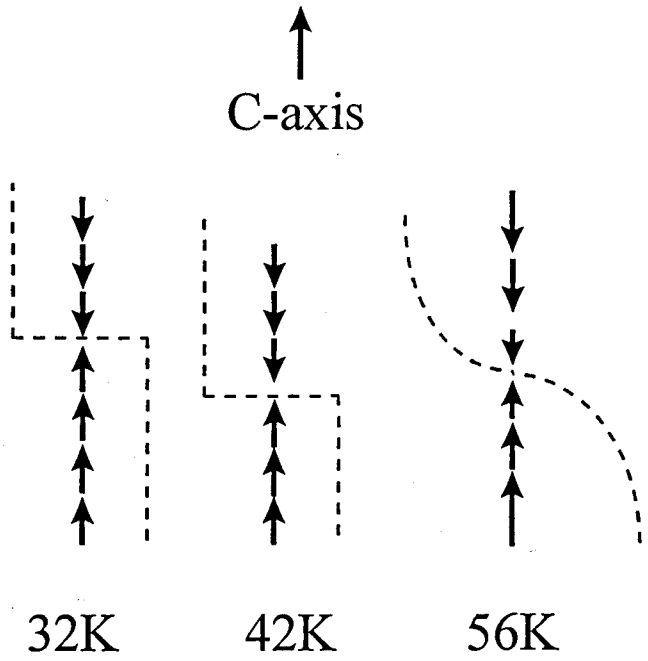

Figure 2.5. Magnetic ordering of Tm. Ferrimagnetic ordering below 32 K. Square-up antiferromagnetic ordering at 42 K. C-axis modulated antiferromagnetic ordering at 56 K.

[Coqblin, 1977]. The measured magnetic moment per atom was 7.06μ_B in the ferromagnetic state and 1.025μ_B in the ferrimagnetic state [Åström *et al.* , 1991]. The magnetic phase diagram of Tm has also been constructed from thermal expansion and magnetostriction data [Zochowski and McEwen, 1992] [Willis and Ali, 1991]. Detail of the magnetic structure in the ferrimagnetic as well as the ferromagnetic phase have been reported by McEwen *et al.* (1995), Steigenberger *et al.* (1992) and McEwen *et al.* (1991) using neutron diffraction. Bohr *et al.* (1990) reported the use of synchrotron x-ray diffraction for the study of magnetic ordering in Tm.

There have been no reported ultrasound measurements for Tm and this work is the first study of the magnetic properties of Tm using ultrasonic techniques.

References

Atoji M. 1974, Solid State Commun., **14**, pp1047.

Åström H.U., Nogues J., Nicolaides G.K., Rao K.V. and Benediktsson G. 1991 J. Phys.: Condens. Matter **3**, pp7395-7402.

Bar'yakhtar and Turov 1988, *Spin Waves and Magnetic Excitations Vol. 2*, Elsevier Science Publishers.

Bohr J., Gibbs D.and Huang K. 1990, Physical Review B, **42,** no.7, pp4322-4327.

Buchel'nikov V.D and Vasil'ev A.N. 1992, Sov. Phys. Usp., **35**, no.3, pp192-211.

Coqblin B. 1977, *The Electronic Structure of Rare-Earth Metals and Alloys: the Magnetic Heavy Rare-Earths*, Acadamic Press.

Cowley R.A. and Jensen J. 1992, J. Phys. Condens. Matter **4** pp9673-9696.

Eccleston R.S. and S.B. Palmer 1992, J. Magnetism and Magnetic Materials, **104-107**, pp1529-1530.

Edit. by Elliot R.J. 1972, *Magnetic Properties of Rare Earth Metals*, Plenum Press, chpt 3.

Gibbs D., Bohr J., Axe J.D., Moncton D.E. and D'Amico K.L. 1986, Phys. Rev. Lett. **55** pp234.

Edit. Gschneider K.A Jr. and Eyring L.R 1978, *Handbook On The Physics And Chemistry Of Rare-Earths,* North-Holland.

Habenschuss M., Stavis C., Sinha S.K. Deckman H.W. and Spedding F.H. 1974, Phys. Rev. B **10**, pp1020.

Hall H.T., Barnett J.D. and Merrill L. 1963, Science, **139**, pp111.

Hellier A.G., Palmer S.B. and Whitehead D.G., 1975, J. Phys. E, **8**. pp 352 - 354.

Jiles D.C. 1979, PhD Thesis, University of Hull.

Koehler W.C., Cable J.W., Wollan E.O. and Wilkinson, M.K. 1962, Phys. Rev. B **126**, pp1672.

Klemm, B., Z. Anorg. Chem., 1937 **231** pp150.

McEwen K.A., Steigenberger U. and Jensen J. 1991, Phys. Rev. B, **43**, no.4, pp3298-3310.

McEwen K.A., Steigenberger U. Weiss L. Zeiske T. and Jensen J. 1995, J. Magnetism and Magnetic Materials, pp767-768.

McMarrow D.F., Jehan D.A., Cowley R.A., Eccleston R.S and McIntyre G.J. 1992, J Phys.: Condens. Matter, **4**, pp8599-8608.

Musgrave M.J.P. 1970, *Crystal Acoustics. Intro. To The Study Of Elastic Waves And Vibrations In Crystals.* Holden-Day.

Palmer S.B., E.W. Lee and M.N. Islam 1974, Proc. Roy. Soc. Ser. **A338**, pp341.

Patterson C. 1986 , PhD Thesis, University of Hull.

Povey M.J.W., Meredith D.J. and Dobbs E.R. 1980, J Phys. F: Metal Phys., **10** pp2041-53.

Steigenberger U., McEwen K.A., Martinez J.L. and Jensen J. 1992, Physica B, **181**, pp158-160.

Snigirev O.V., Tishin A.M. and Volkozub A.V. 1992, J. Magnetism and Magnetic Materials, **111** pp149-152.

Truell R., Elbaum C. and Chick B.B. 1969, *Ultrasonic Methods in Solid State Physics*, Academic Press, chpt 1.

Willis F. and Ali N. 1991, J. Appl. Phys. **69**, no.8, pp5697-5699.

Zochowski S.W. and McEwen K.A 1992, , J. Magnetism and Magnetic Materials, **104-107**, pp1515-1516.

Zochowski S.W. and McEwen K.A 1992, , J. Magnetism and Magnetic Materials, **140-144**, pp1127-1128.

Chapter 3

Ultrasound Measurement System and Experimental Method

3.0 Introduction

This chapter describes the instrumentation and the experimental procedure used in the present work where the aim of this work was to set up an automatic ultrasound measurement system that allows for velocity and attenuation measurements as a function of (1) temperature, (2) applied magnetic field and (3) ultrasonic frequency. Before proceeding to describe the system and the modifications made to the original Matec DSP-8000 software, the shortfall of the original system needs to be addressed first. To achieve the aim of the work a Matec DSP-8000 ultrasound measurement system had to be combined with an Oxford Instrument cryogenic and super conducting magnetic system. The DSP-8000 was not designed to work with the Oxford Instruments cryogenic and super conducting magnet system. The DSP-8000 software was designed only to work with a Lakeshore temperature controller and had the limited facility of controlling only one thermal sensor. As discussed later in this chapter it was found necessary to introduce an additional thermal sensor to read the sample temperature accurately. The original DSP-8000 software had no provision for magnetic field control. Filters on the A/D card were not activated in the original software. The reason for the filters not to be implemented is because the DSP-8000 system is designed to be used over a wide frequency range, several Hz to tens of MHz.

The schematic of the experimental set-up is shown in figure 3.1. The ultrasound measurement system consisted of ; (1) cryostat with super-conducting magnet, (2) tone-burst generator, (3) digitiser (A/D convertor), (4) amplifiers, (5) PC running a modified version of the Matec DSP-8000 software and (6) transducers.

3.1 The Cryostat And Superconducting Magnet.

The cryostat is a dynamic gas flow type. Figure 3.2 shows a schematic cross section of the cryostat. The cryostat has an outer protection casing and adjacent to this is a thin wall vacuum region. In the centre is the Variable Temperature Insert (VTI). The VTI unit consists of a sample space, heater coils, a temperature sensor and a needle valve. The needle valve controls the helium flow rate. A servo motor is mounted on top of the VTI to drive the needle valve. Liquid helium is stored in the lower section of the cryostat with the superconducting solenoid submerged in the liquid helium. In normal operation, the low temperature end is at liquid helium temperature of 4.2 K. A lower temperature of ~ 1.5 K can be achieved by pumping on the sample space, i.e. increasing the helium flow rate and this decreases the vapour pressure above the liquid hence lowering its temperature. Heating is provided by a 80 W heater coil mounted on a copper block positioned at the bottom end of the VTI. The sample is placed on a sample holder which is attached to a sample stick. The sample stick is inserted into the central bore of the VTI.

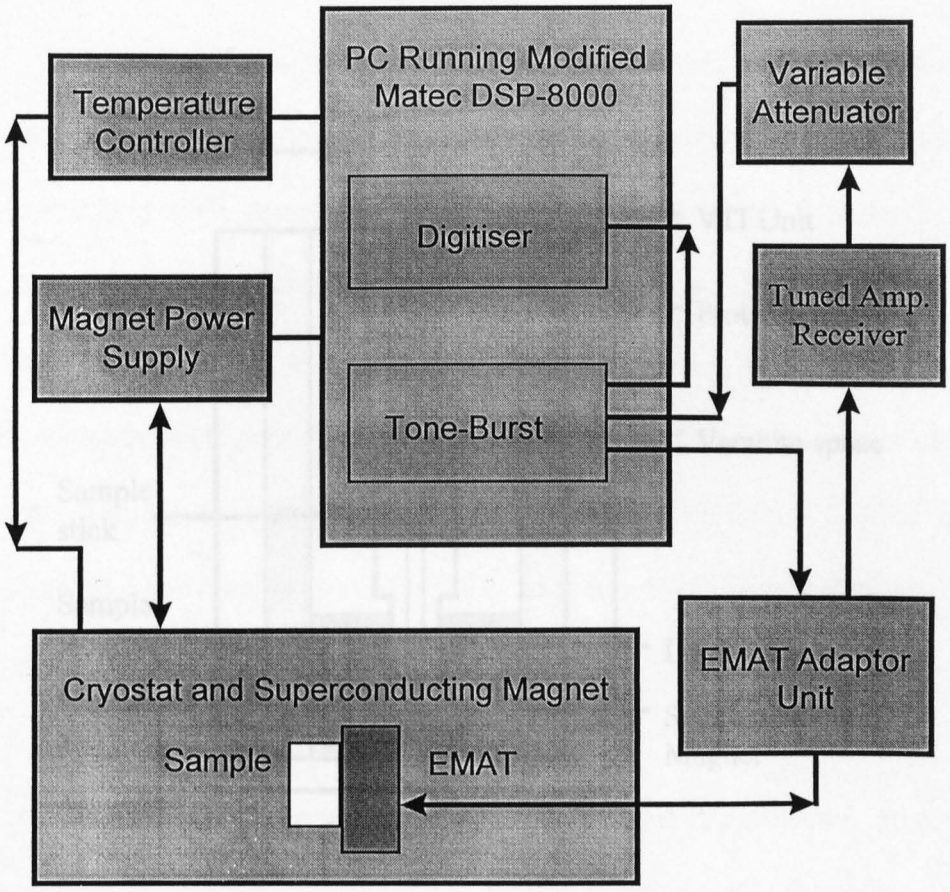

Figure 3.1. Schematic of experimental set-up.

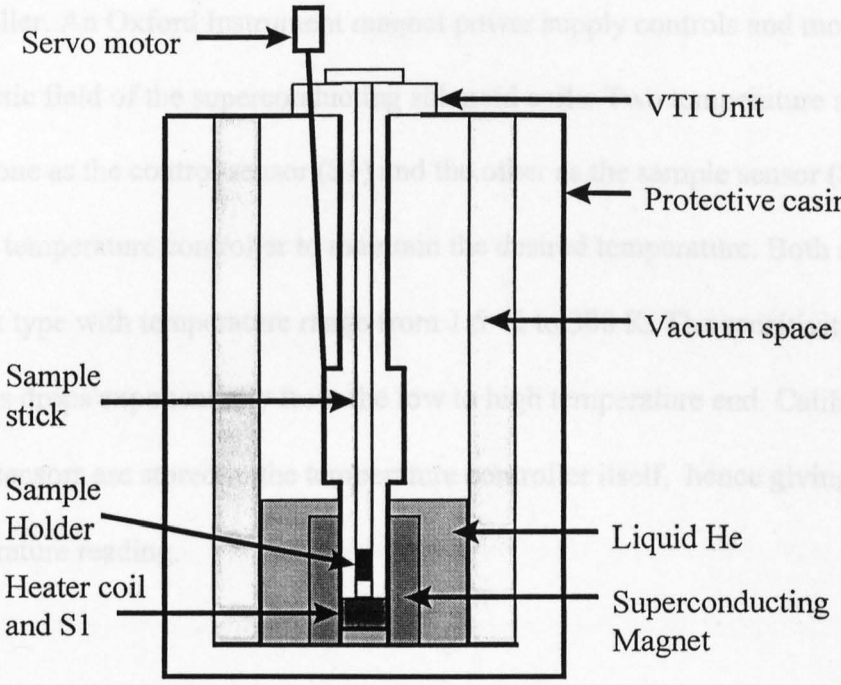

Figure 3.2 Schematic of cryostat and superconducting magnet.

The cryostat is controlled by the Oxford Instrument ITC503 temperature controller. An Oxford Instrument magnet power supply controls and monitors the magnetic field of the superconducting solenoid coils. Two temperature sensors were used; one as the control sensor (S1) and the other as the sample sensor (S2). S1 is used by the temperature controller to maintain the desired temperature. Both sensors were the cernox type with temperature range from 1.5 K to 300 K. The sensitivity of these sensors drops exponentially from the low to high temperature end. Calibration tables for these sensors are stored in the temperature controller itself, hence giving a direct temperature reading.

The temperature controller controls the accuracy, stability and response time of the cryostat. A feed back loop activates the heater voltage and the needle valve. First it looks for the difference between the set temperature and the temperature reading returned by the control temperature sensor, S1. A temperature difference $\Delta T = T_{control\ sensor} - T_{set}$ is then obtained. The voltage applied across the heating coils is proportional to ΔT. If ΔT is non zero and negative the heater voltage is increased, otherwise the opposite occurs. A temperature range is defined such that the voltage across the heater coil is proportional to ΔT. The heater voltage is set to either full or zero, depending on the sign of ΔT, when the temperature lies outside the temperature range. This temperature range is referred to as the proportional band and can be adjusted to suit the behaviour of the cryostat. There is an optimum proportional band for a given cryogenic system. If the proportional band is set too small, temperature oscillations occur. It is kept large enough to prevent oscillations but this introduces residual error which results

in increased time to reach the set temperature and can become impractical. To overcome this, the error voltage is fed into an integrator and the output from the integrator is then added to the heater voltage. This is repeated until the error is within the set tolerance. The integrator itself can cause oscillations which can be prevented by making sure that the time taken for the voltage to swing from fully on to zero in the presence of a fixed error in the proportional band is twice the response time constant of the cryostat. A third control parameter determines the rate of change of the temperature. This is referred to as the derivative action. For all measurements carried out in this work the default factory settings of the proportional, integral and derivative values were used. Hence in remote operation, only the desired temperature value is sent to the temperature controller and the rest of the temperature control operations were left to the temperature controller.

3.2 Tone-Burst Generator (Matec TB-1000)

The tone-burst generator used is a 16-bit 100% IBM compatible plug-in card providing a frequency range of 0.5 MHz to 20 MHz with 200V peak to peak output voltage. A gated receiver with filters was built on the board. The gain on the gated receiver can be software controlled from 0 to 70.0 dB. Other computer controlled features are the tone burst pulse width, tone burst repetition rate, the filter range and the rectification modes. The triggering was set to internal and triggers on the positive slope. All work were carried out with pulse repetition rate at 1 kHz and no rectification.

3.3 Digitiser (SR-9010)

The sampling rate of the digitiser card can be selected via software, between 781 kHz to 100 MHz in the normal mode of operation but this can be as high as 800 MHz in equivalent time sampling mode. In the normal mode of operation the digitised data (maximum of 64 Kbytes) were stored directly into the PC's memory through direct memory accessing (DMA), whereas in the equivalent time sampling mode, e.g. 800 MHz, the waveform had to be captured 8 times. Each time the TTL trigger is delayed by a set value. The waveform can then be merged, through software, by interleaving the 8 data sets. A 800 MHz sampling rate can thus be achieved from a basic clock rate of only 100 MHz.

3.4 Amplifiers

The returning signal was amplified by three different amplifiers. The first amplifier in the return line was the EMAT adaptor box. The EMAT adaptor box had a broad band amplifier with maximum gain of 50 dB peaked at 10 MHz. To reduce the noise level, the output from the pre-amplifier was fed into a narrow band tuneable receiver amplifier, with ~ 50 dB gain in the region of 10 to 15 MHz. The receiver gain on the tone-burst card was software controlled from 0 to 70 dB. The sensitivity of the A/D was kept between +2 to -2 V.

3.5 The Control and Processing Software

The functions of the control software are; (1) sets and checks the experimental parameters before data acquisition, (2) activate tone-burst and acquire data and (3) process and stores data. Communications between the PC and the instruments are via an IEEE-488 GPIB (General Purpose Interface Bus). All instruments shown in figure 3.1 can be computer controlled apart from the EMAT adaptor box, the tuned receiver amplifier and the attenuator. Modifications had to be made to the original Matec DSP-8000 software for it to be useful in this work. The following modifications and changes were made;

(1) to control Oxford Instruments (OI) ITC503 temperature controller,

(2) to control OI superconducting magnet power supply,

(3) to activate the high pass filters on the tone-burst generator card,

(4) to store the captured data

(5) to record and store readings from an additional temperature sensor, S2, mounted on the sample holder.

The software was written in C++ for Windows and compiled with a Borland C++ 4.5 compiler. Since the original software was not written in-house, the documentation on the software was very limited. This made the task of modifying the software a tedious one. In an object oriented programming language such as C++ a target file, i.e. file containing the file extension ".exe", is created by linking files (object

files) together. The set of codes contained in each of the object files performs a specific task, e.g. a global variable object file would contain codes defining variables which are shared by all the object files. In this example the object file performs the function of defining the global variables. There were forty one main object files and six libraries in the original DSP-8000 software. This excludes sub-files, i.e. object files linked to the main object files. The first task in the software modification process is to identify the function of each of the files linked to the executable target file. The function of some files were more obvious than others. Next the handling of data between the files had to be traced, i.e. to map the flow of information between the files. This tedious investigative work took several weeks and was further complicated by the fact that the worker on this project did not have any previous experience programming in C++ for the Microsoft Windows environment.

The description on how the software controls work is best described with an example and a flow chart. Figure 3.3 shows a software flow chart for a typical ultrasound measurement. On executing the software, the DSP-8000 file functions as the main Windows file. It reads the set-up file which contains the GPIB addresses for the instruments. It also reads the calibration table for the digitiser. On top of the main window is a list of menus. In performing an ultrasound velocity measurement as a function of temperature, the Exec menu is activated from the main window. This is shown as a lighly shaded box within the DSP-8000 box, see figure 3.3. The DSP-8000 file starts by checking the GPIB addresses of the GPIB board and the instruments connected to the computer. It then looks for the type of measurement to be performed and the mode of the ultrasound measurement, i.e. pulse-echo or transmission modes,

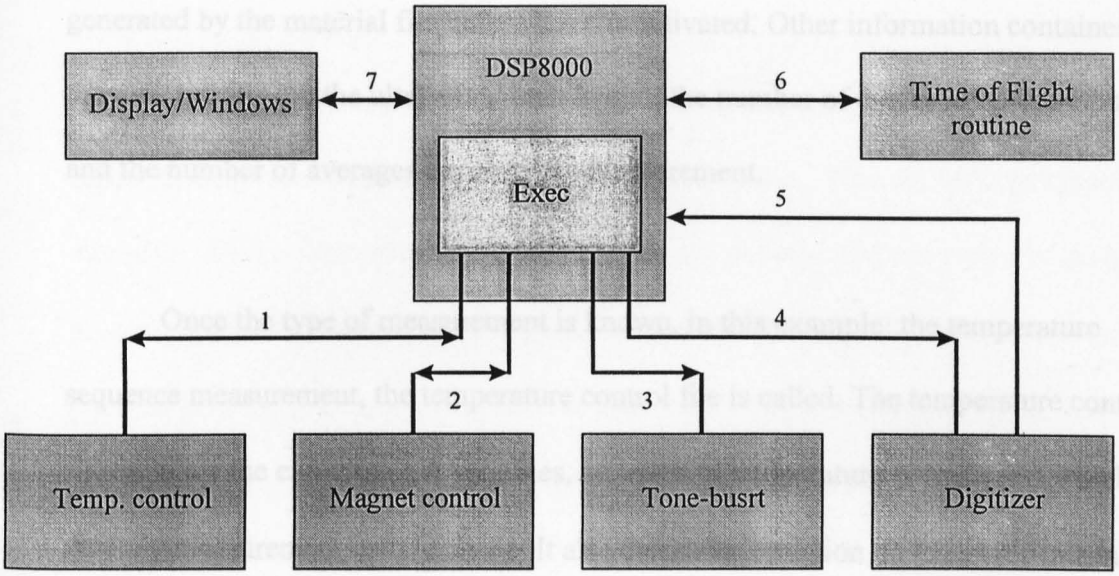

Figure 3.3. Software flow chart for a typical ultrasound mesurement. The shaded box represents an object file. Note that only the main object files are shown. The numbers indicate the order in which the different object files are called up.

which are listed in an object file called "material". This is not shown in figure 3.3. The relevant information is provided by the user in the appropriated dialogue windows generated by the material file before Exec is activated. Other information contained in the material file are the ultrasound path length, the number of cycles in the tone-burst and the number of averages required per measurement.

Once the type of measurement is known, in this example the temperature sequence measurement, the temperature control file is called. The temperature control file contains the experimental variables, i.e. a list of temperature set points at which the velocity measurement is to be made. It also carries information on the experimental constants. The experimental constants are the tone-burst frequency, tone-burst output voltage and the magnitude of the applied magnetic field. The temperature set points are defined by the user in the temperature setup dialog window before Exec is activated. These data are then sent to the appropriate instruments via the associated object files e.g. the magnet control file is called and the magnitude of the desired applied magnetic field is then passed onto the magnet power supply. The experimental conditions are checked before Exec call the tone-burst file which in turn activates the tone-burst generator and arms the digitiser. This triggers the digitiser to capture 8001 data points each time. The data are then transferred to the PC's memory by direct memory access (DMA). A location in the PC memory block had to be pre-defined for this purpose and has a fixed size and location. The data sets are captured repeatedly for the desired number of averages. In order for the time of flight to be determined by the auto-correlation algorithm only data points from two successive pulse echoes are required. This is

achieved by pre-defining two time gates over two successive pulse echoes. An initial run is necessary to locate the echoes and for the gates to be set.

The auto-correlation algorithm is not available from the vendor but a brief technical note from Technology Development Group Inc., Weston, MA. was made available. With reference to this technical note, the sequence of the tensor post signal processing is as follows: With two successive pulse-echoes the first pulse echo is referred to as the reference pulse and the later pulse echo is referred to as the second pulse. In a single pass through the sample the first pulse echo can be described as:

$$r_1(t) = p(t)*[(d(t)*b(t - t_o))*d(t)]*i(t - t_o) \qquad (3.1)$$

where p(t), d(t), r(t) and i(t) are functions for transmitted pulse, single-pass dispersion, back-wall reflection and receiver impulse response respectively. * denotes the convolution operator. The second pulse signal would contain all the functions convoluted in $r_1(t)$ plus a front wall reflection function f(t). The second pulse can be written as:

$$r_2(t) = r_1(t)*[(d(t)*b(t - t_o))*d(t)]*f(t - t_o) \qquad (3.2)$$

$$r_2(t) = r_1(t)*X(t) \qquad (3.3)$$

The "Tensor Post Processing" estimates the convoluted function of the dispersion and reflection functions; $X(t) = d(t)*b(t - t_o)*d(t)*f(t - t_o)$ since $r_1(t)$ and $r_2(t)$ are known. X(t) is narrow with width of only several ns. X(t) is then fitted to a parabola using a least

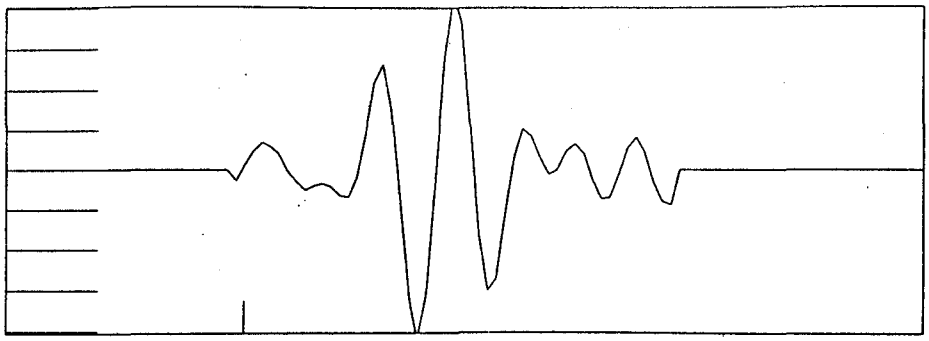

Figure 3.4a. Reference pulse.

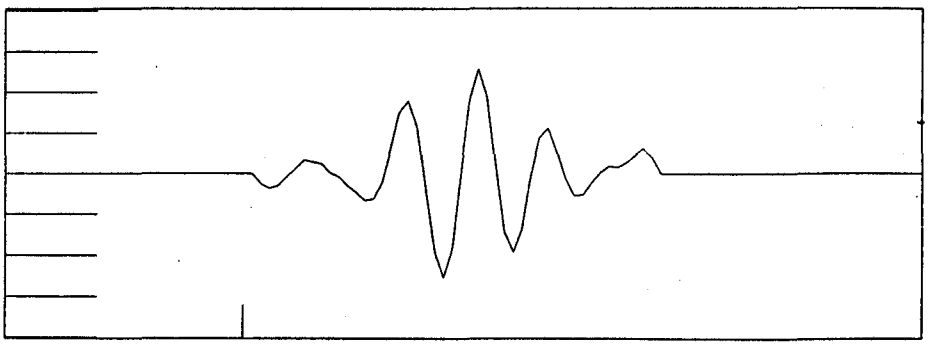

Figure 3.4b. Second pulse.

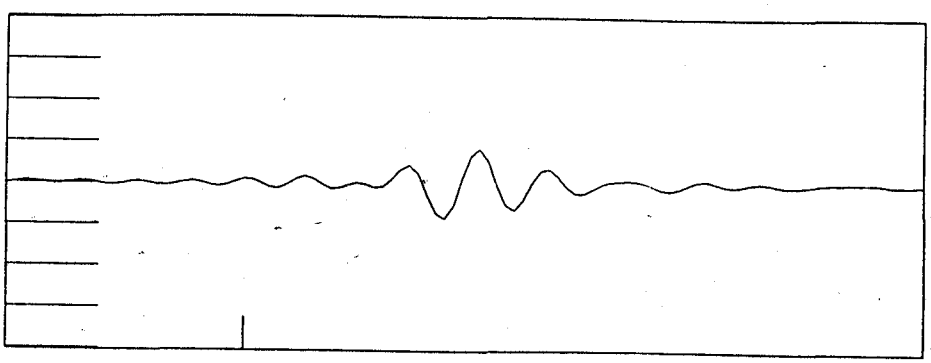

Figure 3.4c. Demodulated output waveform defined by X(t).

square fit. The apex time of the parabola gives the time of flight. Figure 3.4 a and 3.4 b show the reference pulse and the second pulse respectively from a typical ultrasound pulse-echo waveform. Figure 3.4 c shows the demodulated output waveform, i.e. X(t).

The time of flight algorithm was tested on samples with known acoustic velocities, e.g. aluminium. The data were then compared with those obtained manually using a digital oscilloscope (LeCroy 9410). Prior to the automated ultrasound measurement the time of flight measurements at room temperature were carried out to provide absolute velocity measurements which were then used to set the time gates for the automated ultrasound measurement system. This procedure had to be applied to all automated ultrasonic measurements involving a tone-burst as it is possible that the cycles are incorrectly matched. In most cases by ± 1 cycle which corresponds to an error of $\Delta t = 1/f$ in the time of flight. The present automated ultrasound measurement system has an absolute error of ± 0.001 μs in the time of flight measurement and a sensitivity of $\Delta v/v \sim 0.0005$.

3.5.1 Temperature control file

Described in this section are the modifications made to the C++ codes which control the temperature controller. The original software was designed to control a Lakeshore temperature controller but an Oxford Instruments (OI) temperature controller (ITC503) was used with the present system.

The algorithm of the original temperature control file was used. The modification is fairly straight forward. The Lakeshore commands were replaced with the OI ITC503 commands where necessary. Additional commands were required to set the ITC503 to perform automatic control on the heater current and the gas flow in the cryostat.

3.5.2 Magnet control file

The function of the magnet control file is to manage the data flow between the software and the magnet power supply. In contains codes controlling the dialogue windows through which the user pre-defines the magnitude of the desired applied magnetic field. The algorithm is based on the one used in the temperature control file. The super-conducting magnet energising and de-energising sequences are written into the codes. In order to change the magnetic field, the persistence mode is deactivated by bringing the supply current to equal the current in the solenoid. Only then can the heater switch be turned on allowing the circuit between the power supply and super-conducting coils to be closed. The magnetic field is then changed by either lowering or increasing the current in the super-conductor.

The inclusion of the magnet control file to form part of the execution file is not straight forward. Initialisation routines managed by the "hardware set-up" object file had to be changed to allow for the GPIB address for the magnet power supply to be defined

and stored. This also meant that the dialogue windows for the hardware set-up had to be changed to include an extra input box for the magnet power supply GPIB address to be defined.

Modifications were made to the material object file such that an option for magnetic sequence measurements is made available and the dialogue window associated with this file had to be changed. This was followed by adding codes in the Exec file in order for it to recognise this additional measurement type.

Changes had to be made to the data storage codes in order for the magnitude of the applied field to be stored. The data display routines also had to be changed to allow for the magnetic field data to be displayed. Definitions of new global variables were added to the global object file.

3.5.3 Wave-form storage

The original software only allows the storage of the time of flight data as a function of frequency or temperature. The ultrasound wave-form can be displayed on the graph window with a normalised signal amplitude as a function of time. A hard copy can be obtained by printing the contents of the graph window but the raw data of the wave-form could not be stored. A simple routine was attached to the target file for this purpose. It stores the non-normalised wave data located in the memory buffer of the PC on to disk in binary format. This allows the captured ultrasound waveform, consisting of

the pulse-echo amplitudes in the time domain, to be stored for further analysis. The header of stored file contains the sample temperature, the receiver gain and the applied magnetic field information.

3.5.4 RF filtering

Another simple but useful change made on the software was the activation of the high pass filter on the receiver of the tone burst card. This was basically changing the RF filtering value found in the tone burst file header file. The filter was set to 5 MHz high pass since this work only concentrates on transducers operating over 5 MHz. This resulted in a substantial reduction in the noise level.

3.5.5 Temperature sensor (S2)

During test runs on the system it was found necessary to use an extra temperature sensor to measure the sample temperature. A temperature lead or lag always exists between the control temperature sensor and the sample temperature when a temperature sweep is performed on the cryostat. S2 was placed in thermal contact with the sample, see figure 3.5. Just before each measurements was taken Exec activates the temperature control file to read S2.

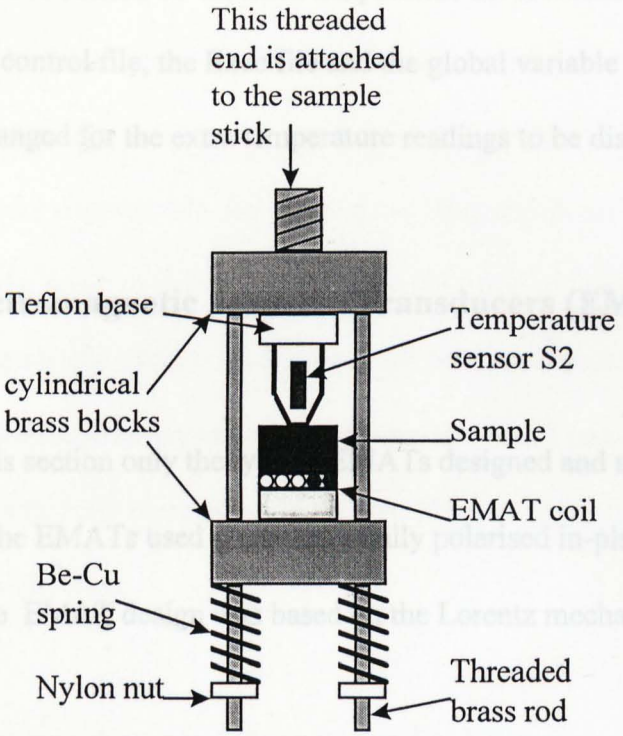

Figure 3.5. The sample holder.

The introduction of an extra temperature involves the modifications of: the temperature control file, the Exec file and the global variable file. Data display format had to be changed for the extra temperature readings to be displayed.

3.6 Electromagnetic Acoustic Transducers (EMATs)

In this section only the type of EMATs designed and used for this work are discussed. The EMATs used were the radially polarised in-plane shear and longitudinal EMATs. The EMAT design was based on the Lorentz mechanism.

When an electromagnetic (EM) wave is incident on the surface of a conductor most of the EM wave gets reflected and some penetrates below the surface but attenuates rapidly in the material. The depth to which the EM wave can penetrate is called the skin depth and is given by:

$$\delta = (\mu_o \mu_r \omega \sigma/2)^{-1/2} \qquad (3.4)$$

where μ_r and μ_o are the relative permeability and permeability of free space respectively, ω is the angular frequency and σ is the conductivity. At f = 10 MHz on aluminium, the skin depth is ~ 25 μm. The acoustic longitudinal wavelength at this frequency in aluminium ~300 μm. Now consider a current carrying wire placed close to the surface of a conductor producing a dynamic field **h** which is varying in time and space. An eddy current , with current density **J**, is induced within the skin depth of the conductor. The

eddy current is the mirror image of the current in the wire. A Lorentz force, **J** x **B**, is experienced by the conduction electrons, see figure 3.6. Due to the motion of the electrons the positive ions located are displaced from their equilibrium position and their motion are coupled into the lattice generating acoustic waves. The displacement direction of the positive ions depends on the direction of the static applied field. If **B** is normal to the sample surface shear waves are produced whereas if **B** is tangential to the sample surface longitudinal waves are generated. With a pan-cake coil configuration and a static magnetic field directed normal to the plane of the coil the generated shear wave is radially polarisation.

The reverse process applies when an EMAT is used as an acoustic detector. The propagation of ultrasonic waves in the material displaces the ions from their equilibrium position and this exerts a drag on the conduction electrons. In the present of a static applied magnetic field both ions and electrons experience a force (torque in the case of a pan-cake spiral coil) and generates a current density, say $\mathbf{J_R}$, in the sample. It is the generation of $\mathbf{J_R}$ associated with it an electric field $\mathbf{E_R}$, $\mathbf{J_R} = \sigma\mathbf{E_R}$, which is detected by the EMAT coil. As a general case, i.e. for any coil configuration, the EMAT is a velocity detector [Dixon, 1994]. Considering a free boundary sample surface the displacement of a particle in the z-direction can be defined as;

$$S(z,t) = S_o(e^{-ikz} + e^{ikz})e^{i\omega t} \qquad (3.5)$$

In most circumstances the skin depth $\delta << \lambda$ and $kz << 1$ and equation 3.6 can be approximated to;

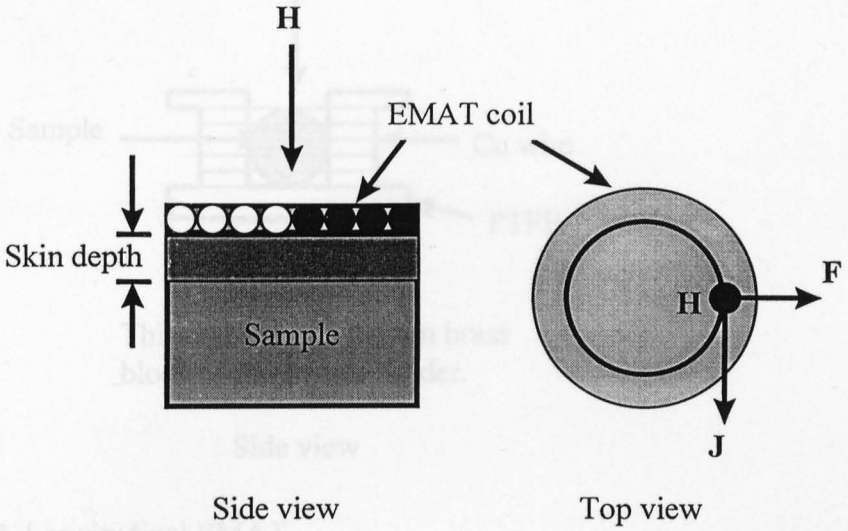

Figure 3.6. Spiral pan-cake coil EMAT. The white and dark shaded circles shown by the side view represents the circular coil with current direction out of the page and into the page respectively. Top view showing **H** directed into the page with only a single turn of the coil. **F** is radial and hence the polarisation is also radial.

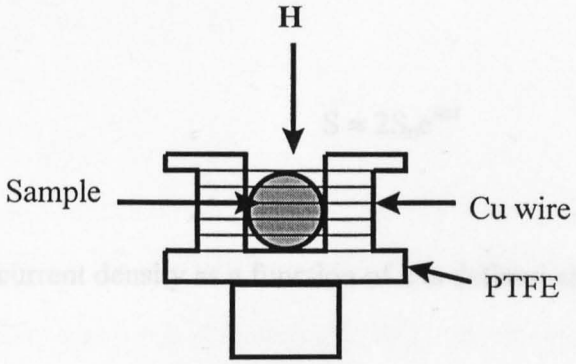

Figure 3.7. Longitudinal EMAT.

$$S \approx 2S_o e^{i\omega t} \tag{3.6}$$

The current density as a function of z is defined as;

$$\mathbf{J_R}(z) = \sigma(\partial S/\partial t \times \mathbf{B_o}) \tag{3.7}$$

since $\mathbf{J} = \sigma E$, where $\mathbf{E} = \mathbf{v} \times \mathbf{B}$ and $\partial S/\partial t = \mathbf{v} = i\omega S$ and if $\mathbf{B_o}$ is set perpendicular to $\mathbf{v}$ then equation 3.8 can be approximated to:

$$J_R \approx \sigma v B_o \tag{3.8}$$

which shows the dependent on the velocity of the particle in the sample. Detailed analysis of the EMATs generation and detection charateristics in non-magnetic materials have been reported by Kawashima (1976). This further differentiates EMATs from piezoelectric transducers where the latter are displacement sensors whereas the former is sensitive to the rate of change of displacement, i.e. velocity.

Detail discussions of the Lorentz mechanism can be found in Dobbs (1973), Kawashima (1976) and Frost (1979). Dobbs (1973) has shown in experiment and theory that the acoustic generation efficiency due to the Lorentz mechanism in non-magnetic metals is

$$\eta = \frac{2B_o h}{[\rho \omega V \delta (1 + \beta^2)]} \qquad (3.9)$$

where ρ is the density of the sample, $\omega = 2\pi f$ the angular frequency, V the sound velocity and $\beta = k^2\delta^2/2$ with $k = 2\pi/\lambda$, the wavevector, i.e. the depth variation of the driving force. The skin depth, δ, is defined by equation 3.4. The condition $\beta << 1$ is valid since the skin depth is confined close to the surface, showing the Lorentz acoustic generation efficiency being proportional to B_o.

In electrically conducting magnetic materials the situation is far more complicated. In addition to the Lorentz mechanism, domain rotation, domain wall motion, magnetoelastic effects and spin-flips are involved.

First the demagnetisation corrections have to be considered for magnetic samples since surface magnetic poles are formed on the samples and the internal field is a summation of the applied field and the demagnetizing field due to the surface poles. In the case of a paramagnet (permeability very close to unity) this effect is very small and can be ignored. In the case of a ferromagnetic where the permeability is large compared to unity the shape demagnetizing factor becomes very important and must be corrected for. The induced field with the demagnetisation correction is [Stratton, 1941]:

$$B = \mu_o H_o \left[1 + \frac{1}{N + \frac{1}{\mu_r - 1}} \right] \qquad (3.10)$$

where N is the demagnetisation factor, H_o the magnitude of the applied field and μ_r the relative permeability. This equation is valid provided the material does not magnetically saturate. The values of N for ellipsoids and cylinders are listed in Bozorth (1951). The Lorentz acoustic generation would then depend on B defined by equation (3.10). In addition μ_r is not a constant.

The theoretical treatment of the EMAT acoustic generation in ferromagnetic materials (Ni) have been reported by Povey *et al.* (1980) and for the rare earths (Gd and Dy) by Buchel'nikov and Vasil'ev (1992), Buchel'nikov and Shavrov (1991), Andrianov *et al.* (1988) and Andrianov *et al.* (1990). Povey *et al.* (1980) showed that the acoustic generation by the Lorentz mechanism in ferromagnets differs from the Lorentz mechanism applied to non-magnetic conductors. The EMAT acoustic generation efficiency, η, defined by equation 3.9, is multiplied by the term:

$$\Phi = 1 - \frac{[\omega_M (1 + i\alpha)]}{\Omega} \qquad (3.11)$$

where $\omega_M = \gamma M_S$, M_S the saturation magnetization, α the spin wave resonance damping parameter and $\Omega = \omega - \omega_s(1 + i\alpha)$ with $\omega_s = \gamma(H - H_S)$, i.e. the spin wave frequency. H and H_S are the static applied magnetic field and the saturation field respectively. $\Phi \rightarrow 0$

as $H \rightarrow H_S$ ($\omega \rightarrow \omega_M$) and a reduction in the Lorentz contribution as the material magnetically saturates. At high field $H > H_S$, $\Phi \rightarrow 1$ where it reverts back to the normal Lorentz mechanism as in non-magnetic conductors.

At low applied magnetic fields the magnetisation of a ferromagnet is dominated by domain wall motion. If the applied static field, $H_o << H_S$, and superimposed on H_o is the dynamic field from the EMAT coil, h, the domain walls within the skin depth would experience an oscillatory force which produces the bending of domain wall and domain wall motion. The bending of domain wall occurs if the distribution of the dynamic field is non-uniform within the skin depth. Both domain wall motion and domain wall bending generate acoustic waves in the sample. The transformation coefficient from domain wall motion to the acoustic wave is shown by Andrianov *et al.* (1990) to be:

$$\eta_d = \text{const.}\left[\frac{\chi^2}{(1+\chi)^2}\right] \tag{3.12}$$

where

$$\chi = \frac{\chi_o \omega_o^2}{(\omega_o^2 - \omega^2)} \tag{3.13}$$

ω_o is the natural oscillation frequency of the domain wall, χ_o is the static susceptibility of the domain wall motion. From equation (3.12) the acoustic generation would increase with increasing χ as a result of the increase of the static susceptibility of the domain wall, χ_o, and η_d also increases when $\omega \rightarrow \omega_o$.

In anisotropic ferromagnets the direction of the applied magnetic field, H_o, has to be considered. If H_o is along the easy direction, the magnetisation process first begins with domain wall motion which leads to the formation of a single domain where the magnetisation, M, is parallel to H_o. If H_o is along the hard direction of the magnet, two sets of domains are formed. A further increase in H_o induces the rotation of the domains to form a single domain. M in this case is not parallel to H_o. Further increases in H_o will align M towards the direction of H_o. In the presence of a dynamic field, h, and $H_o \rightarrow H_S$, the magnetisation M is modulated. A change in the magnetisation direction produces deformation in the sample (anisotropic magnetostriction). Since M is modulated acoustic waves are generated.

While the contribution of the magnetoelastic effects to the acoustic generation changes as a consequence of the dependence of χ, the Lorentz mechanism is dependent on the conductivity of the sample and the induced field, B (defined by equation (3.10)). The ratio of the magnetoelastic acoustic generation efficiency, η_{me}, to the Lorentz acoustic generation efficiency, η_L, is [Buchel'nikov and Vasil'ev, 1992]

$$\frac{\eta_{me}}{\eta_L} = \left(\frac{\beta \gamma \chi^2}{\mu_o \mu_r} \right)^2 \qquad (3.14)$$

β the depth variation of the driving force of the Lorentz mechanism (defined above), χ is a susceptibility tensor defined by $M = \chi H$, where the static and the ac magnetic fields are related to the magnetisation. γ is the volume magnetostriction constant containing

the exchange and anisotropy constants. The Lorentz contribution to the acoustic generation becomes significant when $\chi << 1$ and when the conductivity increases ($\beta \propto$ (conductivity)$^{-1}$).

The spiral pancake EMAT coils were wound from 0.08 mm diameter copper wire. Ideally they should be inductive however a capacitive component is always present arising from stray capacitance between the wires. This component increases with frequency. It is essential that the coils are still acting as a good inductance at the desired frequency. In this case the coils were matched as close to 50 Ω as possible at the driving frequency of ~ 10 MHz. The size of the sample used dictates the maximum diameter of the coils. The samples were grown and cut into cylinders with ~ 4 to 5 mm in length and diameter. The cylindrical axis was made perpendicular to one of the three principle hcp crystallographic axes. The coils were glued onto Tufnol bases which were machined to fit onto the sample holder as shown in figure 3.5. Using the condition of $2\pi fL = 1/2\pi fC$, where L is the inductance, C the capacitance and f the resonant frequency, the capacitance for the LC circuit was estimated and a capacitor close to this value was then connected in parallel with the EMAT coil. The coil, tuning capacitor and the sample to be tested were assembled together in the sample holder and the impedance of the circuit was tested with an impedance meter. The coils and capacitor value were adjusted to so that the EMAT remained inductive and was close to the 50 Ω input impedance at the required frequency. The whole assembly of coil, sample and capacitor plus the co-axial cables were cooled to 77 K to check for the change in the impedance. It was found necessary to tune the EMAT coil with the sample next to it since the inductance of the coil changes when placed next to a metal sample and this

change in the impedance depends on the metals conductivity and permeability. The capacitance of the co-axial cables were also considered in tuning the EMATs as this was significant with a cable length of ~ 2.5 m. The manufacturers quoted capacitance was ~ 154 pF/m at 5 kHz. With the present system the EMAT coil and the capacitor could not be tuned to compensate for the change in impedance as the temperature changes. After the tuning the circuit the EMAT coils were then glued onto the Tufnol base.

For longitudinal wave generation the EMAT coils were wound onto a PTFE base as shown in figure 3.7. The sample was placed in between the gap with one end near to the exposed wires. The number of turns was limited by the conditions mentioned above. Since less than one quarter of the coil was used for the generation of acoustic waves the EMATs acoustic coupling was not as efficient as a pancake coil. Furthermore, as a linear coil is used it is important to align the wires parallel to a known crystallographic axis in a similar manner to the use of a linear shear wave quartz crystal. An alternative and more efficient longitudinal wave generation method was also used. Here the wire was wound directly onto the sample itself. The sample was then placed in the superconducting solenoid with the magnetic field perpendicular to the plane of the coil.

As the EMAT coils were not bonded to the sample they can be used for multiple measurements but care has to be taken not to break the fine electrical connections. The conditions of the EMATs were checked after several measurements or when the signal to noise ratio dropped below the ratio of 2:1. The most common defect was found to be the breaking of the glue holding the EMAT coil together. This was repaired by adding a thin layer of glue over the previous layer.

3.7 Sample preparations

The samples used in this work were single crystals of erbium, erbium-thulium and thulium. Two compositions of erbium-thulium alloys were used; 6.7 % and 8.4 % atomic weight of thulium. The purity of the starting materials were 99.99 by weight %. All samples were kindly supplied and prepared (grown, cut and polished) by D. Fort from the Department of Material and Metallurgy, University of Birmingham, UK. The solid-state crystal growth method used is described by D Fort (1991). For the ultrasound measurements two parallel flat surfaces were produced by spark planing.

In preparing the samples for measurement, minimal preparation was required for the EMATs measurements. The samples surfaces were cleaned with ethanol and then placed against the EMATs held between beryllium copper springs in the sample holder. For the quartz measurements the sample surfaces were first cleaned. Then the thin layer, estimated < 50 μm, of GE low-temperature varnish was applied to the surface. It was found the best acoustic coupling was made when thick GE varnish was used, i.e. almost jelly like. After the GE varnish was applied the quartz transducer was placed into position over the varnish. It was then left for 20 to 30 minutes for the GE varnish to set. Rapid cooling or warming of the sample was avoided to prevent the acoustic coupling from breaking. However, the highly magnetostrictive nature of these samples meant that extra care was taken to preserve the acoustic coupling.

References

Bozorth R.M. 1951, "Ferromagnetism", D. Van Nostrad Co. Inc., New York.

Buchel'nikov V.D and Vasil'ev A.N. 1992, Sov. Phys. Usp., **35**, no.3, pp192-211.

Dixon S.M., 1994, PhD. Thesis, University of Warwick.

Dobbs E R 1973, "Physical Acoustics", Vol. **10** (Ed: Mason W P and Thuston R N), Academic Press, London pp. 127 - 189.

Frost H M 1979, "Physical Acoustics", Vol. **14** (Ed: Mason W P and Thuston R N), Academic Press, London pp. 179 - 275.

Kawashima K. 1976, J. Acoust. Soc. Am. Vol. **60**, no.5, pp.1089-1099.

Stratton J.A. 1941, "Electromagnetic Theory", McGrow-Hill Inc., New York.

Chapter 4

Ultrasound Measurements of Single Crystal Erbium

4.0 Introduction.

Once the ultrasound measurement system was ready, experiments using miniature in-plane radially polarised shear wave EMATs were performed on the single crystal Er sample. The aims were to test the EMATs design and the feasibility of using EMATs to generate and detect ultrasound in single crystals of the rare earth metals. In contact ultrasound measurements using for example a quartz transducer, the acoustic bond between transducer and sample is important to ensure efficient coupling of the acoustic energy into the sample and the back to the detector. This is best described by the acoustic intensity transmission and reflection coefficients [Szilard, 1982];

$$T = \frac{4m}{(m + 1)^2} \tag{4.1}$$

and

$$R = \left(\frac{m - 1}{m + 1}\right)^2 \tag{4.2}$$

respectively, where m is the ratio of the acoustic impedances defined as;

$$m = \frac{\rho_2 v_2}{\rho_1 v_1} \qquad (4.3)$$

ρ and v are the density and acoustic velocity in the material respectively, defined by the subscripts, e.g. 1 : acoustic couplant and 2 : sample.

A successful application of EMATs with single crystals of rare earth metals would imply that ultrasound studies can be conducted in the non-contact regime, i.e. no acoustic bond required between transducer and sample. Er was selected because of its rather well understood magnetic properties. The magnetic structures of Er have been determined from neutron and x-ray diffraction experiments and its magnetic phase diagram (H - T phase diagram) have been constructed by McMorrow *et al.* (1992), see figure 4.1. Susceptibility data for Er from Åström *et al.* (1990) are shown in figure 4.2. However their susceptibility data were measured at much lower frequencies (maxiumum of 1 kHz) as the susceptibility is strongly frequency dependent, it is not possible to extrapolate the data to 10 MHz. Furthermore ultrasound studies have been conducted on single crystals of Er by Palmer *et al.* (1974) and Eccleston and Palmer (1992). By correlating the EMAT results with the magnetic properties of Er we should obtain a better insight into EMAT acoustic generation-detection in strongly magnetoelastic materials such as the rare earth metals.

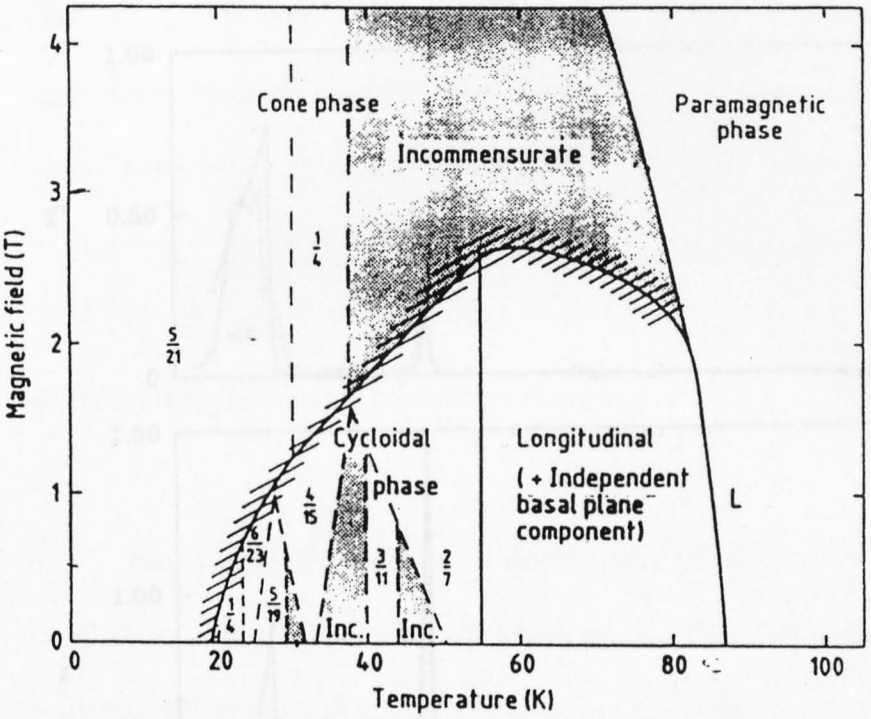

Figure 4.1. H - T phase diagram for single crystal Er reported in McMorrow *et al.* (1992). c-axis applied magnetic field. The boundaries of the main phases are shown by the solid lines, and the different commensurate and incommensurate phases are indicated by the dashed lines. Inc.= incommensurate phase. The diagonally hatched boundary separates the cone phase from the other phases and indicates a region of phase coexistance.

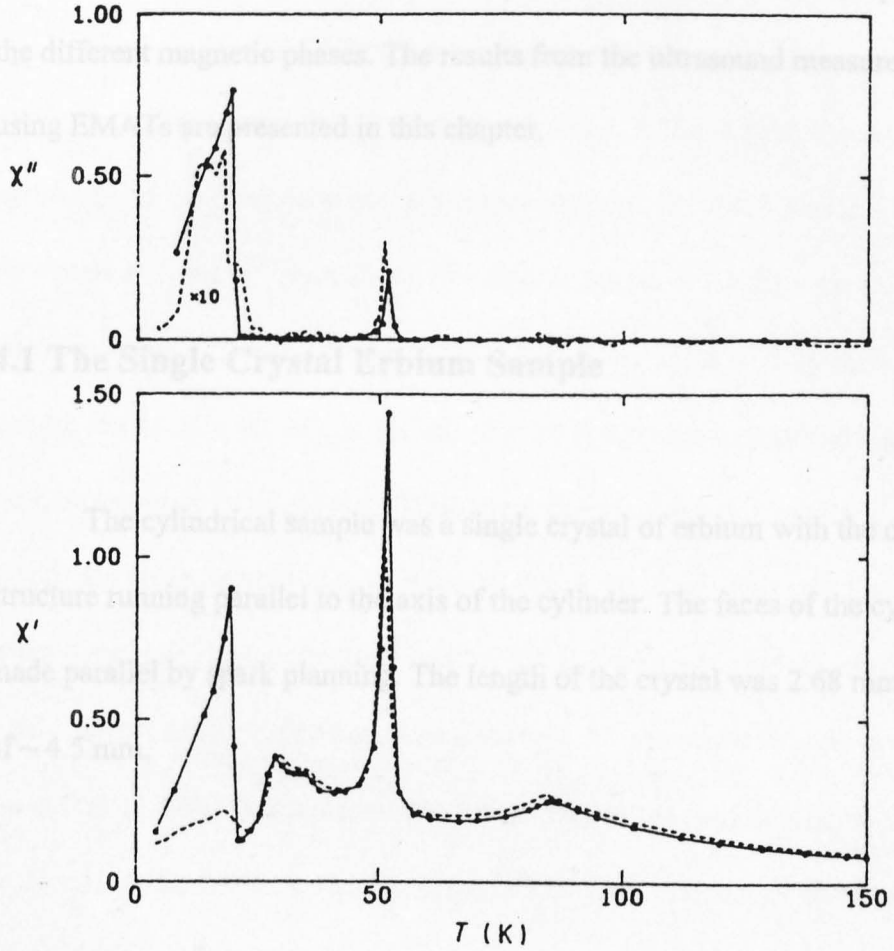

Figure 4.2. ac susceptibility at 10 Hz for Er reported in Åström *et al.* (1990). The data points for H = 8000 Am^{-1} parallel to c-axis are indicated by the dots whereas the H = 240 Am^{-1} is indicated by the dash line with x 10 scale applied. χ' and χ'' are the magnitude of the real and imaginary components of the ac susceptibility respectively.

Most ultrasound studies of the rare earth metals are conducted over a temperature range that includes the different magnetic phases. Similar use of EMATs on the Er sample should provide information on the EMAT acoustic coupling efficiency in the different magnetic phases. The results from the ultrasound measurements of erbium using EMATs are presented in this chapter.

4.1 The Single Crystal Erbium Sample

The cylindrical sample was a single crystal of erbium with the c-axis of the hcp structure running parallel to the axis of the cylinder. The faces of the cylinder were made parallel by spark planning. The length of the crystal was 2.68 mm with diameter of ~ 4.5 mm.

4.2 EMAT Acoustic Coupling Efficiency

An in-plane radially polarised shear wave EMAT was placed in contact with one of the flat surfaces of the Er sample. The crystal was orientated in the cryostat with the magnetic field directed parallel to the c-axis of the hcp structure, i.e. parallel to the axis of the cylindrical sample. The measurements were carried out while the sample was cooled at a rate of ~ 0.4 $Kmin^{-1}$. The orientation of the applied magnetic field with

respect to the EMAT spiral coil generates a radially polarised shear wave propagating down the c-axis of the sample. The send/ receive mode was used. The time of flight of the pulse echoes were measured together with the amplitude of the EMAT signal.

A plot of the EMAT acoustic coupling efficiency as a function of temperature in static applied magnetic field is shown in figure 4.3. The results show the EMAT signal amplitude of the third echo of the pulse-echo train. The 1.0 T and 2.0 T plots are displaced 10^2 and 10^4 respectively for display purpose. As the sample was cooled a slight increase in the coupling efficiency was observed at 87 K, which on further cooling almost fell back to the original level. At ~ 50 K the signal amplitude increased by at least three orders of magnitude. With the magnetic field at 0.5 and 1.0 T the signal amplitude decreases but only to increase sharply at 20 K. This trend was not observed when the applied magnetic field was set at 2.0 T where the amplitude is measured from ~ 50 K down to 26 K. The magnetic field (> 1.5 T) perturbs the magnetic structure of the sample, i.e. the incommensurate structures and the cycloid phases are removed and replaced by a conic phase (McMorrow, 1992). The existence of the incommensurate phases between 20 and 50 K seems to reduce the efficiency of the acoustic wave generation in the sample, see figure 4.1. At 20 K the signal amplitude decreased slightly and then levelled off. The elastic moduli of Er in static applied magnetic field have been reported by Eccleston and Palmer (1992) which showed step like features in C_{33} as a function of temperature. The temperatures at which the EMATs coupling efficiency increases agree well with the temperatures at the edges of these steps.

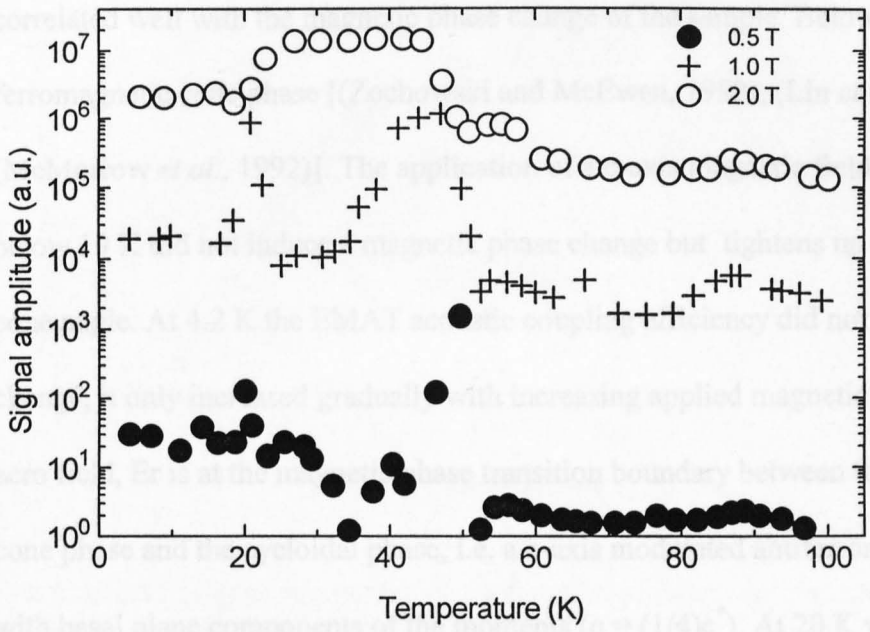

Figure 4.3. In-plane radially polarised shear wave EMAT acoustic coupling efficiency for Er as a function of temperature. Applied magnetic field parallel to the c-axis and wave propagation direction down the c-axis. The plots at 1.0 T and 2.0 T was displaced by 10^2 and 10^4 respectively for display purposes.

The EMAT performance was also monitored at fixed temperature and as a function of c-axis applied magnetic field (figure 4.4). The square root of the signal amplitude was plotted against applied magnetic field at 4.2 K, 20 K, 56 K, 79 K and 88 K. The EMAT response, i.e. the change in the acoustic coupling efficiency, correlated well with the magnetic phase change of the sample. Below 19 K Er has a ferromagnetic cone phase [(Zochowski and McEwen, 1992), (Lin *et al.*, 1992), (McMorrow *et al.*, 1992)]. The application of a c-axis magnetic field with the sample below 19 K did not induce a magnetic phase change but tightens up the ferromagnetic cone angle. At 4.2 K the EMAT acoustic coupling efficiency did not show a sudden change, it only increased gradually with increasing applied magnetic field. At 20 K and zero field, Er is at the magnetic phase transition boundary between the ferromagnetic cone phase and the cycloidal phase, i.e. a c-axis modulated antiferromagnetic structure with basal plane components of the moments ($q = (1/4)c^*$). At 20 K with the c-axis magnetic field < 0.5 T, Er is at the mixed state. This is defined by Zochowski and McEwen (1995) as a boundary separating the cone phase from the other phases. Er becomes a cone phase again when the c-axis applied magnetic field is greater than 0.9 T. At 20 K, the lowest applied field possible for the EMAT signal to be observed was at 0.1 T. A steady increase in the EMAT signal was observed with increasing applied magnetic field. The gradient of the curve (20 K) then changed at ~ 0.5 T. The next change in the EMAT signal occurred at ~ 0.8 T and it levelled off after 1.0 T. The ultrasound echo train became complicated with the interference of mode converted signals with the applied field > 1.2 T.

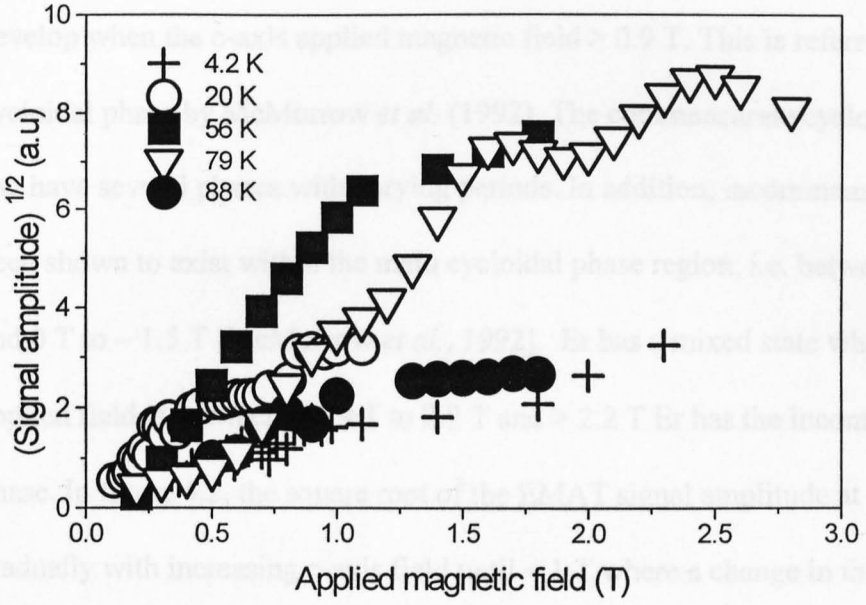

Figure 4.4. EMAT (signal amplitude)$^{1/2}$ as a function of c-axis applied magnetic field for Er. The error bar is equivalent to the marker size.

At 56 K Er can experience several magnetic phase change as the c-axis applied magnetic field is increased from zero. Between zero field and 0.9 T Er has the c-axis modulated antiferromagnetic phase. Basal plane components of the magnetic moments develop when the c-axis applied magnetic field > 0.9 T. This is referred to as the cycloidal phase by McMorrow *et al.* (1992). The commensurate cycloidal phase itself can have several phases with varying periods. In addition, incommensurate phase have been shown to exist within the main cycloidal phase region, i.e. between 20 K to 56 K and 0 T to ~ 1.5 T [McMorrow *et al.*, 1992]. Er has a mixed state when the c-axis applied field is between ~ 1.9 T to 2.2 T and > 2.2 T Er has the incommensurate cone phase. In figure 4.2, the square root of the EMAT signal amplitude at 56 K increased gradually with increasing c-axis field until ~ 1 T where a change in the gradient was observed.

At 79 K Er goes through several magnetic phase changes when a c-axis applied magnetic field is increased from zero. At zero field Er has the c-axis modulated antiferromagnetic structure and becomes a mixed state when the c-axis applied field is between ~ 2.3 T to ~ 2.5 T. Er becomes paramagnetic when the c-axis applied field > 2.5 T. The results in figure 4.2 show the EMAT signal, (signal amplitude)$^{1/2}$, increased slowly with the increase in applied field and showed a change in the gradient at ~ 0.6 T. The EMAT signal continued to rise with increasing applied magnetic field until the applied magnetic field approaches 1.6 T. Between 1.6 to 2.0 T the EMAT signal amplitude showed a slight decrease but it then increases again between 2.0 to 2.5 T and the signal peaked at 2.5 T.

At 88 K and zero applied field, Er is close to the Néel temperature, T_N = 87 K. The application of a c-axis magnetic field shifts the Néel temperature to a lower value [McMorrow *et al.*, 1992]. The EMAT signal increased steadily as the magnetic field was increased and the rate of change of the signal amplitude as a function of applied magnetic field decreases when the field approaches 1.6 T.

The EMAT results, figure 4.3 and 4.4, show:

- evidence of large change in the EMAT acoustic coupling efficiency occurring close to the magnetic phase transition of the sample.
- below 3 T the dependence of the EMAT acoustic coupling efficiency on the square of the applied magnetic field was not observed.

4.3 Velocity Measurement Using EMATs.

The elastic modulus, C_{44}, as a function of temperature is shown in figure 4.5. Since the basal plane is isotropic no birefringence effect is expected with the propagation of a radially polarised shear wave down the c-axis. The data from both quartz transducers and EMATs are shown in figure 4.5. The magnitude of the applied magnetic field was at 1.0 T and parallel to the c-axis for both the EMAT and quartz measurements. There was a large discrepancy between them below 50 K. This shows the automatic ultrasound measurement system requires well defined pulse shapes. Note

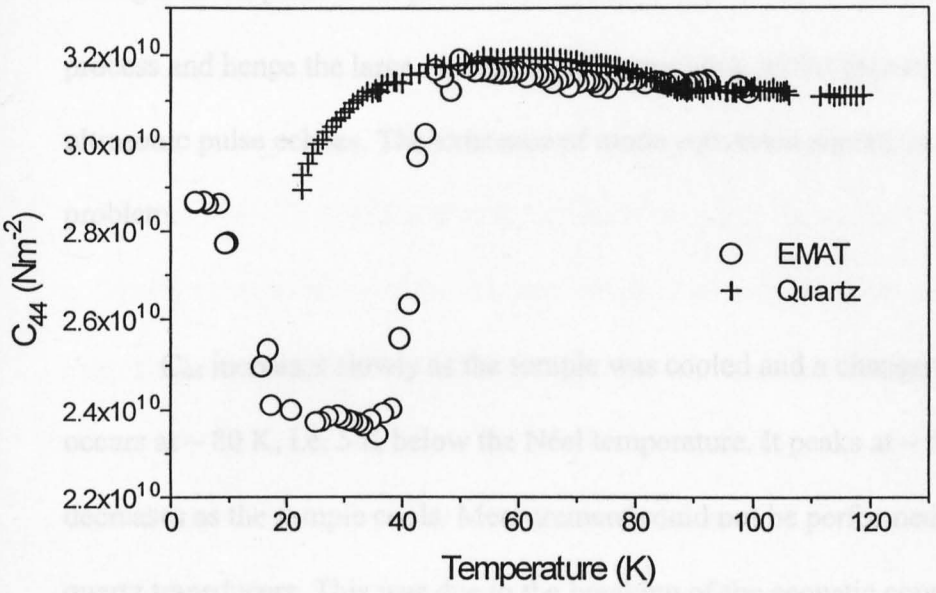

Figure 4.5. C_{44} versus temperature for Er. Wave propagation down the c-axis and applied magnetic field, 1.0 T, parallel to c-axis for both the EMAT and quartz measurements.

that the automated system can be used to drive both quartz transducers and EMATs. Changes in the pulse-echo profile leads to loss of accuracy in the pulse super-position process and hence the large error in the determination of the time of flight of the ultrasonic pulse echoes. The existence of mode converted signals is an inherent problem.

C_{44} increases slowly as the sample was cooled and a change in the gradient occurs at ~ 80 K, i.e. 5 K below the Néel temperature. It peaks at ~ 54 K and from then decreases as the sample cools. Measurement could not be performed below 22 K using quartz transducers. This was due to the breaking of the acoustic couplant as a result of the abrupt change in the dimension of the sample, as indicated in the $\Delta l/l$ measurement reported by Zochowski and McEwen (1995).

4.4 Discussion and Conclusion

This preliminary work showed large changes (at least 10 times) close to the known first order magnetic transition temperatures of Er. The changes in the EMAT signal were gradual, i.e. the EMAT signal amplitude remained high over a temperature range of 10 - 15 K approximately centred at the transition temperatures. The zero static applied magnetic field, $H_o = 0$, generation of ultrasound was not observed. Even if there is a zero field acoustic generation mechanism the present system is not sensitive enough to detect it. There was a variation in minimum magnitude of H_o required for ultrasound signal to be observed. In the ferromagnetic state the minimum static applied field

required was $H_0 \sim 0.1$ T and H_0 had to be increased to ~ 0.25 T in the anti-ferromagnetic phase and $H_0 > 0.5$ T when the sample was paramagnetic. Some correlation between H_0 and the EMATs acoustic coupling efficiency was observed where an increase in the EMATs acoustic coupling efficiency was observed with increasing field. The EMAT signal amplitude versus H_0 data, for $0.1 \text{ T} < H_0 < 2.8$ T, did not resolve the Lorentz generation mechanism from those contributed by the magnetoelastic effects. When $H_0 > 3$ T the acoustic generation became highly efficiency as shown by the enhancement of the mode converted acoustic signals in the ultrasonic wave-forms. While the mode converted signals caused problems, both in the signal amplitude measurements and time-of -flight measurements, as both longitudinal and shear wave are propagating simultaneously there is the potential with more sophisticated data analysis to extract the required data from the ultrasonic wave-forms.

In this system, the ultrasound measurements require a well defined reference pulse. As explained in chapter 3, data points from two successive pulses in the wave train are used by the auto-correlation algorithm to determine the time of flight of the pulse echoes. Two gates are set over these pulse echoes. The introduction of large errors in the time of flight measurements can be attributed to (a) a large variation in the pulse profile between the two selected pulse echoes and (b) a sudden change in velocity, i.e. $\Delta t >$ 1/frequency of the tone-burst. A combination of these problems are reflected in the results shown in figure 4.5. These initial runs show that care must be taken in this automatic measurement system to ensure that the pulse echoes can be correctly traced. A reasonable signal to noise ratio (> 3:1) is required for reliable time of flight of the pulse echoes to be extracted. An immediate solution is to increase the signal by increasing the

driving voltage of the transducers and also increasing the number of cycles in the tone burst. For this system the peak to peak driving voltage is limited to 200 V. The number of cycles per pulse echo can be changed and is software controlled. However, driving the transducers very hard is not desirable. A transducer driven hard rings much longer than preferred. This is characterised by a broad asymmetric pulse. The tail end of the pulse can run into the successive pulse echo. This reduces the time resolution of the pulse echoes. A balance between increasing signal amplitude and the number of cycles to use is required. Driving the transducer off resonance can also reduce the ringing. Mechanical backing was used in this work to reduce transducer ringing. The backing consisted of vacuum grease placed at the back of the transducer and also on the back wall of the sample. The use of backing material was only applied to ultrasound measurements where quartz transducers were used. Despite the effort in obtaining good signal to noise ratio the use of a wide-band pre-amplifier (centred at 10 MHz producing 50 dB of gain) was necessary.

In general, commercial ultrasound measurement systems are mostly geared to drive PZT transducers which are orders of magnitude more efficient than quartz transducers or EMATs. Inefficiency in the acoustic generation is not solely dependent on the type of transducer used but the conditions in which the transducers are used. How well the transducers are tuned determines the efficiency in the transfer of electrical energy into mechanical energy (acoustic). The present practice is to ensure that the transducers and drivers are electrically matched (ideally at 50 Ω) at 77 K. The capacitor or inductor, depending if quartz or EMAT is used, is selected for that one temperature only. The temperature range in which the experiments were performed did not help the

tuning process since the circuit would be detuned due to the temperature dependence of the electrical parameters. In most cases the ultrasound studies are performed from 4.2 K to 200 K. The system would benefit from the use of tuneable capacitor and inductor. The tuning circuit had to be wired close to the transducer. A tuning circuit like the ones used in NMR systems could be adapted for use in this ultrasound measurement system. The design of a variable tuning circuit would have to take into consideration the restricted sample space.

References

Andrianov A.V., Buchel'nikov V.D., Vasil'ev A.N., Gaidukov Yu.P., Il'yasov R.S. and Shavrov V.G., 1988, Sov. Phys. JETP **67**(11), pp2331.

Andrianov A.V., Buchel'nikov V.D., Vasil'ev A.N., Gaidukov Yu.P., Shavrov V.G., 1990, Sov. Phys. JETP **70**(5), pp 944.

Åström H U, Chen D-X, Benediktsson G and Rao K V, 1990, J. Condens. Matter **2**, pp3349-3357.

Bar'yakhtar V.G. and Turov E.A., 1988, Ed: Borovik-Ramanov A.S. and Sinha S.K., "Spin Waves And Magnetic Excitations", chpt 7, North-Holland, Amsterdam.

Buchel'nikov V.D and Vasil'ev A.N., 1992, Sov. Phys. Usp., **35**, no.3, pp192-211.

Buchel'nikov V.D. and Shavrov V.G., 1991, Sov. Phys. Solid State, **33**(11), pp1853.

Eccleston R.S. and S.B. Palmer 1992, J. Magnetism and Magnetic Materials, **104-107**, pp.1529-1530.

Lin H., Collins M.F., Holden T.M. and Wei W., 1992, Phys. Rev. B, **45**, pp12873.

McMorrow D.F., Jehan D.A., Cowley R.A., Eccleston R.S and McIntyre G.J. 1992, J Phys.: Condens. Matter, **4**, pp.8599-8608.

Palmer S.B., E.W. Lee and M.N. Islam 1974, Proc. Roy. Soc. Ser. **A338**, pp341.

Povey M.J.W., Meredith D.J. and Dobbs E.R., 1980, J.Phys. F: Metal Phys., **10**, pp2041.

Watson B. and Ali N., 1995, J.Phys.: Condens. Matter, **7**, pp4713.

Zochowski S.W. and McEwan K.A 1995, J. Magnetism and Magnetic Materls, **104-107**, pp.1127-1128.

Chapter 5

Ultrasound Measurements Of Single Crystal Tm.

5.0 Introduction.

The study of the magnetic properties and magnetic structures of Tm have been reported by Koehler *et al.* (1962), Bohr *et al.* (1990), Åström *et al.* (1991) and Steigenberger *et al.* (1992) and are described in section 2.3. Figure 5.1 shows a tentative magnetic phase diagram of Tm deduce by Zochowski and McEwen (1992) from thermal expansion and magnetostriction data. Magnetisation and ac susceptibility data reported by Åström *et al.* (1991) are shown in figures 5.2 and 5.3 respectively. However at the time the present work was conducted there were no reports of measurements of the elastic constants of Tm. The present chapter describes ultrasonic measurements of the temperature dependence of the single crystal elastic constants of Tm. Ultrasonic velocity measurements were made, with and without applied magnetic field and as a function of temperature. Measurements were carried out with conventional quartz transducers and EMATs. The elastic moduli were calculated from the velocity measurements. In chapter 4 was shown that EMATs could be used successfully on single crystal Er and therefore its application has been extended to single crystal Tm. The EMAT signal amplitude is used to construct a tentative magnetic phase diagram for the single crystal Tm sample and this is compared to results obtained with complementary techniques.

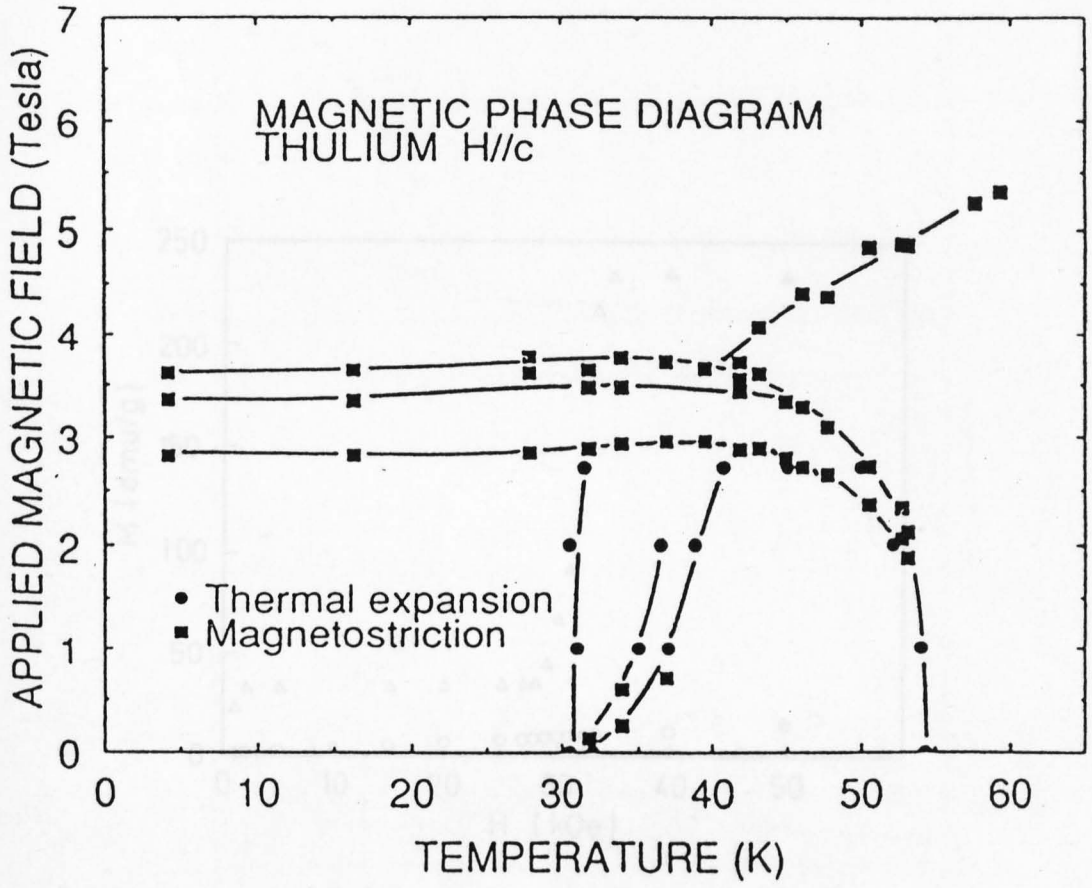

Figure 5.1. A tentative magnetic phase diagram of Tm deduce by Zochowski and McEwen (1992). Square and round markers indicate anomalies observed in their magnetostriction and thermal expansion data respectively.

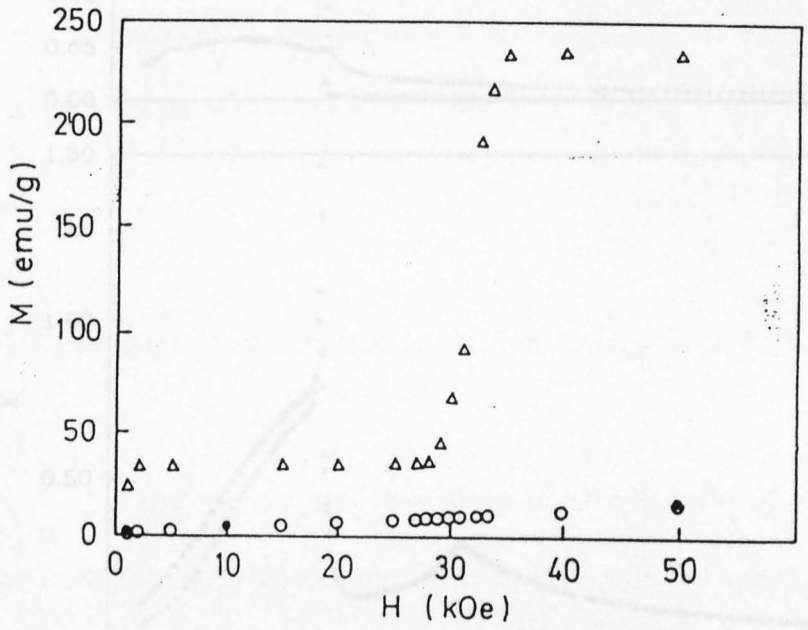

Figure 5.2. Magnetic moment of Tm at 5 K measured with a SQUID magnetometer reported by Åström *et al.* (1991). White and dark circles represent a-axis and b-axis measurements respectively. The c-axis measurements are indicated by the triangles.

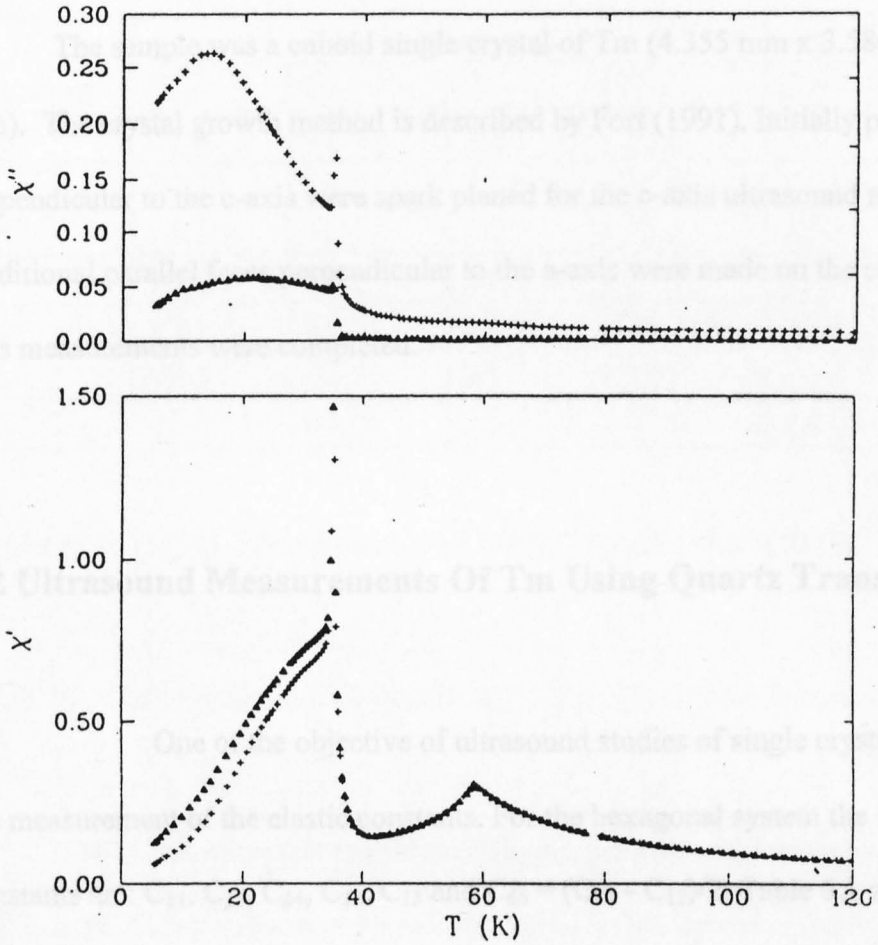

Figure 5.3. ac susceptibility versus temperature for Tm with 0.1 Oe c-axis applied magnetic field. The dark triangles and + symbols represent 100 Hz and 1000 Hz respectively. Data from Åström *et.al.* (1991).

5.1 The Single Crystal Tm Sample

The sample was a cuboid single crystal of Tm (4.355 mm x 3.586 mm x 3.772 mm). The crystal growth method is described by Fort (1991). Initially parallel faces perpendicular to the c-axis were spark planed for the c-axis ultrasound measurements. Additional parallel faces perpendicular to the a-axis were made on the crystal after the c-axis measurements were completed.

5.2 Ultrasound Measurements Of Tm Using Quartz Transducers

One of the objective of ultrasound studies of single crystal rare earth is the measurement of the elastic constants. For the hexagonal system the five elastic constants are: C_{11}, C_{33}, C_{44}, C_{12}, C_{13} and $C_{66} = (C_{11} - C_{12})/2$. Table 5.1 shows a list of the elastic constants for the heavy rare earth with the hexagonal crystal system at room temperature and zero applied field. The measurements for C_{13} could not be performed on the existing single crystal Tm sample, restricted by the physical size of the sample. To perform the C_{13} measurement additional parallel flat surfaces had to be spark planned on the sample. This is to enable ultrasonic waves to be propagated along the 45° direction to the c-axis in the a - c plane. To extract C_{13} from equations 2.6 and 2.7 two sets of velocities measurements had to made, i.e. the b-axis polarised shear wave

velocity, defined by eq. 2.6, and the velocity from the propagation of a longitudinal wave defined by eq. 2.7. The error estimated for the Tm data is ± 0.5 GPa.

Elements	Elastic Moduli (GPa) at 300 K and 0 T					
	C_{11}	C_{33}	C_{44}	C_{12}	C_{13}	C_{66}
Gd *	67.8	71.2	20.8	25.6	20.7	21.1
Tb *	69.2	74.4	21.8	25.0	21.8	22.1
Dy +	73.1	78.1	24.0	25.3	22.3	23.9
Ho +	76.1	78.6	24.2	24.7	20.6	25.7
Er *	83.7	84.5	27.5	29.3	22.3	27.1
Tm	92.5	81.5	28.2	33.5		29.5
Lu #	91.0	84.0	26.8	32.0	28.0	29.5

Palmer *et al.* (1974), + Palmer and Lee (1972), # Tonnies *et al.* (1971)

Table 5.1. Elastic moduli of heavy rare earth elements at room temperature and pressure.

The elastic constants enable the velocity, slowness and wave surfaces to be constructed. These surfaces provide information on the behaviour of the ultrasonic waves as a function of propagation direction. The slowness (polar plot of 1/velocity) surfaces for Tm have been constructed with different C_{13} and based on the equations given in Musgrave (1970), figure 5.4. From table 5.1 it can be deduce that the elastic constants increase with atomic number and the estimated (extrapolated) value for Tm C_{13} is ~ 25 GPa . In figure 5.4, the c-axis direction was selected as the 0° starting point for the polar plot and with the a-axis direction at 90°. The slowness surfaces are; longitudinal, L (dash) , the in-plane (a-c plane) polarised shear, S_1 (solid), and the b-axis polarised shear, S_2 (dots). The units are in $m^{-1}s$. The slowness surface for the b-axis

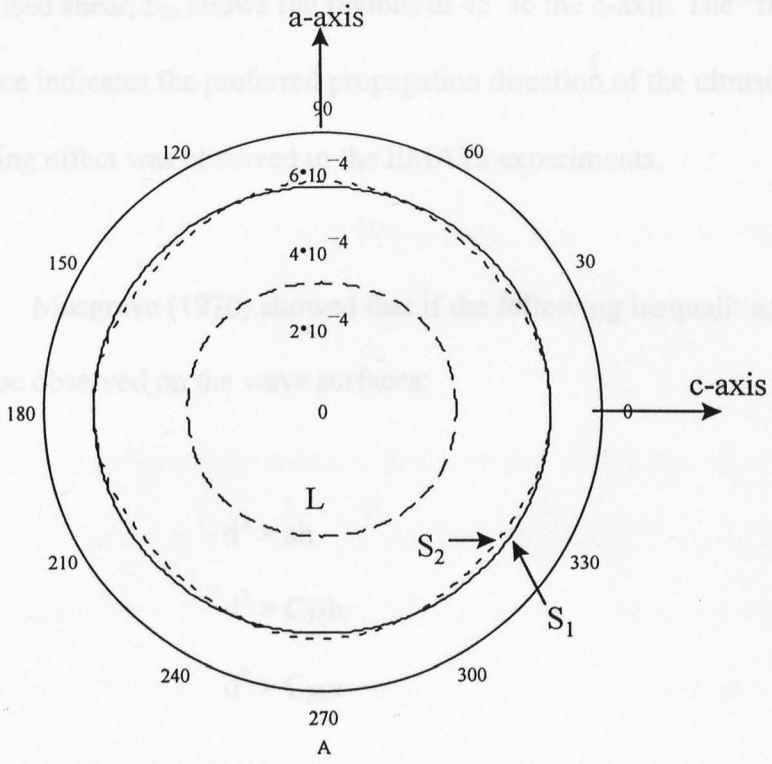

Figure 5.4. Slowness surfaces for Tm in the a-c plane in units of $m^{-1}s$. C_{13} = 25 GPa. L = longitudinal wave, S_1 = a-c plane polarised shear and S_2 = b-axis polarised shear.

polarised shear, S_2, shows flat regions at 45° to the c-axis. The "flats" on the slowness surface indicates the preferred propagation direction of the ultrasonic waves. The beam steering effect was observed in the EMATs experiments.

Musgrave (1970) showed that if the following inequalities are satisfied cusping will be observed on the wave surfaces:

$$d^2 > ah \quad (5.1)$$

$$d^2 > C_{11}h \quad (5.2)$$

$$d^2 > C_{33}a \quad (5.3)$$

where

$$d = C_{13} + C_{44} \quad (5.4)$$

$$a = C_{11} - C_{44} \quad (5.5)$$

$$h = C_{33} - C_{44} \quad (5.6)$$

For Tm with C_{13} = 25 GPa the above inequalities are not satisfied. $d^2 = 2.8 \times 10^{21}$ Pa^2, $ah = 3.4 \times 10^{21}$ Pa^2, $C_{11}h = 4.9 \times 10^{21}$ and $C_{33}a = 5.2 \times 10^{21}$. The experimental consequence of cusping edges on the wave surfaces is the inaccuracy in the velocity measurements.

Figure 5.5 shows the temperature dependence of C_{33} at 0 T. The sample was initially cooled and then warmed (at 0.5 K/min.). Only a slight hysteresis was observed

between 50 K and 80 K. The longitudinal velocity increased steadily as the sample was cooled from 200 K to 140 K. It then levelled off between 110 K and 140 K. The velocity decreases below 110 K and again levels off at ~ 55 K (T_N = 56 K reported by Koehler *et al.*, (1962) and McEwen *et al.* (1995)), a significant change in the behaviour was observed with the velocity rising rapidly with decreasing temperature.

The only obvious anomaly in C_{33} at zero field from the raw data was T_N ~ 55 K, figures 5.5. and 5.6. The derivative of the data (dC_{33}/dT) was not sufficient to enhance other anomalies in the data, figure 5.7. The noise in the data were also differentiated and were further enhanced. A combination of differentiation and smoothing processes removed not only the noise but also smooth out the signal hence removing the detail of the elastic constant data. However, other anomalies in C_{33} were observed after the data were signal processed using the technique reported by Greenough (1978). The technique is as follows, two least square fits are made to points on either side of a point, say on x_i. The number of points selected (n) for the least square fit depends on the data density and the resolution required. The intercept of the least square fit lines is then determined and the area of the triangle formed by the three points, i.e. the intercept, x_{i-n} and x_{i+n}, is then calculated. The area would vary depending on the smoothness of the data and also the value of n. These steps are then repeated over the range of the data, i.e. i is incremented. This signal processing technique was applied to the zero field C_{33} data. The calculated areas were then divided by $\Delta x = x_{i-n} - x_{i+n}$ and each point (area) is averaged over three nearest neighbours, figure 5.8. The following anomalies in the zero field C_{33} data (cooling) were observed: 26 K, 38 K, 55 K, 68 K, 78 K and 92 K. Although only one of the six anomalies in C_{33} can be directly associated with the magnetic transition of the

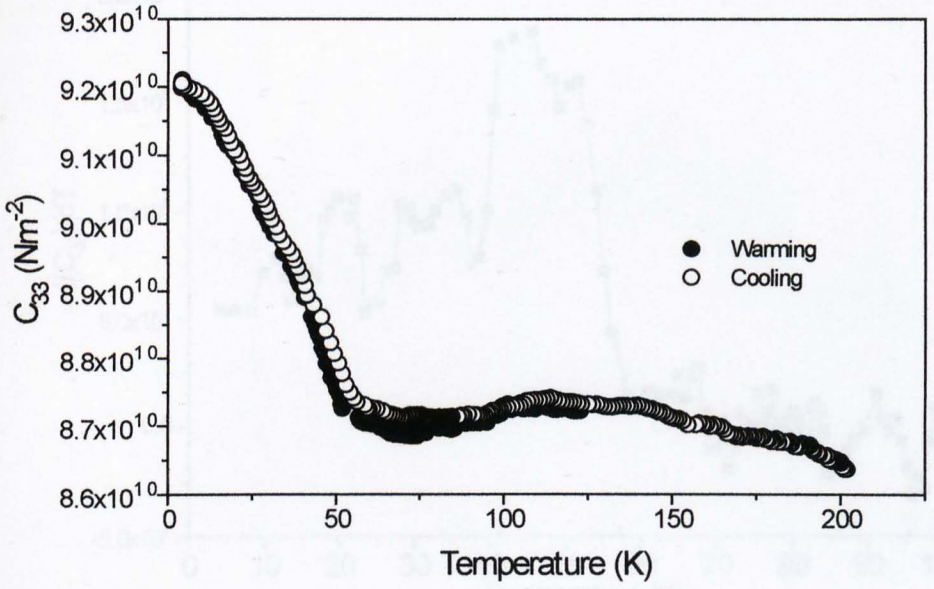

Figure 5.5. C_{33} as a function of temperature at zero applied magnetic field.

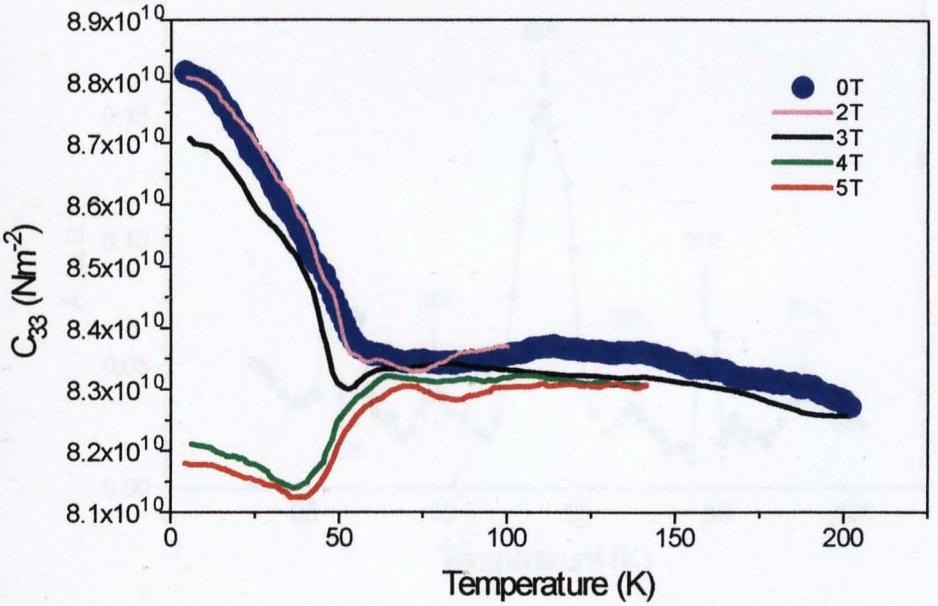

Figure 5.6. C_{33} as a function of temperature with applied magnetic field along the c-axis.

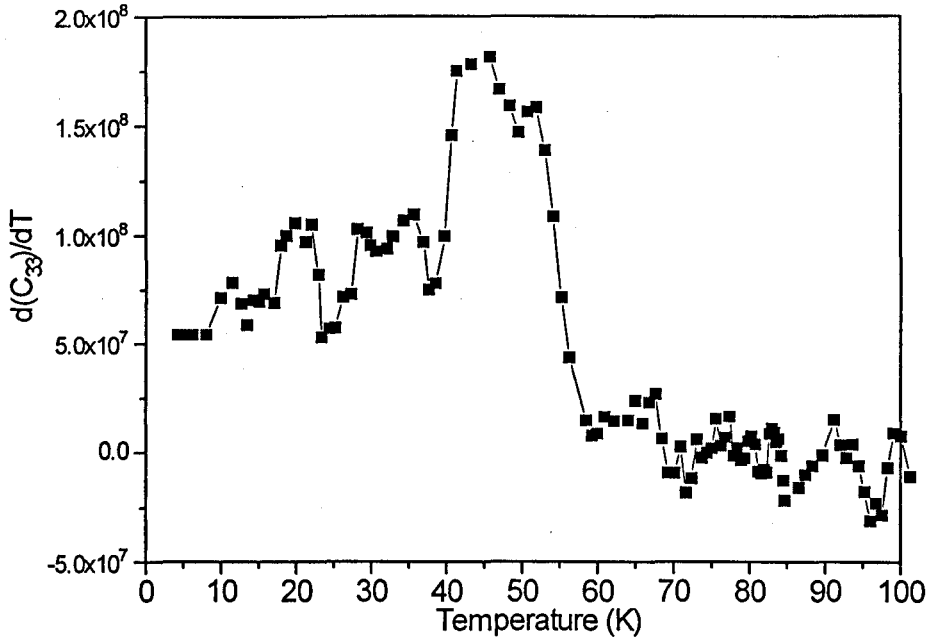

Figure 5.7. First order derivative of C_{33} (zero field) with respect to temperature as a function of temperature.

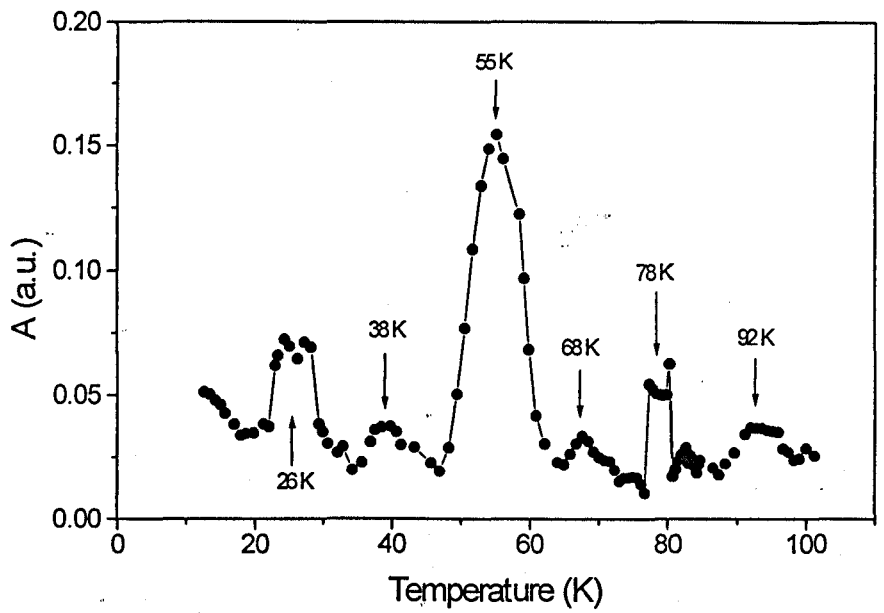

Figure 5.8. Signal processed C_{33} (zero field) data using technique described in Greenough (1978) and a 3 point nearest neighbour averaging applied.

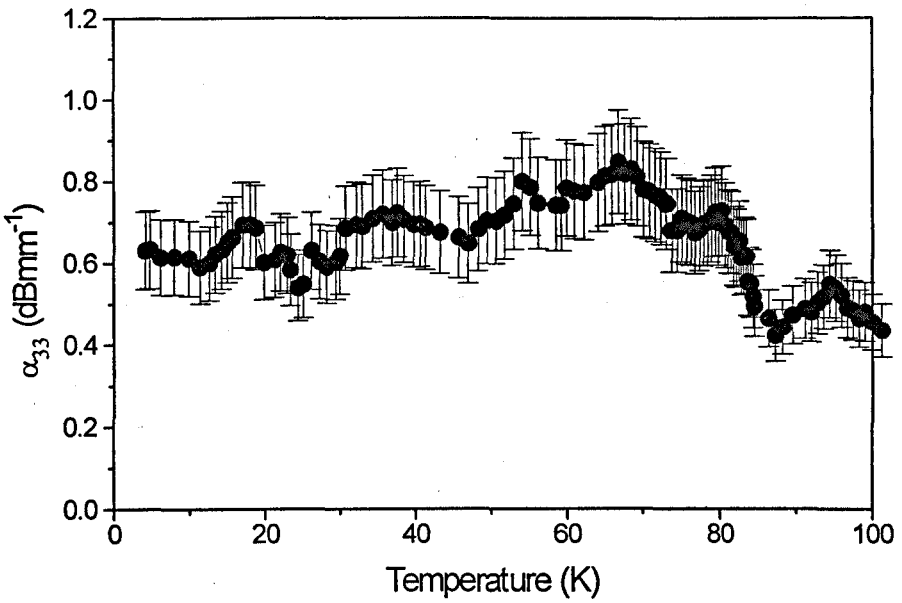

Figure 5.9. Ultrasonic attenuation of longitudinal wave propagatinf down the c-axis as a function of temperature at zero applied field.

sample, i.e. $T_N = 55$ K. Although $T_C = 32$ K (Koehler *et al.*, 1962) and the squaring up of the c-axis modulated antiferromagnetic structure ,42 K, (Koehler *et al.*, 1962) it may be possible that the anomalies at 26 K and 38 K could be associated with these magnetic transitions. The ultrasonic attenuation, figure 5.9, only showed an anomaly at ~ 88 K, i.e. 0.3 $dBmm^{-1}$ increase in ultrasonic longitudinal wave attenuation. It is an inherent problem with the present system to have large absolute errors (~ 15 %) in the attenuation measurements.

The experiment was repeated with an applied magnetic field set parallel to the c-axis. C_{33} did not show significant changes with the applied magnetic field magnitude < 3.0 T when compared to the zero field data. At 3.0 T, C_{33} shows a minimum at 52 K before it started increasing following a similar trend to the zero field curve. The material softens further when the applied magnetic field was increased with most significant effects below 50 K. At 4 T, C_{33} shows a minimum at 37 K with $C_{33} = 81.4$ GPa. This minimum was reduced further when the applied magnetic field was increased to 5 T. At 5.0 T, C_{33} showed similar features except for the slight dip at ~ 78 K.

Figures 5.10 shows C_{44} as a function of temperature and in zero applied field. The sample was cooled from 243 K down to 4.2 K. As the sample was cooled, C_{44} increases gradually and has a maximum value at 140 K. C_{44} then decreases to a minimum at $T_N = 59$ K. Below T_N C_{44} increases rapidly. The signal processing technique described above was applied to the zero field C_{44} data where it showed an anomaly at 33 K in addition to T_N, figure 5.11. Although the attenuation measurements

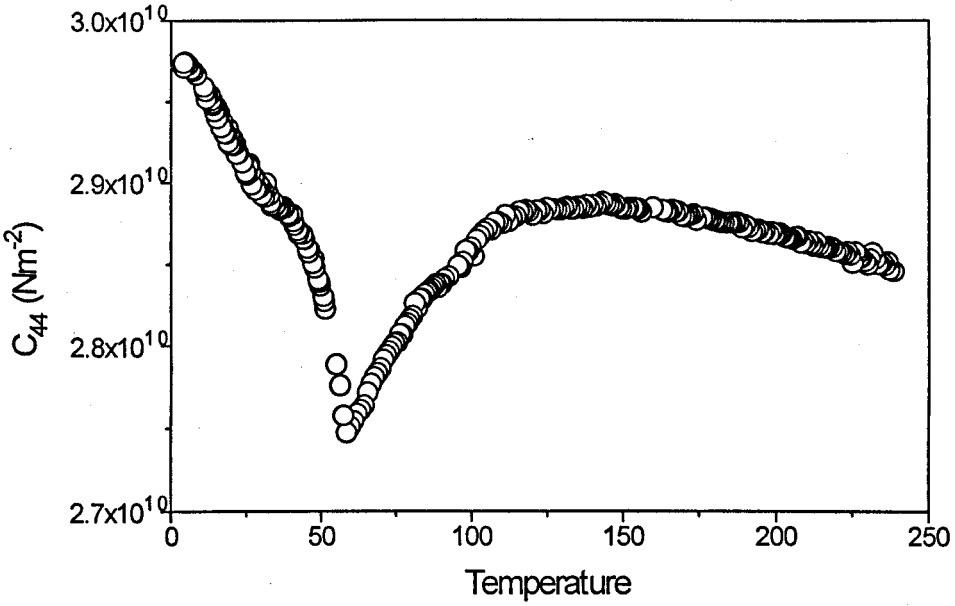

Figure 5.10. C_{44} as a function of temperature at zero applied field.

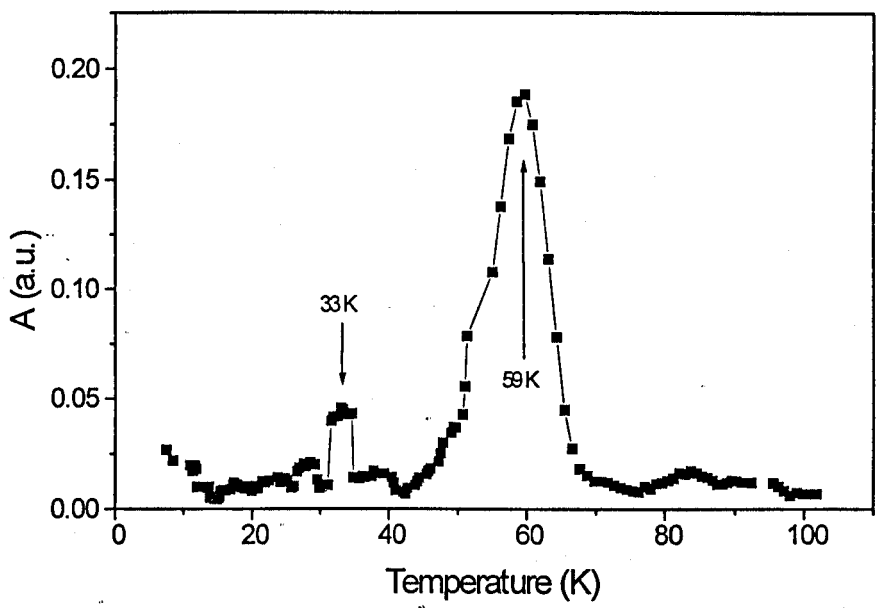

Figure 5.11. Signal processed zero field C_{44} data as a function of temperature.

(α_{44}), figure 5.12, did not show significant changes close to T_N the shear wave attenuation increases from ~ 1 $dBmm^{-1}$ to ~ 3 $dBmm^{-1}$ at 28 K.

Figure 5.13 shows the same experiment conducted with an applied magnetic field along the wave propagation direction (c-axis). The anomalies observed at 0 T were also present with the application of a magnetic field. As the applied magnetic field was increased the material became softer in the region of the magnetic ordering temperature as indicated by the increasingly pronounced dip close to 55 K. In addition to the decrease in C_{44} the minimum shifted to lower temperature. With an applied magnetic field < 2.0 T this minimum was observed at 55 K and was shifted to 50 K at 3.0 T. The data acquisition was terminated at 26 K when the applied magnetic field along the c-axis was at 3.0 T because of high attenuation of the ultrasound, figure 5.14.

They were difficulties with ultrasonic propagation in the basal plane since the quartz transducer became highly resonant at 67 K and 90 K for the C_{66} and C_{11} measurements respectively. This prevented velocity measurements at lower temperatures. There were no difficulties encounted for the basal plane C_{44} measurements. Figure 5.15 show C_{66} as function of temperature. The data were acquired while the sample was cooled. In the temperature range of 90 K to 293 K, the change in C_{66} was gradual. This trend was also observed for C_{11} between 67 K and 210 K and with the exception of the anomaly at 101 K, figure 5.16.

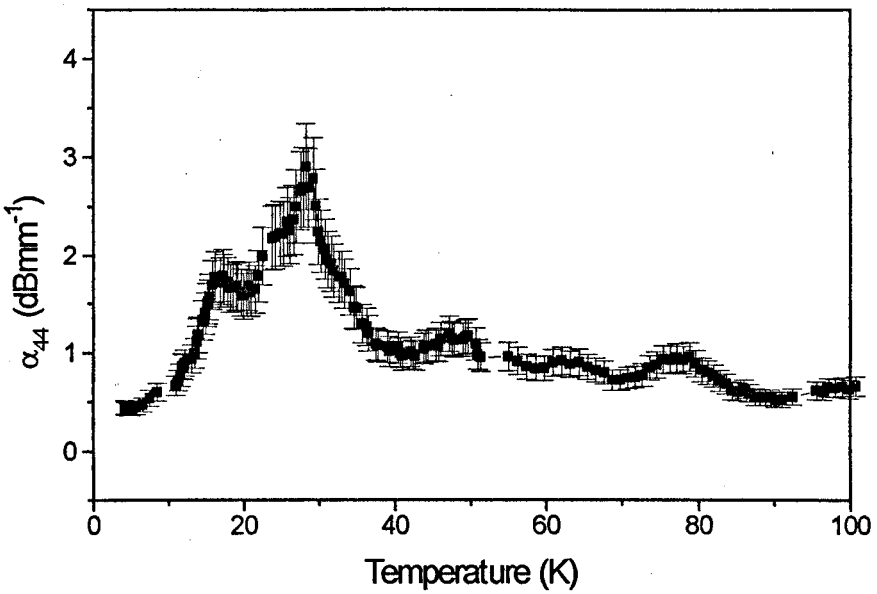

Figure 5.12. Zero field shear wave attenuation (α_{44}) versus temperature. Wave propagating direction down the c-axis.

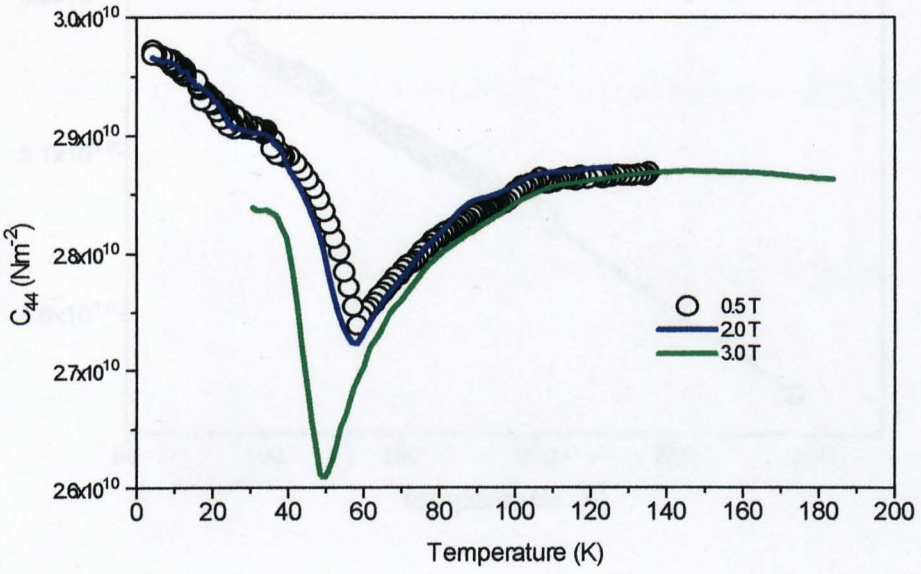

Figure 5.13. C_{44} as a function of temperature with applied magnetic field along the c-axis.

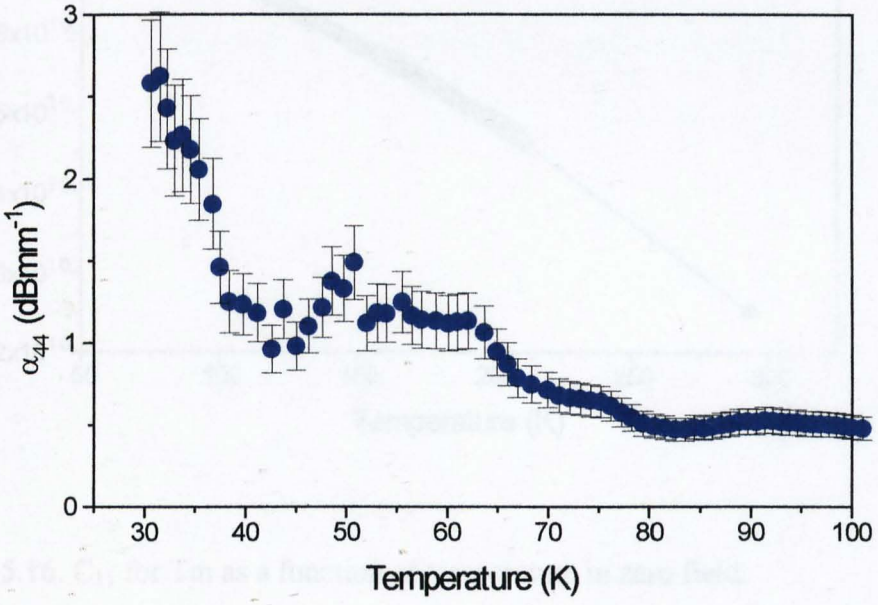

Figure 5.14. α_{44} as a function of temperature. Applied magnetic field at 3 T along the c-axis.

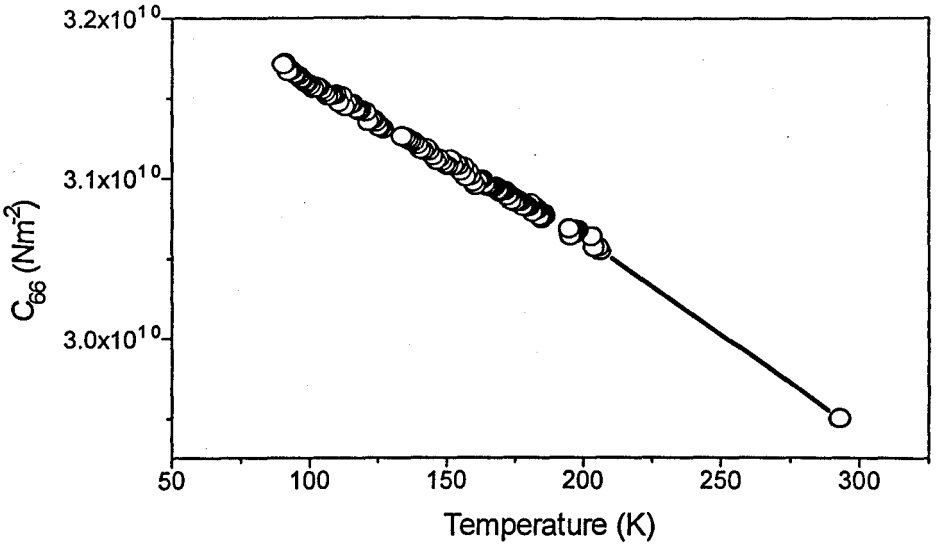

Figure 5.15. C_{66} for Tm as a function of temperature in zero field.

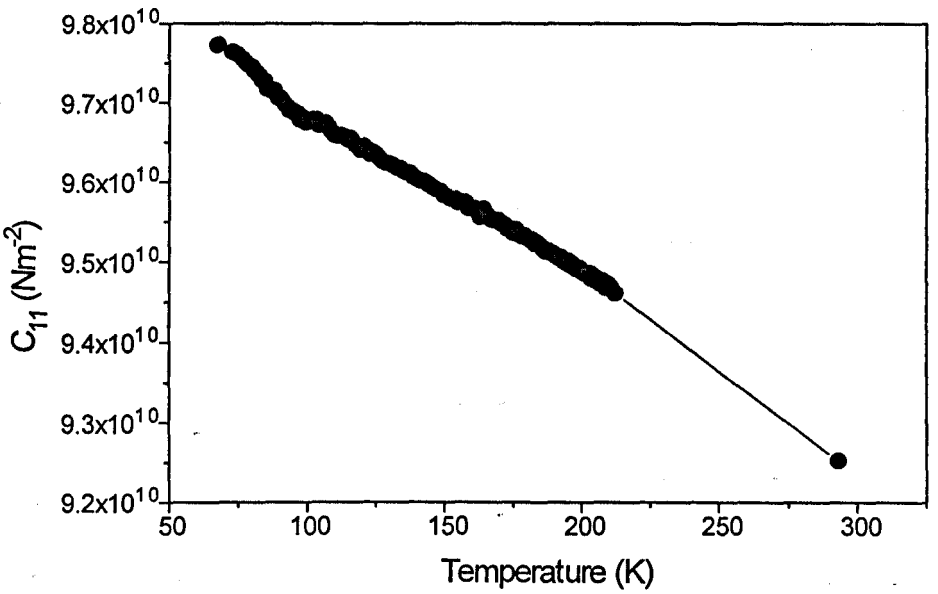

Figure 5.16. C_{11} for Tm as a function of temperature in zero field.

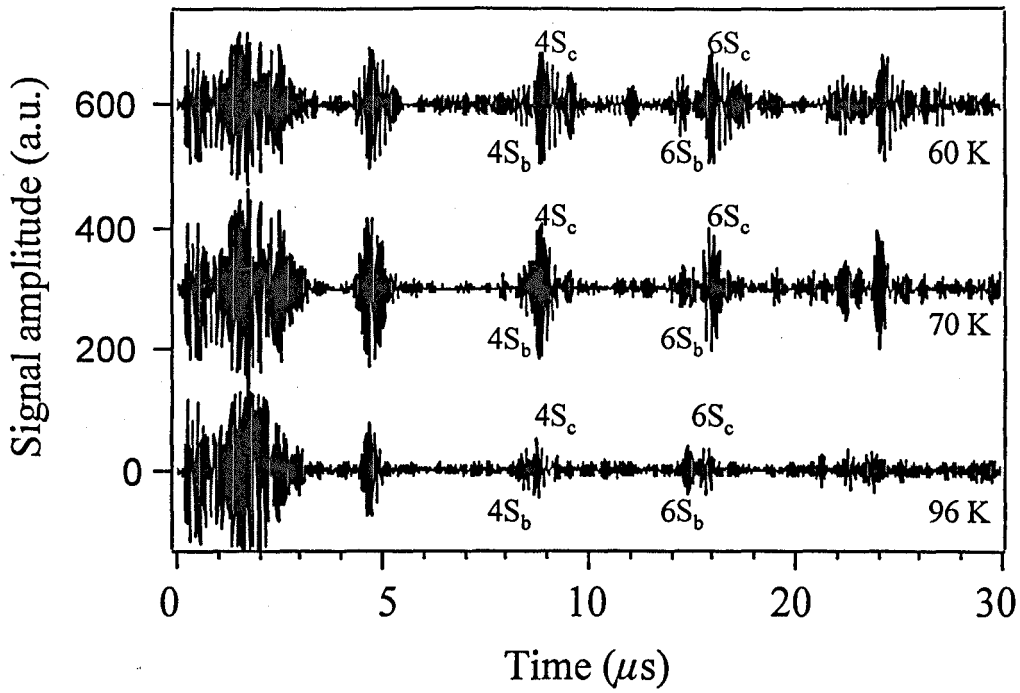

Figure 5.17. Wave-form of EMAT generated in-plane radially polarised shear wave. Wave propagation down the a-axis with applied magnetic field parallel to a-axis. Shear wave with polarisation along the b-axis and c-axis are denoted by S_b and S_c respectively.

5.3 Ultrasound Measurements Of Tm Using In-Plane Radially Polarised EMAT

The EMATs were used to carry out measurements of the velocity of in-plane radially polarised shear waves propagating down the c-axis and the a-axis. Shear wave velocity measurements made with wave propagation down the c-axis allowed the determination of C_{44}. In contrast the propagation of the radially polarised shear wave down the a-axis revealed the anisotropy in this direction. The ultrasound energy is steered into the principal axes and this produces birefringence as shown in figure 5.17. With a-axis magnetic field set at 2.0 T (figure 5.18), two sets of shear wave echoes are observed, labelled as S_b and S_c with their polarisation direction along the b-axis and c-axis respectively. The velocities of the two shear waves were known from the quartz measurements and hence can be identified. This automated ultrasound measurement system requires well defined echoes. Therefore, in order for the S_b and S_c velocities to be measured accurately the pulses have to be well separated. The two sets of shear wave pulse echoes are well separated further along in time but with reduced amplitude. When the ultrasound became highly attenuating the signal amplitude of these latter pulse echoes reduces to the noise level. Therefore the C_{66} measurements as a function of temperature and applied magnetic field were not carried out due to the large error introduced. However, the comparison of the signal amplitude between S_b and S_c pulse echoes shows ultrasound energy is steered more into the c-axis polarised shear wave. There was a significant reduction in the S_b signal amplitude at 70 K, i.e. close to the temperature where difficulties in the ultrasound measurements with quartz transducers

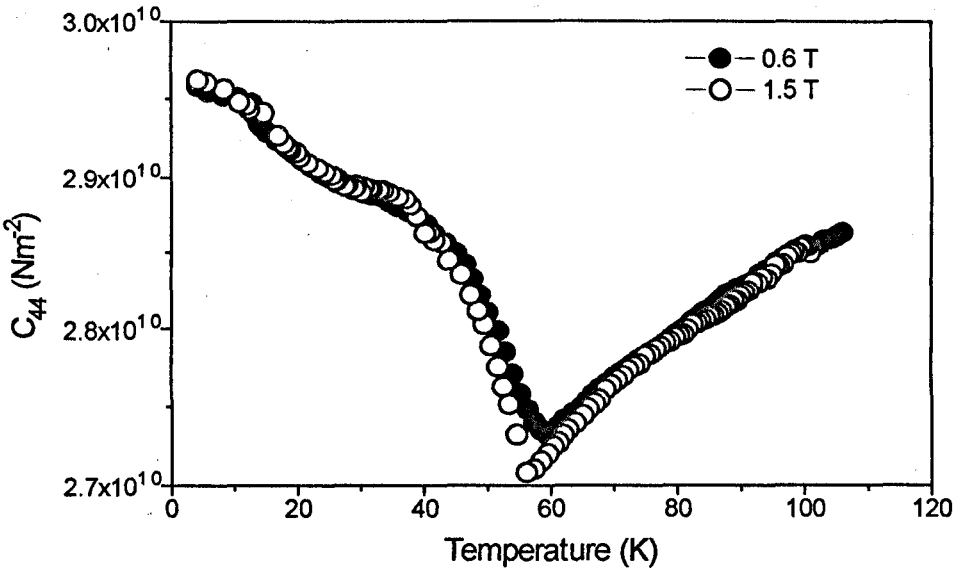

Figure 5.18. EMAT measured C_{44} as a function of temperature and applied magnetic field directed parallel to the c-axis.

were observed. This further proves the b-axis polarised shear wave experiences high ultrasonic attenuation when propagated down the a-axis of the single crystal Tm. In cooling the sample the amplitude of S_c increases whereas the amplitude of S_b shows only a marginal change. The observed signal amplitude is a combination of the EMAT acoustic generation efficiency and the ultrasonic attenuation.

The c-axis propagated shear velocity measurements using the in-plane radially polarised shear wave EMAT are very similar to those obtained with the y-cut quartz transducers. Figure 5.18 shows C_{44} as function of temperature measured with the EMAT at magnetic fields of 0.6 T and 1.5 T.

5.4 Contour Plot of EMAT Signal Amplitude

The EMAT acoustic coupling efficiency changes with temperature and applied magnetic field. An increase in the EMAT acoustic coupling efficiency was observed close to the magnetic phase transition temperatures. Similar to the effects observed with the EMAT measurements conducted on single crystal of Er (Chapter 4). A typical EMAT signal amplitude as a function of temperature sweep at constant applied magnetic field is shown in figure 5.19. The direction of shear wave propagation and applied magnetic field, $H_o = 1.0$ T, is down the c-axis. The EMAT signal amplitude as a function of temperature measurements were repeated at different static applied magnetic fields, i.e. H_o increments of 0.1 T and temperature increments of ~ 0.5 K. The data were use to plot the EMAT signal amplitude as function of H_o and T. The H_o - T EMAT

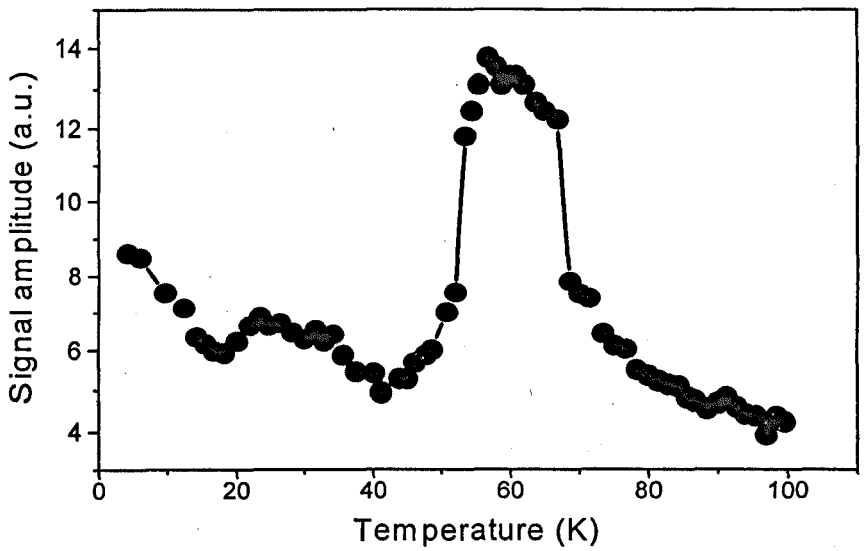

Figure 5.19. EMAT signal amplitude as a function of temperature. In-plane radially polarised shear wave propagates down the c-axis and applied magnetic field, 1.0 T, set parallel to the c-axis.

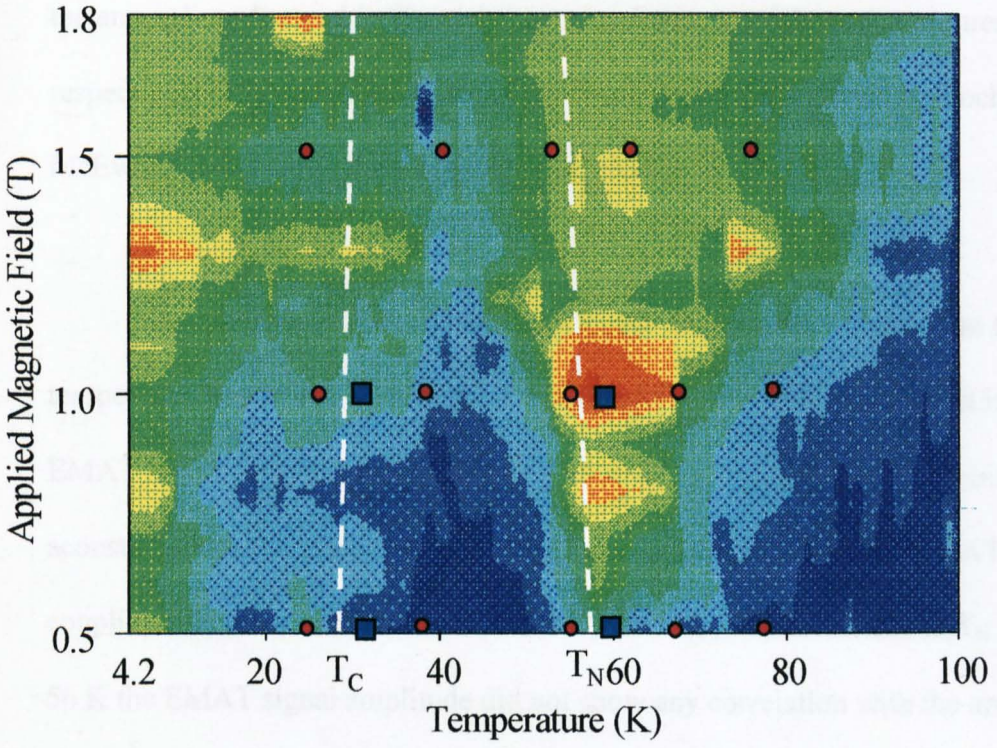

Figure 5.20. H_o - T plot of EMAT signal amplitude. H_o and shear wave propagation along the c-axis of the single crystal Tm. The plot is generated with 0.1 T increment of H_o and ~ 0.5 K increment of T. The EMAT signal amplitude is divided into ten levels with red (10 a.u.) indicating high signal level whereas the blue regions indicate low EMAT signal amplitude (1 a.u.). The red and blue markers indicate the anomalies observed in C_{33} and C_{44} (using quartz transducers) measurements respectively. The white dotted lines indicate the T_C and T_N bondaries of Tm reported in Zochowski and McEwen (1992).

signal amplitude plot was constructed with MathCAD software, figure 5.20. The EMAT signal amplitude in the contour plot is divided into 10 levels where the blue shaded regions indicate the lowest EMAT signal amplitude and the red shaded regions indicated the highest EMAT signal amplitude. The red and blue markers in figure 5.20 indicate the anomalies observed in C_{33} and C_{44} (using quartz transducers) measurements respectively. The magnetic phase boundaries, T_C and T_N, reported by Zochowski and McEwen (1992) are indicated by the white dotted lines.

The contour plot shows two high signal amplitude regions, i.e. at the low temperature end (4.2 K to 10 K) and between 55 K and 75 K. An overall increase in the EMAT signal amplitude as H_o is increased could be associated with the increase in the acoustic generation efficiency due to the Lorentz mechanism. High EMAT acoustic coupling efficiency and the anomalies in C_{33} and C_{44} occurred close to T_N. Below T_N = 56 K the EMAT signal amplitude did not show any correlation with the anomalies in the elastic constants. Below 1.0 T the EMAT signal amplitude remained low from 30 K to 55 K despite the anomalies observed in elastic constants data. Within this temperature range Zochowski and McEwen (1992) have reported two magnetic phase boundaries originating from 30.5 K and T_C = 32 K at zero applied field. The EMAT acoustic coupling efficiency did not show large changes to the squaring up of the magnetic moment at 42 K. Furthermore significant increases in the EMAT signal amplitude between 1.3 T to 1. 4 T and 20 K to 38 K can not be associated with any known magnetic phase transition temperatures of Tm. The EMAT signal amplitude measurements were limited to H_o = 1.8 T. The increase in EMAT acoustic coupling efficiency as a function of H_o produced complicated ultrasonic wave-forms where the

mode converted signals became significant where their interference with the main ultrasonic pulse echoes introduces errors in the signal amplitude measurements.

5.5 Conclusion

The anomalies observed in the elastic constants measurements of Tm at zero field are listed in table 5.2.

C_{11}	67 K
C_{44}	33 K and 59 K
C_{33}	26 K, 38 K, 55 K, 68 K, 78 K and 92 K
C_{66}	90 K

Table 5.2. Anomalies observed in the elastic constants of Tm at zero field.

The antiferromagnet-paramagnetic transition (at 56 K) couples strongly to both the shear and longitudinal waves propagating down the c-axis. This is shown by the significant change in the velocities of the ultrasonic waves at 55 K (C_{33}) and 59 K (C_{44}). The changes in the elastic constants at T_C = 32 K was subtle, where the anomaly associated with T_C was only observed in C_{44}.

The propagation of ultrasound down the a-axis proved unusually difficult. The propagation of radially polarised shear wave down the a-axis produces birefringence where the ultrasound energy is steered into the a-axis and c-axis polarised components. The latter had a lower attenuation. Approaching the Néel temperature the EMAT acoustic coupling efficiency for the c-axis polarised shear wave increases but the a-axis polarised shear wave only showed a marginal change in its signal amplitude.

C_{33} and C_{44} as a function of temperature show the softening of Tm with the application of magnetic field parallel to the c-axis. The effect is most significant with magnetic field > 3.0 T. A possible ferrimagnetic - ferromagnetic transition may have occurred with the c-axis applied field > 3 T at 42 K.

The increase in EMAT signal amplitude was greatest close to $T_N = 56$ K but the other observed increase in the EMAT signal amplitude could not be associated with known magnetic phases transition temperatures of Tm.

References

Åström H.U., Nogues J., Nicolaides G.K., Rao K.V. and Benediktsson G., 1991, J. Condens. Matter, **3**, pp 7395-7402.

Fort D 1991, J. Alloys and Comp. **177**, pp.31 - 47.

Greenough R .D., 1978, J. Magn. Magn. Mat **8**, pp286.

Koehler W.C., Cable J.W., Wollan E.O. and Wilkinson M.K., 1962, Phys. Rev. **126** pp 1672.

McEwen K.A., Steigenberger U. and Jensen J. , J. Magn. Magn. Mat. **140 - 144** (1995) pp 767-768.

Musgrave M.J.P., 1970, "Crystal Acoustics. Intro. To The Study Of Elastic Waves And Vibrations In Crystals", Holden-Day, San-Francisco.

Palmer S.B., Lee E.W and M.N. Islam, Proc. Roy. Soc. (London) **A328** (1974) pp 341.

Palmer S.B. and Lee E.W., Proc. Roy. Soc. (London) **A327** (1972) pp 519.

Tonnies J.J., Gschneidner K.A. and Spedding F.H., J. Appl. Phys. **42** (1971) pp 3275.

Steigenberger U., McEwen K.A., Martinez J.L. and Jensen J. 1992, Physica B, **181**, pp158-160.

Zochowski S.W. and McEwen K.A 1992, , J. Magn. Magn. Mat, **104-107**, pp1515-1516.

Chapter 6

Ultrasound Measurements Of Erbium-Thulium Alloy

6.0 Introduction

In the previous two chapters the results from the ultrasound measurements conducted on single crystals of Erbium and Thulium were presented and discussed. Similar experiments have been carried out on two binary alloys of these two metals. The results are presented here in three sections. The first section shows the EMAT acoustic coupling efficiency as a function of temperature and is followed by results of measurements of the elastic properties as a function of temperature. The static applied magnetic field is varied from 0 to 3.0 T. In the last section, the EMAT signal amplitude is used to construct a tentative magnetic phase diagram of $Er_{91.6\%}Tm_{8.4\%}$.

6.1 The Er-Tm Samples.

Single crystals with two different compositions of the alloy were produced, i.e. (a) $Er_{93.3\%}Tm_{6.7\%}$ and (b) $Er_{91.6\%}Tm_{8.4\%}$, where the composition is indicated as atomic weight percentage. The samples were single crystals grown by the solid-state induction method described by Fort (1991). The purity of the starting materials were 99.99 %

weight. For the $Er_{93.3\%}Tm_{6.7\%}$ composition two crystals were grown; they were cut with faces to allow the ultrasound measurements of the C_{11}, C_{33}, C_{44} and C_{66} elastic moduli. C_{12} can be calculated from the C_{66} and C_{11} measurements, see section 2.1. C_{13} elastic modulus was not measured due to difficulties in producing parallel faces perpendicular to an axis at 45° to the c-axis of the crystal. Both samples were cylindrical with the end faces spark planed perpendicular to the crystallographic a and c axes. The length and diameter of the $Er_{93.3\%}Tm_{6.7\%}$ crystals were; l = 4.285 mm and d = 5.267 mm for the c-axis crystal and l = 4.049 mm and d = 5.403 mm for the a-axis crystal.

The $Er_{91.6\%}Tm_{8.4\%}$ sample was initially a cylinder centred on the a axis, allowing C_{11} and C_{66} to be measured prior to planing the c-axis flats to permit the measurements of C_{33} and C_{44}.

6.2 Elastic Constants Measurements.

Results from the measurement of elastic constants for the different crystallographic directions of the Er-Tm sample are presented in this section. The ultrasound measurements using quartz are presented first and then followed by the results from ultrasound measurements conducted with EMATs. The results are presented in the form of the elastic constants as a function of temperature at various static applied magnetic fields. The densities of the sample are taken to be $\rho = 9160.12$ kgm^{-3} and $\rho = 9157.06$ kgm^{-3} [MacPDF software with x-ray crystallographic data] for

$Er_{91.6\%}Tm_{8.4\%}$ and $Er_{93.3\%}Tm_{6.7\%}$ respectively, calculated from pure Er and Tm data. Since the properties of rare earth are very similar the calculation assumes a linear relation in density between Er and Tm.

The elastic constants measured at room temperature (zero field) for both samples were very similar. They are the same when the experimental error of ± 0.5 GPa is taken into account. For $Er_{93.3\%}Tm_{6.7\%}$: C_{11} = 83.5 GPa, C_{33} = 80.5 GPa, C_{44} = 28.8 GPa and C_{66} = 30.0 GPa.

6.2.1 c-axis Measurements.

Figure 6.1 shows C_{44} as a function of temperature for $Er_{91.6\%}Tm_{8.4\%}$ at zero field. The sample was initially cooled and when the sample reached 4.2 K it was then warmed up. Hysteresis was observed between ~65 to ~ 85 K. On cooling the velocity gradually increases until ~ 80 K when it increased rapidly to a maximum of 1818 ms^{-1} and then started to decrease smoothly except for a small anomaly around 24 K. Using quartz transducers the lowest temperature attainable for any useful data to be collected was ~ 15 K. The attenuation of the shear wave was such that only one reflected echo was observed. Figure 6.2 shows the attenuation as a function of temperature. The anomalies observed in C_{44} were: 15 K, ~24 K, 56 K and 80 K. The latter anomaly corresponds to $T_{N\parallel}$ = 80 K. The 24 K anomaly is associated with the decoupling of the modulation of the basal plane moments and the c-axis components (26 K) [Parnell *et al.* (1998)].

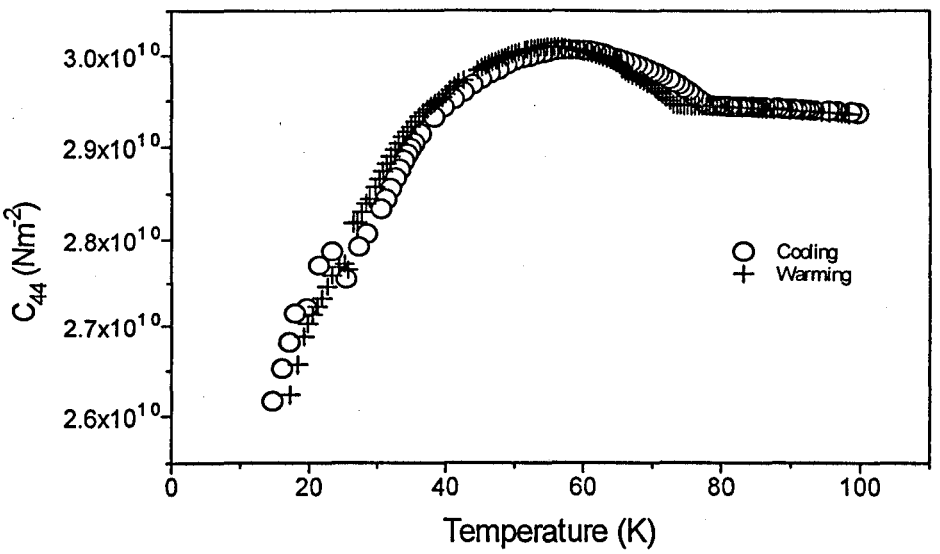

Figure 6.1. C_{44} versus temperature for $Er_{91.6\%}Tm_{8.4\%}$ at 0 T.

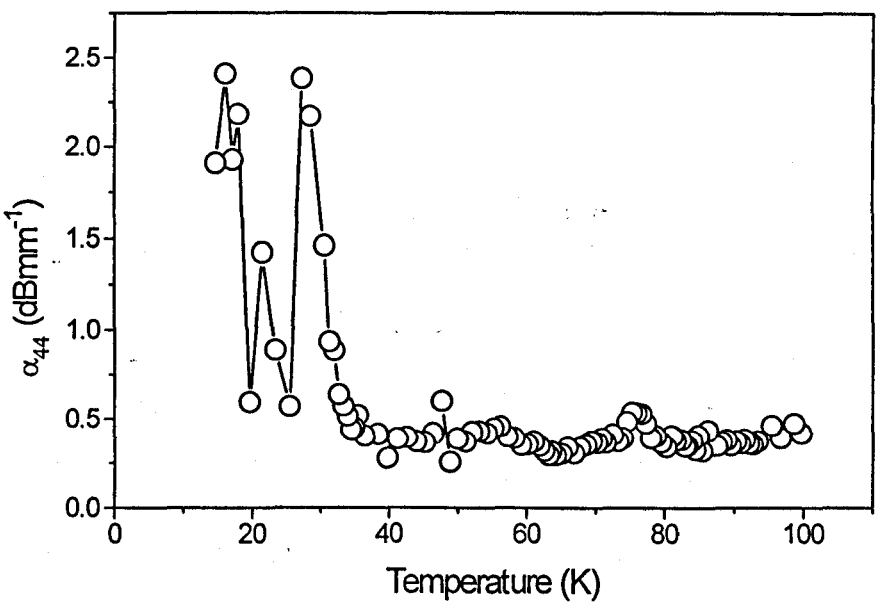

Figure 6.2. Attenuation of c-axis propagated shear wave in for $Er_{91.6\%}Tm_{8.4\%}$ at zero field. Data recorded while sample was cooled. Error ± 15 %.

Figure 6.3, shows C_{44} as a function of temperature with the application of a static magnetic field parallel (at 0.5 T, 0.75 T and 1.0 T) to the c-axis for the $Er_{91.6\%}Tm_{8.4\%}$ sample. The anomaly observed at 24 K, which corresponds to the decoupling of basal plane moments from c-axis components, was not observed when a c-axis magnetic field was applied. At low fields < 2.0 T there was no significant change to the shear velocity.

Figure 6.4 shows C_{44} as a function of temperature in applied magnetic fields: 3.0 T and 4.0 T for $Er_{93.3\%}Tm_{6.7\%}$. However, with the applied magnetic field > 2.0 T obvious effects were observed to the shear velocity and hence C_{44}. At 3.0 T, C_{44} decreases at first slowly as the sample was cooled below 80 K (Néel temperature $T_{N\|}$) and then a marked increase was observed at 67 K, indicating the suppression of $T_{N\|}$. This increase in C_{44} continued until the sample was at 60 K. A smooth decrease in the elastic modulus was then observed. It levelled off at 38 K and then began to increase as the temperature approached 30 K. Immediately below 30 K a drop in C_{44} was observed. This shows the antiferromagnetic structure with basal plane components and c-axis moments phase described by $q=(2/7)c^*$ observed at zero field (Parnell *et al.*, 1998) has been changed with the c-axis applied field > 3 T. Below ~ 26 K no useful data could be estimated due to high signal attenuation. Figure 6.5 shows the ultrasonic attenuation as a function of temperature with c-axis applied field at 3 T. Increasing the applied magnetic field further to 4.0 T removed the hump observed at 3.0 T. At 4.0 T, C_{44} decreases smoothly and then increases at ~ 40 K. The experiment was terminated at 29 K due to high attenuation of the ultrasound echoes.

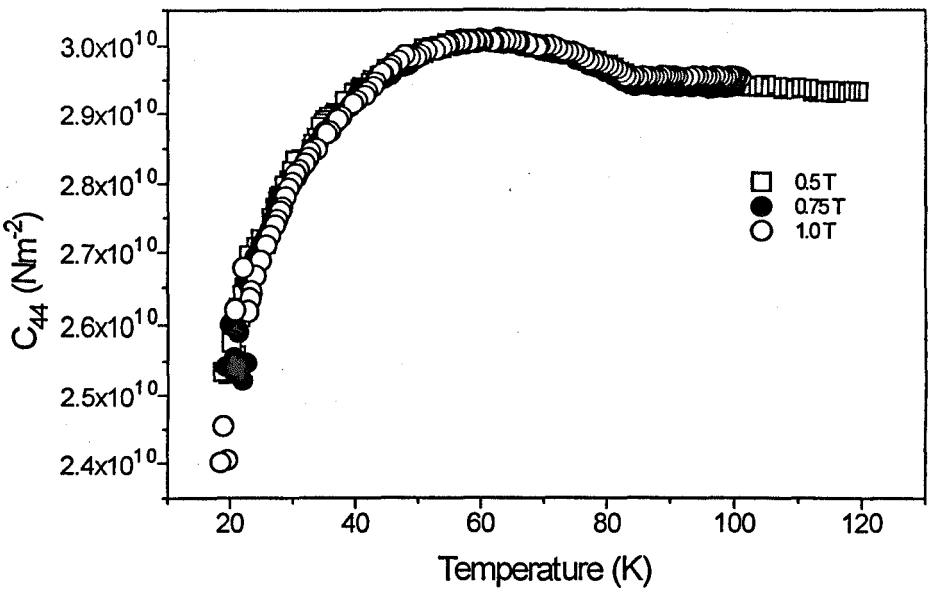

Figure 6.3. C_{44} as a function of temperature for $Er_{91.6\%}Tm_{8.4\%}$. Applied magnetic field parallel to the c-axis.

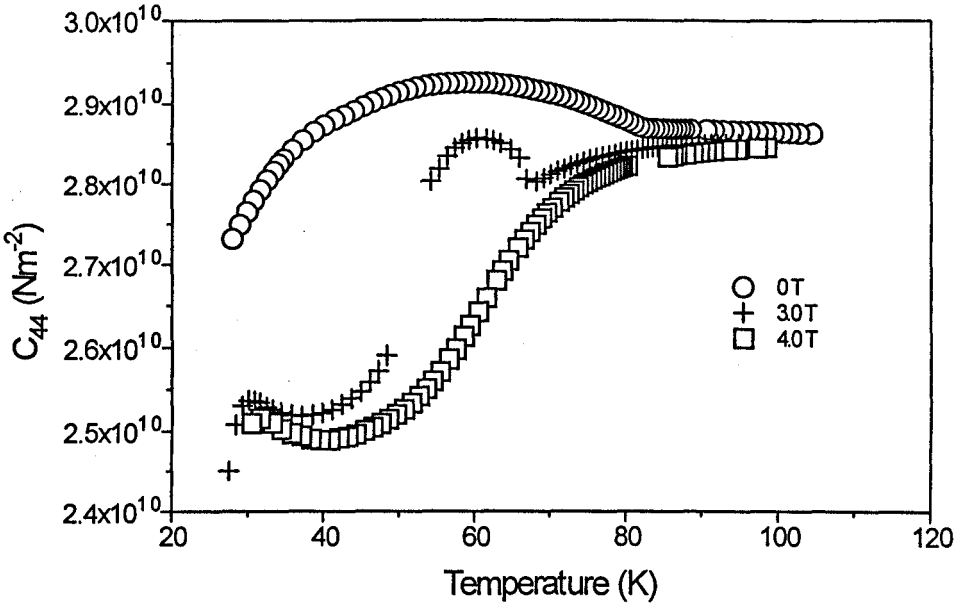

Figure 6.4. C_{44} as a function of temperature for $Er_{93.3\%}Tm_{6.7\%}$. Applied magnetic field parallel to c-axis.

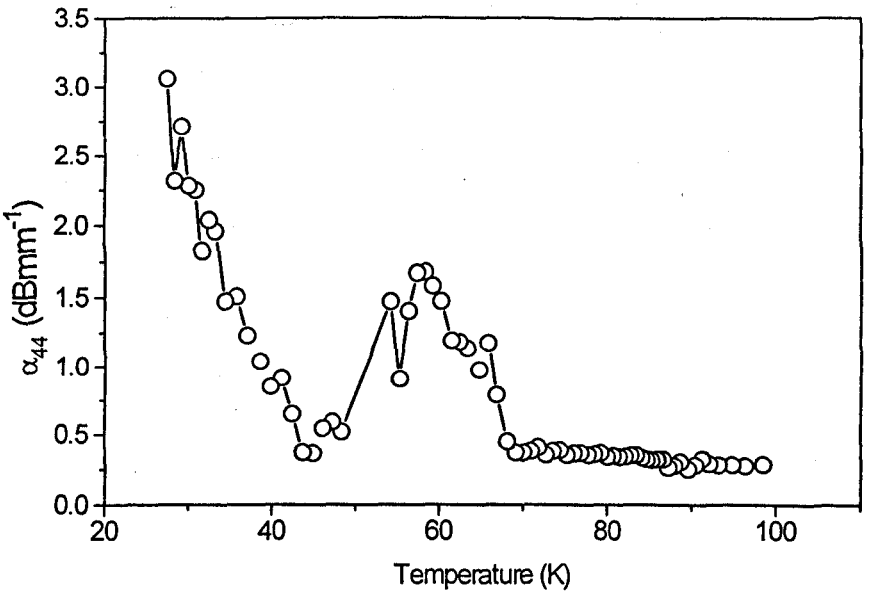

Figure 6.5. Attenuation of c-axis propagated shear wave in $Er_{93.3\%}Tm_{6.7\%}$ with c-axis applied magnetic field at 3 T.

Figure. 6.6 to figure. 6.8 show a series of C_{33} measurements as a function temperature and magnetic field for $Er_{91.6\%}Tm_{8.4\%}$ and $Er_{93.3\%}Tm_{6.7\%}$. In zero field, step like anomalies were observed in C_{33} at 21 K, 44 K and 80 K on cooling, showing first order phase changes at these temperatures. The latter anomaly is associated with the Néel temperature. The 21 K anomaly corresponds to the cycloid phase with decoupling of the modulation of the basal plane and c-axis components magnetic moments, i.e. wobble of the cycloid in the a-c plane. The transition from the c-axis modulated antiferromagnetic phase to the cycloid phase was observed between 26 K to 47 K, [Parnell *et al.*, 1997]. Hysteresis in the velocity of ~ 4 K is observed at all three phase transitions as shown in the expanded views in figure 6.6 b, c and d. The features observed in C_{33} as a function of temperature for Er-Tm are similar to those reported by Eccleston and Palmer (1992) for pure single crystal Er. In Er-Tm there was no evidence of the c-axis cone structure down to 2 K [Parnell *et al.*, 1998]. The effect of an applied magnetic field parallel to the c-axis is minimal below 0.5 T, figure 6.7. The attenuation (α_{33}) of longitudinal wave propagating down the c-axis at zero field is shown in figure 6.9.

Figure 6.8 shows the effect of applied c-axis magnetic field for the $Er_{93.3\%}Tm_{6.7\%}$ sample. At zero field C_{33} for $Er_{93.3\%}Tm_{6.7\%}$ is similar to that of $Er_{91.6\%}Tm_{8.4\%}$. At 1.0 T changes to C_{33} are significant, especially below 18 K. Instead of increasing steadily, C_{33} continued to decrease below 18 K and levelled off at ~ 10 K. At zero field between 9 K to 18 K Er-Tm has been shown to have the cycloid phase. Increasing the magnetic field caused even more drastic changes to C_{33} as illustrated in figure 6.13. At 3.0 T T_N seems

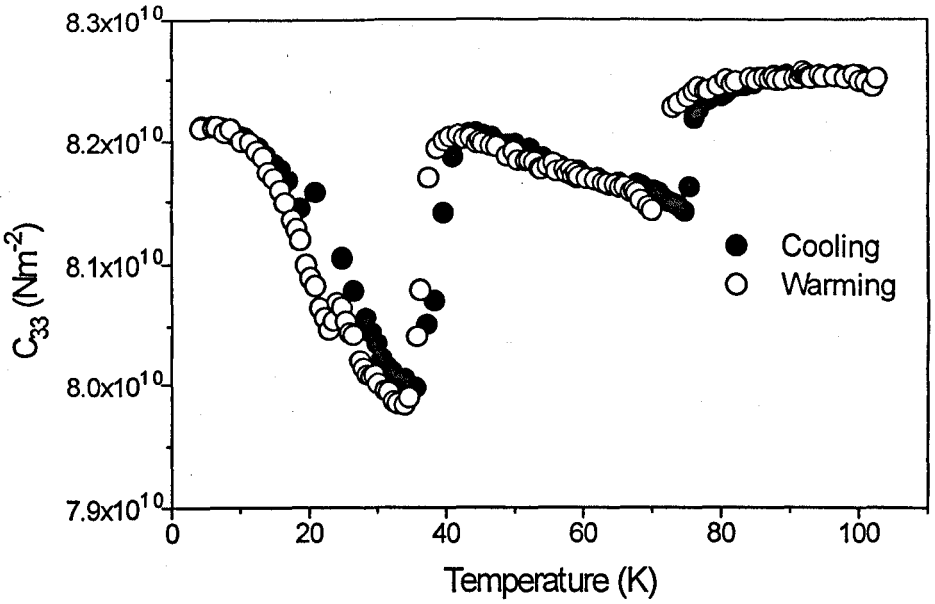

Figure 6.6a. C_{33} as a function of temperature for $Er_{91.6\%}Tm_{8.4\%}$.

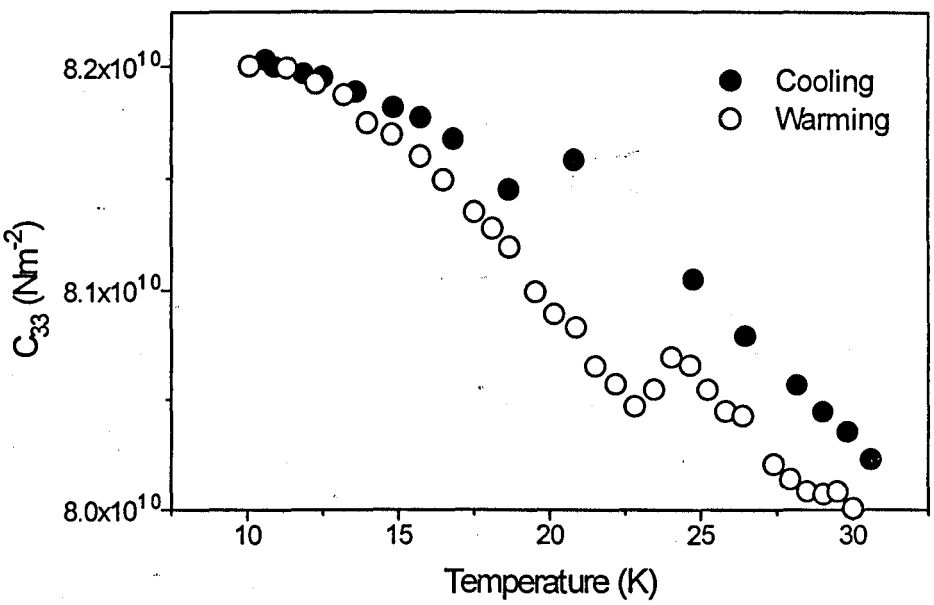

Figure 6.6b. C_{33} as a function of temperature for $Er_{91.6\%}Tm_{8.4\%}$.

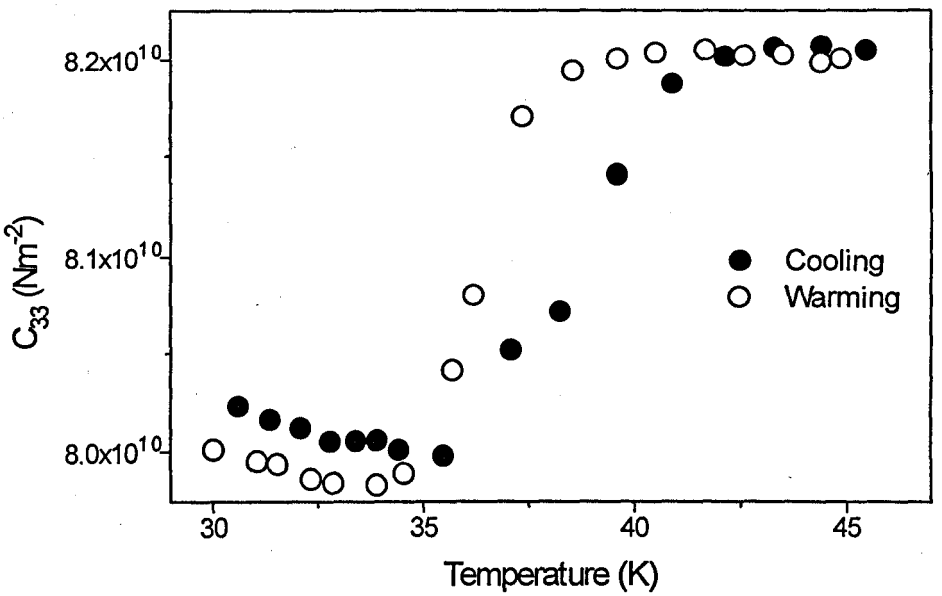

Figure 6.6c. C_{33} as a function of temperature for $Er_{91.6\%}Tm_{8.4\%}$.

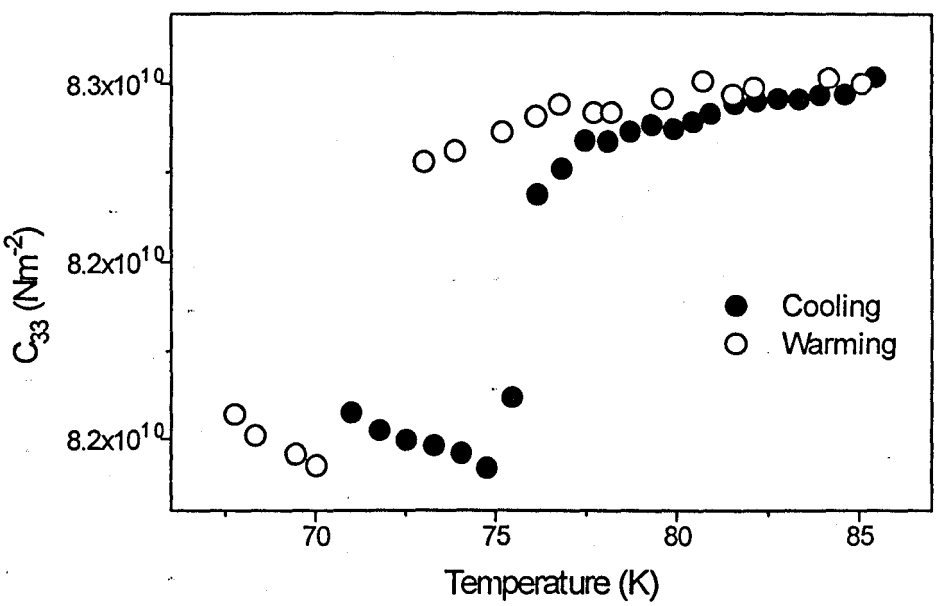

Figure 6.6d. C_{33} as a function of temperature for $Er_{91.6\%}Tm_{8.4\%}$.

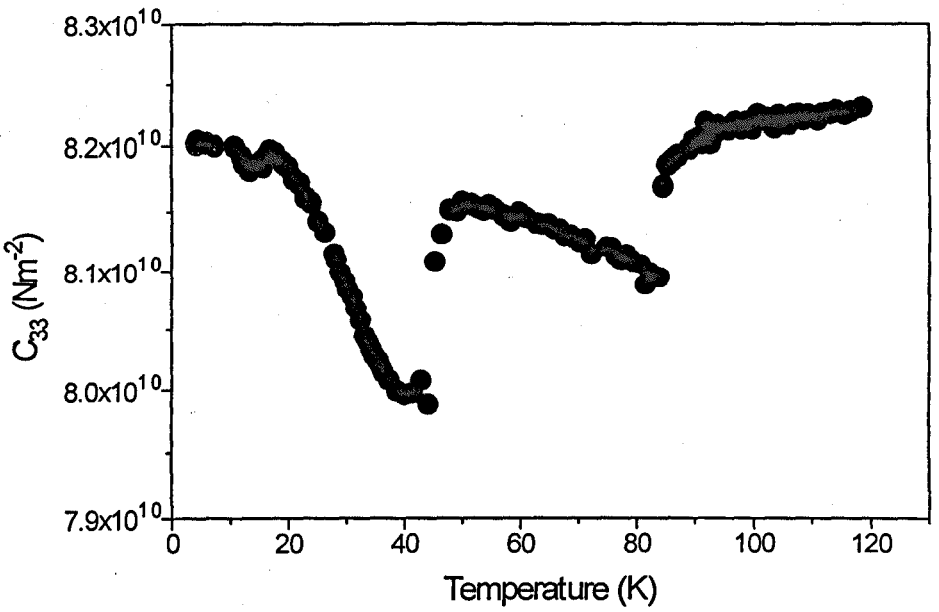

Figure 6.7. C_{33} as a function of temperature for $Er_{91.6\%}Tm_{8.4\%}$ at 0.5 T. Applied magnetic field parallel to c-axis.

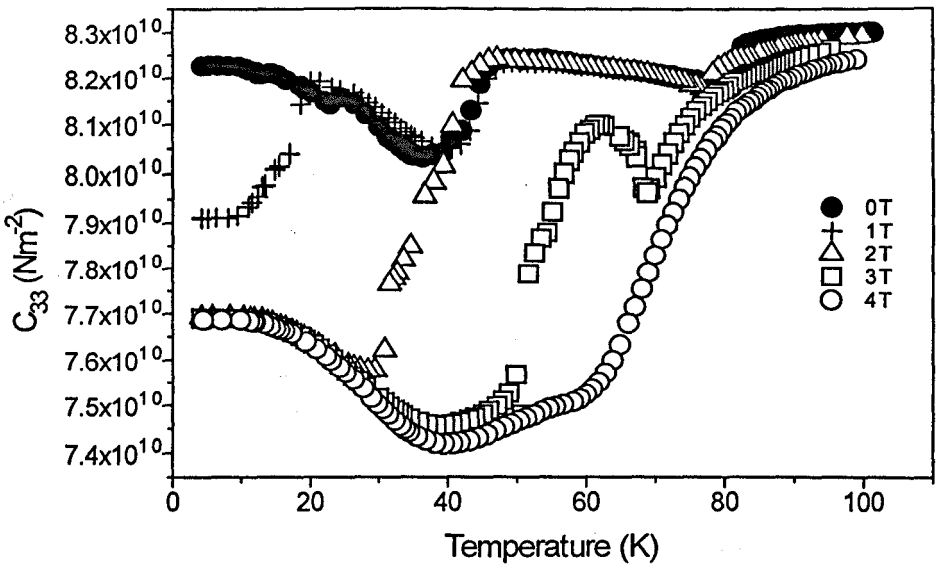

Figure 6.8. C_{33} as a function of temperature for $Er_{93.3\%}Tm_{6.7\%}$. Applied magnetic field parallel to c-axis.

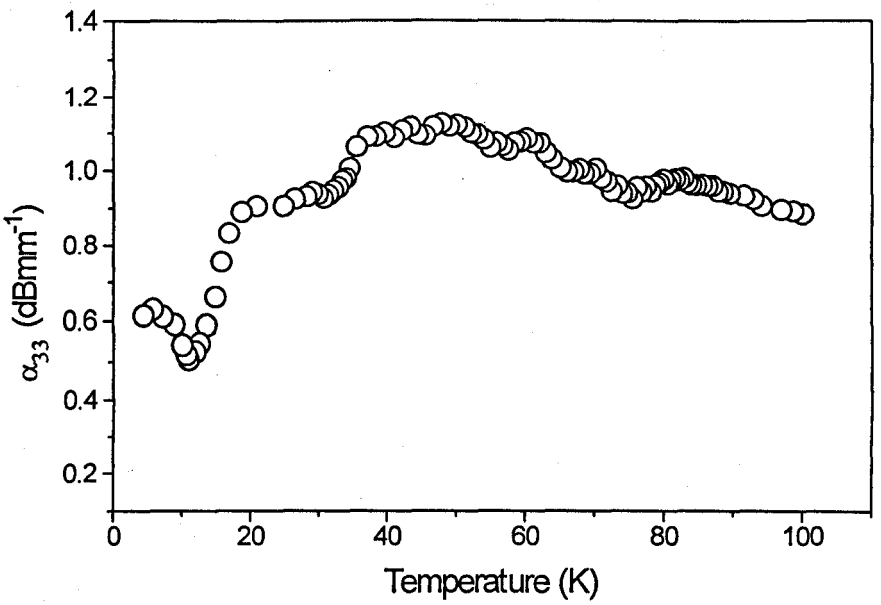

Figure 6.9. C-axis propagated longitudinal wave attenuation (α_{33}) in $Er_{93.3\%}Tm_{6.7\%}$ as a function of temperature at zero applied field.

to be suppressed and at 4.0 T the step like features were completely removed and replaced by a smooth variation of C_{33} as a function of temperature. The response of the material as reflected by C_{33} and C_{44} are very similar at 3.0 T.

6.2.2 a-axis Measurements

C_{11} measurements as a function of temperature and applied magnetic field for $Er_{91.6\%}Tm_{8.4\%}$ is shown in figure 6.10. At 0 T anomalies were observed at 25 K, 38 K, 44 K and 80 K. At zero applied field C_{11} shows a change in gradient at $T_N = 80$ K. The material began to soften (44K) when the basal plane component of the moments develop, i.e. transition into the cycloid phase. The formation of the basal plane magnetic moment increases the strain along the a-axis. The ultrasound attenuation became high at the cycloid phase as shown in figure 6.11. C_{11} increases, with corresponding decrease in the attenuation, once the basal plane components of the magnetic moments are formed. The applied magnetic field in the a-axis direction has drastic effects on C_{11} where an applied magnetic field of > 0.5 T was required to induce significant changes in C_{11}. The a-axis applied magnetic field could have assisted in the formation of the basal plane components of the magnetic moments (enhanced formation of the cycloid phase). In the c-axis measurements, the applied field had to be > 2 T before significant changes in the elastic constants were observed.

The shear wave propagation down the a-axis with polarisation in the b-axis direction provided the C_{66} measurements. C_{66} as a function of temperature for

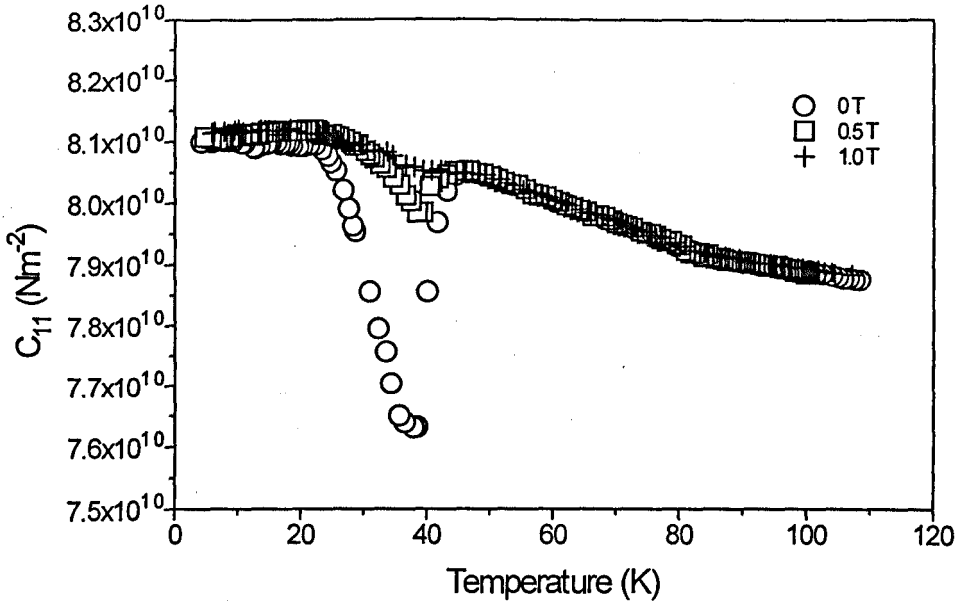

Figure 6.10. C_{11} as a function of temperature for $Er_{91.6\%}Tm_{8.4\%}$. Applied field parallel to the a-axis.

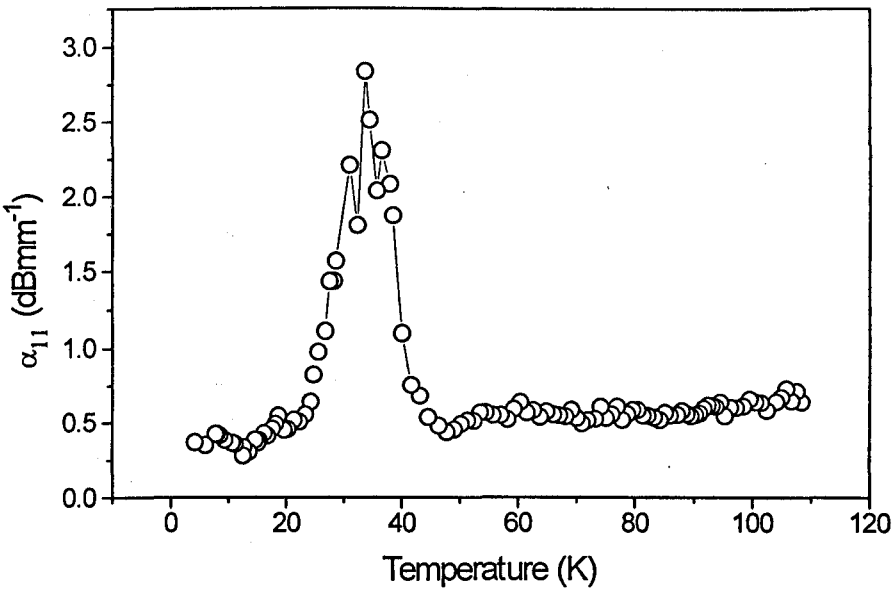

Figure 6.11. A-axis propagated longitudinal wave attenuation (α_{11}) in $Er_{91.6\%}Tm_{8.4\%}$ as a function of temperature at zero applied field.

$Er_{91.6\%}Tm_{8.4\%}$ is shown in figure 6.12. The data was obtained while the sample was cooled at ~ 0.8 $Kmin^{-1}$. At 0 T anomalies were observed at 15 K, 24 K, 37 K, 45 K and 80 K. As the sample was cooled C_{44} increased gradually. A change in gradient was observed at ~ 80 K (Néel temperature) and below this temperature the shear wave velocity continued to increase more rapidly. A sharp decrease in the velocity occurred at 45 K which reached a minimum of 1754 ms^{-1} ($C_{66} = 2.82 \times 10^{10}$ Nm^{-2}) at 37 K. This anomaly occurred close to the magnetic phase transition temperature of 47 K where an anti-ferromagnetic structure with a basal plane and c-axis component modulated by the same wavevector, $q = (2/7)c^*$ is formed. Further cooling saw the velocity rapidly increased to ~ 1900 ms^{-1} ($C_{66} = 3.31 \times 10^{10}$ Nm^{-2}) at 24 K and below this temperature and down to the lowest attainable temperature of 4.2 K, the velocity became constant at 1896 ms^{-1}. The attenuation of the b-axis polarised shear wave propagating down the a-axis also showed anomalies at the temperature reported above, figure 6.13.

With the application of a static magnetic field parallel to the a-axis, the magnetic ordering was biased in the magnetic field direction and this led to drastic changes in the elastic properties of the material. This is reflected on the C_{66} measurements as a function of temperature with the application of magnetic field, figure 6.12. The dip at 37 K was greatly reduced with increasing magnetic field. This is very similar to the behaviour of the longitudinal wave propagated down the a-axis with an a-axis applied field.

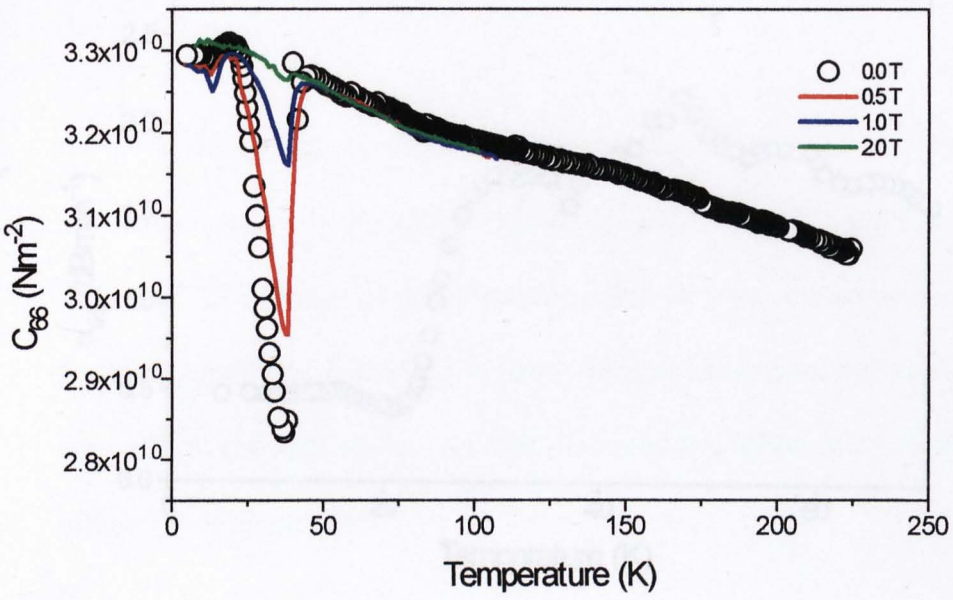

Figure 6.12. C_{66} as a function of temperature for $Er_{91.6\%}Tm_{8.4\%}$. Applied magnetic field along the a-axis.

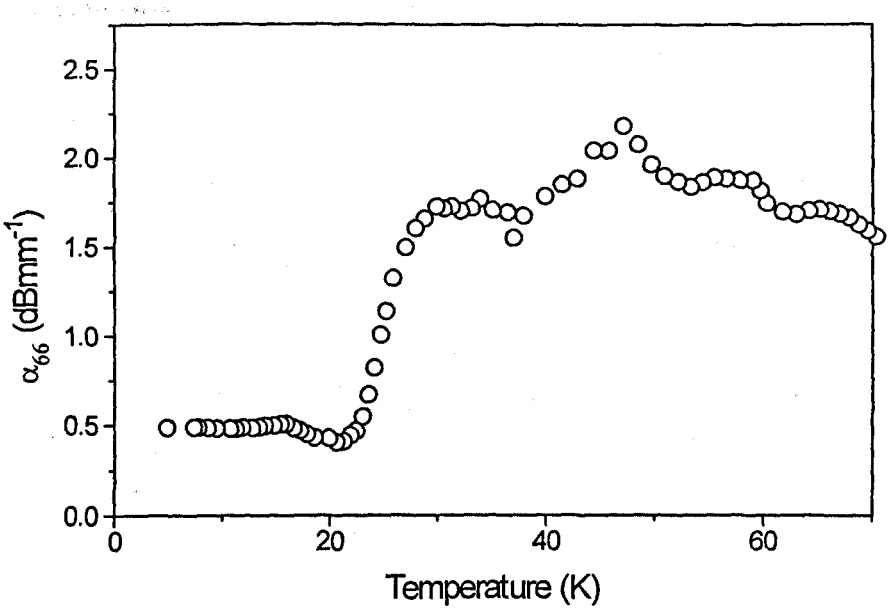

Figure 6.13. Attenuation (α_{66}) of b-axis polarised shear propagating down the a-axis in $Er_{91.6\%}Tm_{8.4\%}$ at zero field.

6.3 Ultrasound Studies Of Er-Tm Using EMATs.

In this section the results and discussions from the ultrasound studies of the Er-Tm samples using EMATs are presented. In-plane spiral coil and linear coil EMATs were used. The former produces radially polarised shear waves whereas the later produces longitudinal waves. The elastic constant measurements as a function of temperature and applied field are first presented and followed by the EMAT acoustic efficiency measurements.

6.3.1 EMAT Generated Shear Wave Velocity Measurements.

The velocity measurements were taken simultaneously with the amplitude measurements. Figure 6.14 shows C_{44} as a function of temperature for $Er_{91.6\%}Tm_{8.4\%}$ at static fields of; 0.5, 0.75 and 1.0 T. The applied field was parallel to the c-axis. Data were recorded while the sample was cooled. The increase in the velocity was gradual, 0.25 $ms^{-1}K^{-1}$, from 115 K to 88 K. A change in the gradient was observed at ~ 87 K. No useful data could be measured with the shear EMAT between 65 to 72 K due to the low acoustic coupling efficiency of the EMAT. The lowest temperature where useful velocity data could be obtained was 19 K, below which the waveform became complicated with mode converted signals and also the generation of longitudinal a wave became more dominant. The EMAT results are very similar to the ones obtained using quartz transducers. This provided confidence in the use of EMATs in the ultrasound studies of single crystals rare earth.

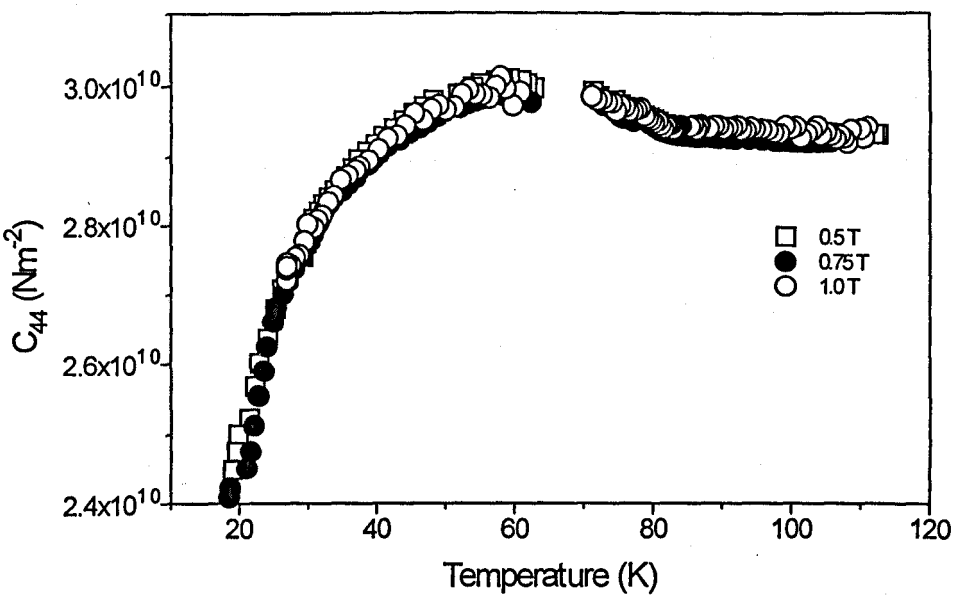

Figure 6.14. C_{44} as a function of temperature for $Er_{91.6\%}Tm_{8.4\%}$. EMAT generated in-plane radially polarised shear wave. Applied magnetic field parallel to the c-axis.

6.3.2 EMAT Generated Longitudinal Wave Velocity Measurements.

Figure 6.15 shows the C_{33} versus temperature for $Er_{91.6\%}Tm_{8.4\%}$. Obvious changes in the velocity are observed at; 15 K, 18 K ,20 K, 40 K, 45 K and 85 K. Additional features were observed at 0.5 T in the temperature range of 35 K to 42 K. The velocity dropped rapidly at 85 K followed by a steady increase, (0.5 $ms^{-1}K^{-1}$), at 45 K where the next drop in the velocity occurred. A minimum at 40 K was observed. On further cooling the velocity increases at ~20 K and showed another sharp drop at 18 K. Below 15 K temperature no useful data could be obtained again due to the complicated waveforms. The "steps" features were present in the C_{33} curves but close inspection shows differences in C_{33} when compared to the ones obtained with quartz transducers. It must be emphasised that the direction of the applied magnetic field was along the a-axis for the EMATs measurements whereas the in quartz measurements the applied field was set along the c-axis. The effects of the a-axis applied magnetic field is most profound in the cycloid phase of the material (< 47 K). Instead of a sharp change at ~ 40 K as observed in the quartz measurements of C_{33}, figures 6.6 - 6.8, the application of the a-axis magnetic field delayed the increase in C_{33} to a lower temperature (~ 30 K). C_{33} decreased rapidly as the sample temperature approaches 15 K.

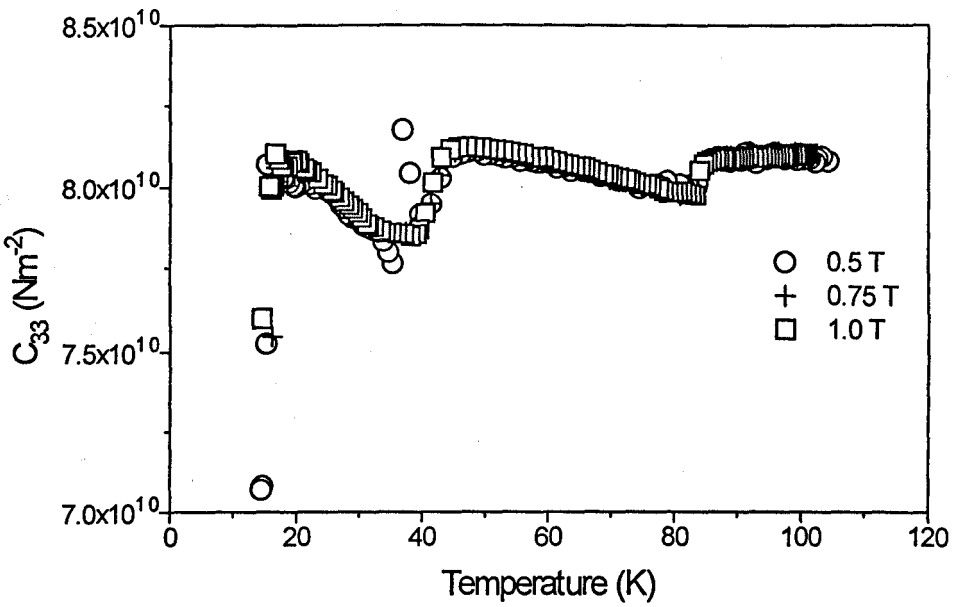

Figure 6.15. C_{33} as a function of temperature with a-axis applied magnetic field for $Er_{91.6\%}Tm_{8.4\%}$. EMAT generated longitudinal wave.

6.3.3 EMAT Signal Amplitude Measurements

The signal amplitude of the ultrasound echoes were measured as a function of temperature and magnetic field. The EMAT signal amplitude displayed in the results were from the third echo in the ultrasound wave train.

Figure 6.16 shows the EMAT signal amplitude as a function of temperature and applied magnetic field for $Er_{91.6\%}Tm_{8.4\%}$. The static applied magnetic field was set parallel to the crystallographic c-axis of the sample and the radially polarised shear waves was propagated down the c-axis. Several temperature sweeps at constant magnetic field were carried out. The temperature sweep rate was $\sim 0.05\ Ks^{-1}$. The data sets for 0.75 and 1.0 T are displaced by adding 4 arbitrary units (a.u.) and 8 a.u. respectively for the purpose of presentation. The error in the amplitude measurement is $\sim \pm 10$ %. The lowest magnetic field where signal can be usefully observed across the temperature range (4.2 to 110 K) was 0.5 T. The data were obtained while the sample was cooled and the first peak in the signal amplitude was observed at ~ 85 K. The signal amplitude then decreased and at ~ 70 K the signal to noise ratio fell below the cut-off level of 2:1. The signal recovered again at ~ 61 K. The signal began to rise again at ~ 40 K. At 0.5 T the signal amplitude then settled to a constant level, "flat" region, between ~ 25 K and ~ 38 K before a sharp rise occurs as the sample approaches 20 K. As the c-axis applied field was increased this "flat" region became narrower. Below 19 K the waveform became complicated by the interference of mode converted echo pulses, (as illustrated in figure 6.17 for magnetic fields > 2.2 T at 77 K). The reflected shear echoes

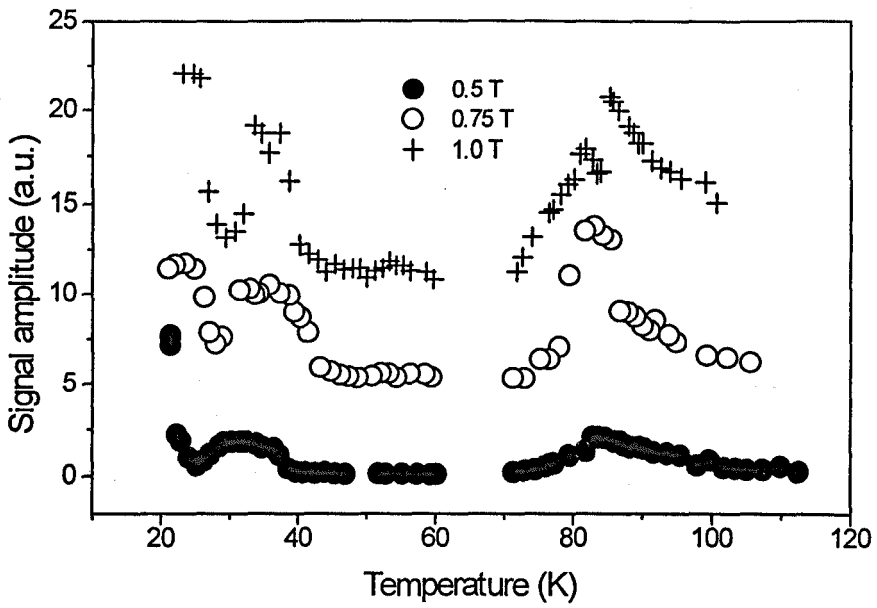

Figure 6.16. In-plane radially polarised shear wave EMAT's coupling efficiency as a function of temperature for $Er_{91.6\%}Tm_{8.4\%}$. The 0.75 T and 1 T curves were displaced by 4 a.u. and 8 a.u. for display purpose.

are labelled 2S, 4S, 6S etc. As the magnetic field is increased, longitudinal waves were observed and they are labelled 2L, 4L etc. LS denotes the mode converted longitudinal to shear or vice-versa as they have the same arrival time. The mode converted signals are combinations of the 2S, 2L and LS. At 2.6 T, figure 6.17, the mode converted signals run into the main shear pulses and produces interference. This greatly increase the errors in the amplitude measurements where even the identification of the shear pulse can become difficult. Figure 6.17 also show the isotropic nature across the a-b plane of Er-Tm. No birefringence effect was observed even though the polarisation of the shear wave was across the whole of the a-b plane.

The in-plane radially polarised EMAT signal amplitude measurements showed an increase in the EMAT acoustic coupling efficiency occurring close to the magnetic transition temperatures of the material. As the sample was cooled the first increase in the EMAT signal at 85 K corresponds to the paramagnetic - antiferromagnetic phase transition. The EMAT acoustic efficiency also showed an increase in the cycloid phase of Er-Tm. The increase in the EMAT acoustic coupling efficiency did not occurred close to the cycloid phase transition temperature of 47 K. Instead the EMAT signal amplitude peaked at ~ 38 K. The shear wave attenuation, figure 6.2, showed an increase from ~ 38 K and peaked at 30 K before dropping to a minimum at 26 K. This trend was also observed in the EMAT signal amplitude, figure 6.16. At 26 K (zero field), the basal plane components of the magnetic moments became decoupled from the c-axis modulated components. The increase in the EMAT signal amplitude as the sample temperature approaches 20 K could be associated with the formation of the magnetic

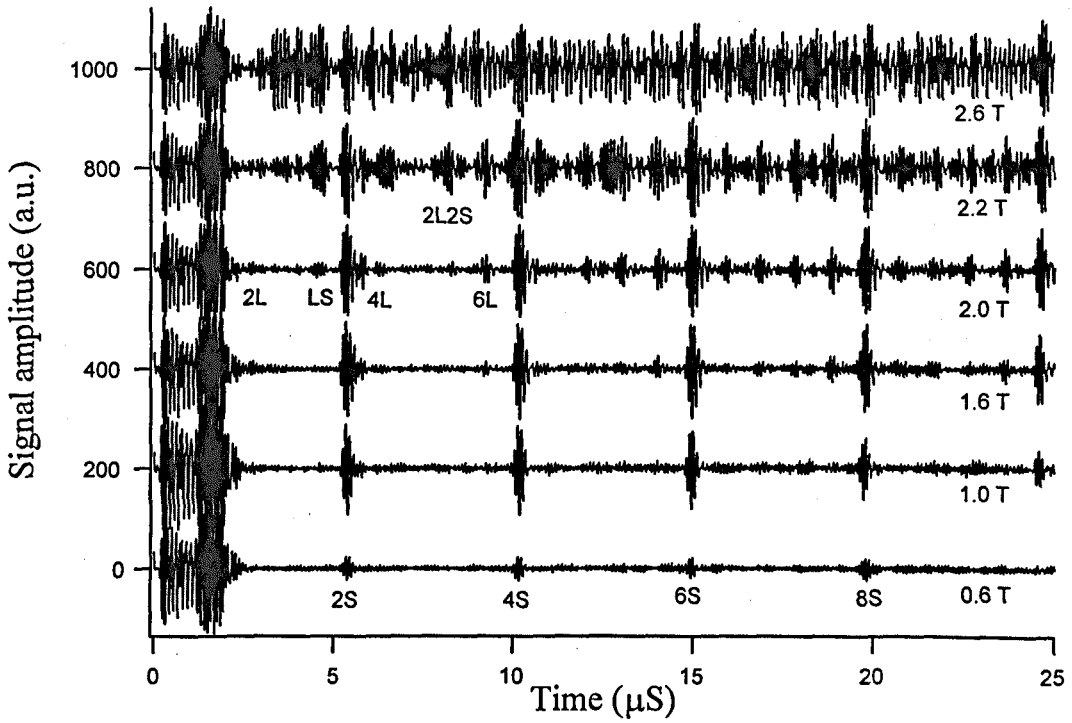

Figure 6.17. In-plane radially polarised shear wave EMAT generated ultrasonic waveform at 77 K for $Er_{91.6\%}Tm_{8.4\%}$. Wave propagation down the c-axis and the applied magnetic field parallel to the c-axis. L = longitudinal wave echo, S = shear wave echo and LS = mode converted longitudinal to shear or vice-versa.

structure described by a single q-vector and q/2 modulation for the basal plane components of the moments [Parnell *et al.*, 1998].

The next set of results, figure 6.18, show the longitudinal EMAT signal amplitude as a function of temperature. The longitudinal wave was propagated down the c-axis with an a-axis applied magnetic field. In cooling the sample with applied field at 0.5 T, the first significant change in the EMAT signal amplitude was at ~ 85 K. This step like feature became less pronounced and was shifted to a lower temperature when the a-axis applied magnetic field was increased. The next significant change in the EMAT signal amplitude was at 80 K (Néel temperature). The EMAT signal amplitude peaked at ~ 50 K (close to the formation of the cycloid phase, 26 K - 47 K). It then levelled off between ~ 26 K to ~ 30 K (26 K decoupling of the basal plane component) before further decrease in the signal amplitude was observed. This change in the EMAT signal amplitude close to 20 K is opposite to the behaviour of the shear wave EMAT signal amplitude, see figure 6.16. The longitudinal wave attenuation at zero field, figure 6.9, also showed similar trend to the longitudinal EMAT signal amplitude. The increase in the a-axis applied field has a slightly higher acoustic generation efficiency but have similar features to the 0.5 T curve. The overall increase in the EMAT signal amplitude is a contribution from the Lorentz mechanism.

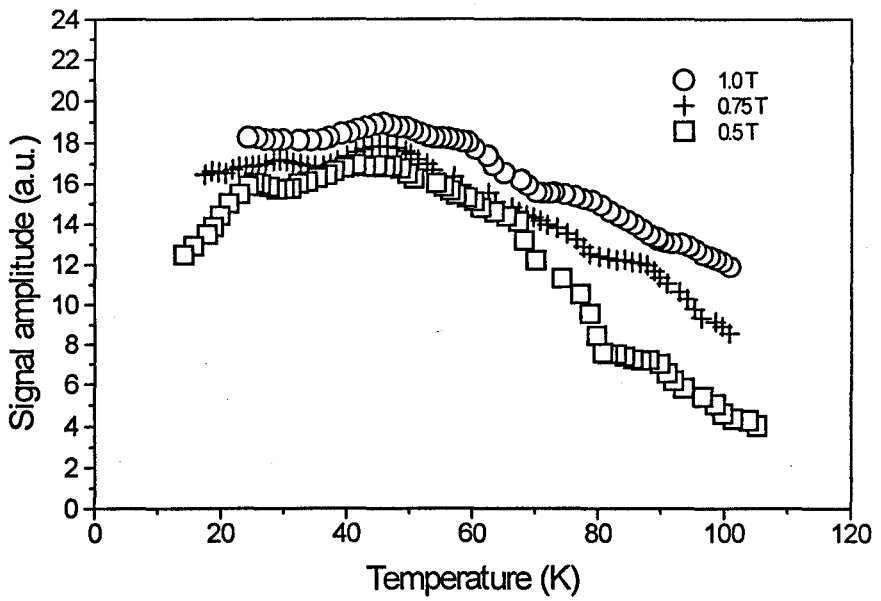

Figure 6.18. Longitudinal EMAT signal amplitude as a function of temperature. Longitudinal wave propagated down the c-axis of $Er_{91.6\%}Tm_{8.4\%}$ with a-axis applied magnetic field.

6.4 Contour Plot of EMAT Signal Amplitude ($Er_{91.6\%}Tm_{8.4\%}$).

A contour plot was produced from the in-plane radially polarised EMAT signal amplitude, figure 6.19. The scans were carried out by sweeping the c-axis magnetic field with 0.1 T increments at fixed temperatures. The temperature increment of ~ 0.5 T was applied. The data were then loaded into MathCAD, mathematical processing software, for the contour plots to be generated. The contour in figure 6.19 is divided into ten levels with the blue shaded regions set to 1 a.u. and the red shaded regions to 10 a.u.. Distinct regions showing high EMAT acoustic coupling were observed. The EMAT acoustic coupling efficiency is dependent on changes in the magnetic ordering of the material, as shown in the previous two chapters. Hence the variation in the EMAT efficiency may allow us to identify regions that correspond to various magnetic structures for $Er_{91.6\%}Tm_{8.4\%}$. In general an increase in the signal amplitude was observed as the applied magnetic field, H_o, was increased. The markers placed over the contour plot represent the anomalies observed in C_{33} and C_{44} (quartz measurements).

The H_o - T EMAT signal amplitude plot for $Er_{91.6\%}Tm_{8.4\%}$ shown in figure 6.19 summaries the EMAT results for this chapter. The zero field magnetic structures of $Er_{91.6\%}Tm_{8.4\%}$ identified by Parnell *et al.* (1998) can not be use here. It may be assumed at low applied magnetic fields ($H_o < 0.5$ T) the magnetic structures of $Er_{91.6\%}Tm_{8.4\%}$ remained similar to the magnetic structures at zero field. For $H_o < 0.5$ T, figure 6.19 show two high EMAT signal amplitude regions i.e. 27 K to 35 K and 19 K to 23 K, and can be associated with T_C and $T_{N\perp}$ respectively. The high EMAT signal region between

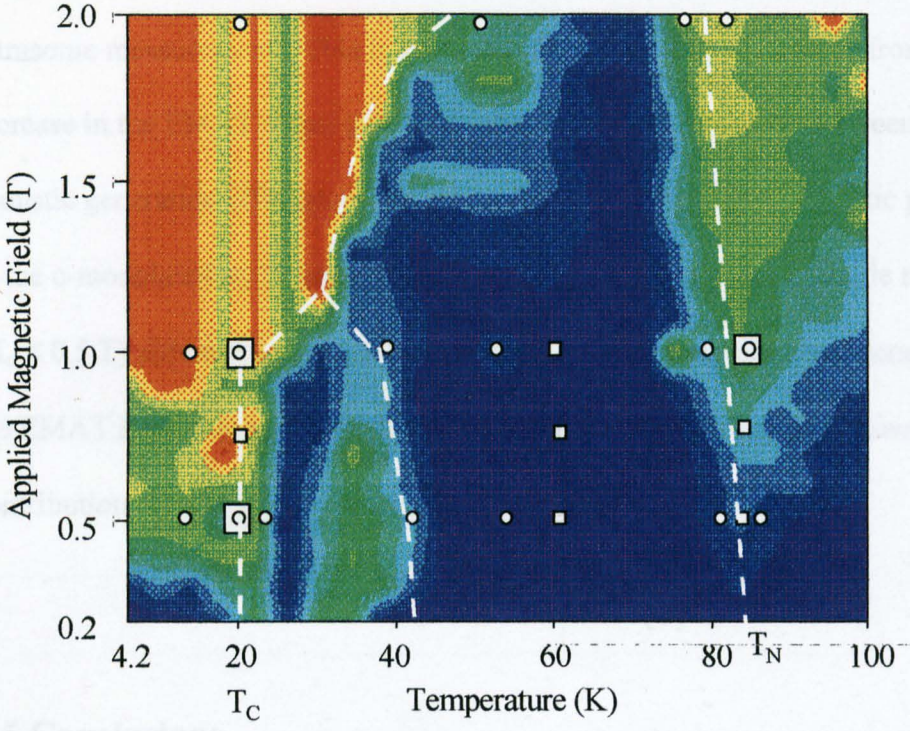

Figure 6.19. H_o - T plot of EMAT signal amplitude for $Er_{91.6\%}$ $Tm_{8.4\%}$.. H_o parallel to c-axis. A ten level contour is used with blue (1 a.u.) corresponding to low EMAT signal amplitude and red (10 a.u.) corresponding to high EMAT signal amplitude. The white circular and square markers are the anomalies observed in C_{44} and C_{33} (quartz transducers measurements) respectively. The white dotted lines show the possible magnetic phase boundaries of the material deduced from the anomalies in C_{33} and C_{44} (quartz) measurements.

19 K to 23 K correlated with the decoupling of the basal plane component from the c-axis component of the magnetic moment, i.e. cycloid phase. The antiferromagnetic - paramagnetic boundary may also be deduced from the observed anomalies in the ultrasonic measurements. This is shown by the dotted line originating from 85 K. The increase in the EMAT signal amplitude showed some correlation between the EMAT acoustic generation efficiency with the antiferromagnetic - paramagnetic phase change. In the c-modulated antiferromagnetic phase the EMAT signal amplitude remained low ($H_o < 0.5$ T) although anomalies in C_{33} and C_{44} were observed. The overall increase in the EMAT signal amplitude with increasing applied magnetic field shows the contribution of the Lorentz mechanism becoming more dominant.

6.5 Conclusions.

The ultrasound studies of Er-Tm have revealed several anomalies in the elastic constants of Er-Tm indicating the possible magnetic transition temperatures of Er-Tm. Table 6.1. shows a list of the observed anomalies in C_{11}, C_{33}, C_{44} and C_{66} with applied field of 0.5 T. Note that for the EMAT C_{33} measurements the applied field was set along the a-axis whereas in the quartz C_{33} measurements the applied field was directed parallel to the c-axis. In the C_{11} and C_{66} (quartz) measurements the applied field was directed parallel to the a-axis. The identified magnetic transition temperatures for Er-Tm at zero field agreed well with those identified by neutron scattering measurements reported by Parnell *et al.* (1998). The use of EMATs for non-contact ultrasound measurement on single crystal of magnetic rare earth samples has been shown to be a viable and useful

technique. The results from the EMATs (non-contact method) and quartz (contact method) measurements for C_{33} and C_{44} too agreed well within the limit of the experimental error.

Temperature (K)		10	15	20	26	40	45	56	80	85
C_{11}	Quartz				✓	✓	✓		✓	
C_{33}	Quartz	✓	✓	✓		✓	✓			✓
	EMAT		✓	✓		✓	✓			✓
C_{44}	Quartz			✓				✓		✓
	EMAT			✓				✓		✓
C_{66}	Quartz		✓		✓	✓	✓		✓	

Table 6.1. Table showing the temperature at which anomalies were observed in the elastic constants measurements at 0.5 T.

The H_o - T plot of the EMAT signal amplitude show the correlation of increase in EMAT signal amplitude with first order magnetic transitions in the $Er_{91.6\%}Tm_{8.4\%}$. Although the magnetic phase transition temperatures can not be determined from the EMAT signal amplitude, but can be use as a quick preliminary method of indicating temperatures where possible magnetic phase transition temperatures occurs.

References

Eccleston R.S. and S.B. Palmer 1992, J. Magnetism and Magnetic Materials, **104-107**, pp1529-1530.

Parnell S.R., Lim C.M., Eccleston R.S., Palmer S.B., Salgueiro da Silva M., Moreira J.M., Sousa J.B., McIntyre, 1998, J. Magn. Magn. Mat., **177-181**, pp 1014-1015.

Chapter 7

Conclusion And Further Work

The aims of this work have been achieved (listed in chapter 1). An existing commercial ultrasound measurement system (Matec DSP-8000) have been adapted for use in the study of magnetoelastic effects of single crystal rare earth metals and alloys. The automated ultrasound measurement system was also adapted and improved to function with relatively low efficiency transducers, such as EMATs. The DSP-8000 software has been modified for use with Oxford Instruments cryogenic and superconducting magnet system. The ultrasound system is therefore capable of performing ultrasonic velocity ($\Delta v/v \sim 0.0005$ and $\Delta t = \pm 0.001$ μs) and attenuation measurements ($\Delta V = \pm 8$ mV) as a function of : (a) temperature (4.2 to 300 K ± 0.1 K), (b) applied magnetic field (0 to 11 T ± 0.01 T) and (c) ultrasound frequency (5 to 20 MHz ± 10^{-6} MHz).

Although the present ultrasound measurement system have been successfully used in the studies of single crystals of Er, Tm and Er-Tm, further improvements to the system can be made. To improve the sensitivity of the velocity measurements the digitisation rate of the A/D board can be increased from the present 100 MHz to 800 MHz. The equivalent time sampling mode (ETS) had be implemented to enable the A/D board to perform at 800 MHz. In the ETS mode the wave-forms are captured repeatedly, with the trigger position (in the time domain) shifted by 1.25 ns each time the wave-

form is captured. The ultrasonic wave-form is then reconstructed by interleaving the 8 sets of wave-forms. The reconstructed waveform can then be feed into the auto-correlation routine for the time of flight of the pulse echoes to be extracted.

In order for the automated ultrasound system to achieve its intended purpose of velocity and attenuation measurements with reasonable sensitivity and accuracy, the ultrasonic pulse-echoes need to have very similar profile. To obtain similar pulse-echo profiles the interference between mode converted waves with the main ultrasonic pulse-echoes had be minimal.

The use of tone-burst with a Gaussian profile in ultrasound measurements is to limit the frequency components in the ultrasonic waves. The tone-burst generator card used in the ultrasound measurement system did not generate tone-burst with a Gaussian profile. This implies the auto-correlation algorithm would be more likely to select the incorrect frequency peak hence introducing errors in the determination of the time-of-flight. This is because there would be several significant frequency peaks in the wave-form (frequency domain). Replacing the tone-burst generator with one which produces gaussian shaped tone-burst and has a higher peak to peak output voltage (~ kV) would improve the performance of the system significantly.

The time-of flight of the ultrasound pulse echoes is only one of the many information which are contained in the ultrasound waveforms. The waveform storage function added to the original software would allow further analysis on the waveforms to be carried out using separate mathematical software. As a suggestion for further

work, the wave-form analysis can be performed within the ultrasound measurement software by including mathematical routines, such as Fast Fourier Transforms (FFT) and filtering, in the software.

In the present ultrasound system the ultrasound attenuation measurements uses the signal amplitude from two successive pulse echoes (V_1 and V_2) from which the attenuation is calculated using $20\log(V_1/V_2)$. A curve fitting routine can be written in the software to enable an exponential function to be fitted over three or four pulse echoes for the ultrasonic attenuation to be determined.

The display of data on the computer screen can be further improved. At present the software only displays the data in a tabulated form. It would be more useful if the data were presented as 2-D graphs, e.g. velocity versus temperature with the graph being up dated every time data is captured.

This study of EMAT acoustic generation in single crystals of Er, Tm and Er-Tm shows the complexity of the generation mechanisms. The EMAT data from this work did not show a distinction between the acoustic signal generated by magnetoelastic effects from the Lorentz mechanism. It can be concluded that the EMAT signal increases (at least x 10 the base level) when the sample temperature approaches the first order magnetic transition temperatures (known from other established characterisation methods) of the samples. The EMAT signal level remained high (> x 10) when the samples were in the ferromagnetic state (Er, Er-Tm) and ferrimagnetic state (Tm). The EMAT signal showed an increase as the sample (Er, Tm and Er-Tm) temperature

approaches T_N and then decreases as T gets further away from T_N. However, the EMAT signal remained high over at least ±10 K on either side of T_N, in otherwords the increase in EMAT signal can only provide a crude estimate of the magnetic phase transition temperature (ΔT_N = ±10 K). The H_o - T plot of the EMAT signal amplitude, figure 5.17 and 6.19, summarises the dependence of the EMATs acoustic coupling efficiency on H_o and T in the single crystals of Tm and $Er_{91.6\%}Tm_{8.4\%}$. Some correlations between the changes in the EMATs acoustic coupling efficiency and the anomalies in ultrasonic velocities (quartz measurements) were observed. The magnetic structures of $Er_{91.6\%}Tm_{8.4\%}$ are known only at zero applied field [Parnell *et al.*, 1998]. The phase boundaries for $Er_{91.6\%}Tm_{8.4\%}$ coincide with ultrasonic velocity data at zero field and these anomalies can be tracked using the ultrasonic velocity data of $Er_{91.6\%}Tm_{8.4\%}$ in higher applied magnetic fields. These velocities anomalies are superimposed on contour plots of EMAT signal amplitude variation. The detail in these H_o - T plots can be improved by increasing the data density (present data were taken at 0.1 T field increments and ~ 0.5 K temperature increments).

The elastic constants (velocity measurements) obtained using quartz and EMATs agreed very well. However the inconsistency of the EMAT generated ultrasound did not allow the attenuation measurements to be made using EMATs. The dependence of the EMAT acoustic coupling efficiency on temperature and applied magnetic field meant that care had to be taken in the velocity measurements, figure 4.5. The acoustic generation could become highly efficiency which results in the interference of the mode converted acoustic signals with the main pulse echoes and therefore introducing errors to the time-of-flight measurements. In the other extreme the EMAT acoustic coupling

efficiency could be reduced to the noise level and thus preventing the time-of-flight measurements to be made.

All the EMATs measurements carried out in this work required a static applied magnetic field, H_0. A minimum of ~ 0.1 T was required when the samples were in the ferromagnetic (Er, Er-Tm) and ferrimagnetic states (Tm). $H_0 > 0.5$ T when the samples were paramagnetic and antiferromagnetic. The velocity measurements using EMATs was also restricted by an upper limit of H_0. In the ferromagnets when $H_0 > 2$ T the ultrasonic wave-forms became complicated with mode converted signals. The present system and the design of the EMATs can be further improved to lower the magnitude of H_0 required for at least 3 to 1 signal to noise ratio to be obtained.

The use of EMATs in this work show the benefit of non-contact ultrasound measurement method where the samples and transducers were subjected to extreme of temperatures (4.2 K to 300 K). The problems associated with the fracture of acoustic couplant were eliminated.

The ultrasound measurements, both EMATs and quartz, showed several anomalies in elastic constants of Tm and Er-Tm. Several of these anomalies correlated with the known magnetic transition temperatures of the samples. Apart from the anomalies associated with the known magnetic phase transitions in Tm, the ultrasound measurements also showed anomalies in the ultrasonic wave behaviour at 26 K, 38 K, 68 K and ~ 90 K. Further investigations are required to identified the physical changes associated with these anomalies. The elastic constants measurements of Tm need to be

completed for C_{13} as a function of temperature and applied magnetic field. This would enable the wave and slowness surfaces of Tm to be constructed which can then be use to explain the ultrasonic waves propagation behaviour in Tm. The effects of a c-axis applied magnetic was shown to be most significant above 3 T on C_{33} and C_{44}. Further work is required to study the ultrasonic wave behaviour close to the ferrimagnetic to ferromagnetic transition boundary.

The automated ultrasonic system could be used to study other materials as a function of temperature and magnetic field, e.g. superconductors. Improved techniques for measuring the EMAT acoustic efficiency changes (linear amplifiers with a wide dynamic range) combined with theoretical modelling may aid in the identification of the magnetic phase boundaries in rare earth metals.

References

McEwen K.A., Steigenberger U. and Jensen J. , J. Magm. Magn. Mater., 1995, **140 - 144**, pp 767-768.

Parnell S.R., Lim C.M., Eccleston R.S., Palmer S.B., Salgueiro da Silva M., Moreira J.M., Sousa J.B., McIntyre, 1998, J. Magn. Magn. Mat., **177-181**, pp 1014-1015.